Università degli Studi di Torino

Doctoral School of Sciences and Innovative Technologies

PhD Program in Chemical and Material Sciences XXXIV Cycle

Synthesis and Characterization of Advanced Nanostructured Materials for Applications in HER, MeOH Electrooxidation and SERS

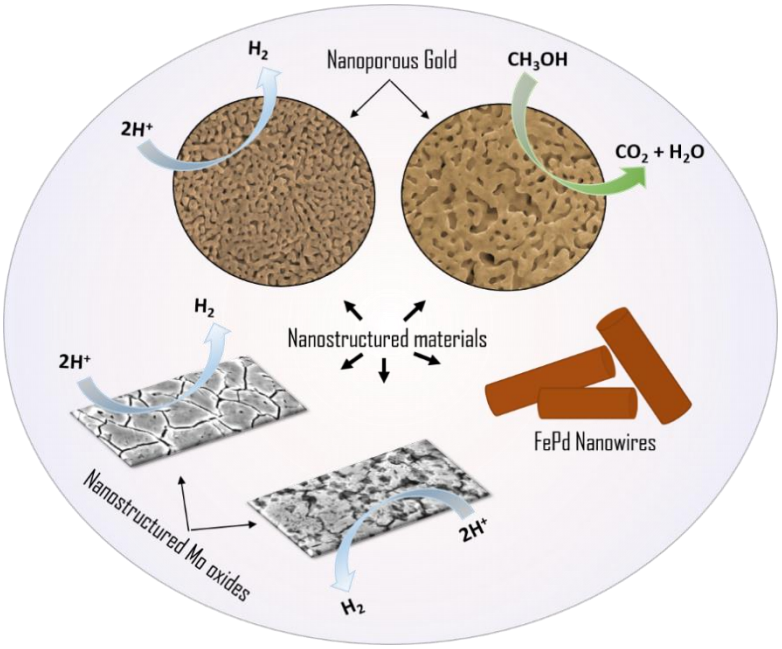

Deepti Raj

Supervisor: Prof. Paola Rizzi

Università degli Studi di Torino

Doctoral School of Sciences and Innovative Technologies

PhD Program in Chemical and Material Sciences XXXIV cycle

Synthesis and Characterization of Advanced Nanostructured Materials for Applications in HER, MeOH Electrooxidation and SERS

Candidate: **Deepti Raj**

Supervisor: Prof. **Paola Rizzi**

Jury Members: Prof. **Alberto Castellero**

Dipartimento di Chimica

Università degli Studi di Torino, Torino, Italy

Prof. **Eva Pellicer**

Departimento di Physica

Universitat Autònoma de Barcelona, Barcelona, Spain

Prof. **Paola Tiberto**

Istituto Nazionale di Ricerca Metrologica (INRIM)

Torino, Italy

Head of the Doctoral School: Prof. Alberto Rizzuti

PhD Program Coordinator: Prof. Bartolomeo Civalleri

Torino, 2021

PREFACE

The aim of this preface is to give an overview of the main topics treated in this PhD thesis.

This dissertation, titled "Synthesis and Characterization of Advanced Nanostructured Materials for Applications in HER, MeOH Electrooxidation and SERS", has been submitted to the Doctoral School of the University of Torino to fulfil the requirements for obtaining the PhD degree in Chemical and Material Science. The results presented in this dissertation have been obtained in the last three years as a PhD student of the XXXIV cycle (from October 2018 to December 2021) in the Metallurgy research group, under the supervision of Prof. Paola Rizzi, at the Department of Chemistry, University of Turin, Turin, Italy.

Chapter I provides a broad introduction to the contents of the thesis, underlining the main motivation behind the work undertaken and its importance as well as giving a glimpse into each chapter in a more detailed fashion highlighting the major expectations and findings along the way.

Chapter II summaries the experimental and theoretical methods used in this thesis.

Chapter III-V contains the main results obtained during the PhD. The discussions and conclusions of the results are reported for each chapter.

Overall conclusions of this whole thesis are reported in the final **Chapter VI**.

INDEX

Chapter I

INTRODUCTION

As beings of the twenty-first century witnessing the remarkable technological progresses it would an understatement to say that our lives are hugely dependent on unlimited families of advanced materials. Whether it is about manufacturing and improving some of the most indispensable parts of human lifestyle today, i.e., laptops, computers, digital cameras, smartphones, nano-sensors, microwave ovens, automated cars and many other intelligent devices and instruments, or about taking steps in the direction of sustainable development in terms of energy generation and storage and conservation of non-renewable resources of earth, there is a vital need of special type of materials that have superior properties. Nanostructured materials come into the picture here. An extremely intriguing class of advanced materials, nanostructured materials possess most unique physical and chemical properties. These properties are substantially different from their bulk counterparts which include excellent mechanical, thermal, electrical, magnetic, optical, and biological properties and behaviours. For example, gold can become liquid when it is in nanosize at lower temperatures. Additionally at nanoscale, the surface area to volume ratio is exponentially increased which is why nanomaterials also typically have an enhanced surface area and high surface energy. In recent times, umpteen number of nanostructured materials, such as nanoporous metals, nanotubes, nanoparticles, nanofilms, nanofibers, nanowires, and nanocomposites, have been produced that either have already found or have strong potential for applications in energy generation, storage, biosensors, artificial muscle development, nanofiltration units, and medicines.

As the global energy needs increment incessantly for countless applications, it has become absolutely pivotal to regulate the usage of fossil fuel resources and take compelling steps towards sustainable solutions and alternatives. This calls for the employment of renewable energy resources to meet the demands of the ever-developing world. In the same thread, hydrogen gas has emerged as an excellent source of energy with immense potential which is produced at the industrial level by the half-cell reaction of hydrogen evolution (HER) during the electrolysis of water. To catalyse this reaction the most common electrocatalysts are Pt-based that showcase impressive performance. But the exploitation of these electrocatalysts has become hugely problematic which can be narrowed down three main factors - the scarcity of Pt, its expensiveness and substandard stability as an electrocatalyst. In totality it is not a sustainable, long-term solution for the electrocatalysis of HER. In addition, Direct methanol fuel cells (DMFCs), which convert the chemical energy of methanol in electric energy via methanol electro-oxidation, too have been attractive with regard to production of sustainable energy. The conventional electrocatalysts are Pt-based like Pt−Cu and Pt−Ru alloys. But

again, Pt comes with its disadvantages - expensiveness, instability and susceptibility to poisoning. Hence, it becomes the need of the hour to strive for highly efficient and durable yet sustainable and affordable alternatives for Pt-based electrocatalysts. With the knowledge of the outstanding properties owned by nanostructured materials as discussed before, it is only fair to exploit them to be possible competitors in the race against Pt-based electrocatalysts all the while continuing the search for the best alternative. Therefore, this dissertation attempts to contribute to the study of cheaper, more durable and efficient alternative electrocatalysts for sustainable energy employing different nanostructured materials.

Nanoporous (NP) materials/metals, renowned as one of the most promising candidates for electrocatalytic applications, are a fascinating class of nanomaterials with one-of-a-kind chemical and physical properties that have possible applications in other fields as well, e.g., actuators, sensors, filtration membranes, etc. They are essentially built of a three-dimensional framework of nano-scale pores and ligaments. The final properties of these nanoporous materials directly depend on and derive from the unique properties of the pore-ligament scaffold such as their dimension, composition, morphology, etc. This means that the properties of the fabricated NP metals have a large scope which depends as a whole on the parameters of the preparation method. Speaking of the preparation method, a remarkably straight-forward and efficient method that has gained accolades in the past few years is called dealloying. Dealloying is defined as the selective corrosion of one or more less-noble metals in an alloy precursor without impacting the composition of the more noble metals. This phenomenon is comprised of two events taking place simultaneously – (i) selective and gradual removal of the less noble metals and (ii) rearrangement of the remaining more noble metal atoms by surface diffusion. This method is applicable to both crystalline and amorphous alloy precursors. The most common types of dealloying are chemical and electrochemical dealloying. The NP metals prepared by this method have a large scope of tunability and flexibility in terms of their chemical and physical properties which can be modified according to the desired application by playing with the parameters of dealloying. To design the preparation method based on dealloying, few parameters need to be considered with utmost care – (i) parting limit (defined as the minimum concentration of the noble metal component of the alloy precursor above which no selective corrosion can take place); (ii) a substantial difference between the electrochemical potentials of the components of the alloy precursor (mainly in the case of electrochemical dealloying); (iii) corrosion potential at which the dealloying can occur; (iv) choice of a suitable electrolyte in accordance with the Pourbaix diagram.

This thesis will provide a comprehensive study into various nanostructured (NS) materials, namely, Nanostructured Mo oxides, Nanoporous Gold (NPG) and FePd nanowires describing their preparation methods and characteristics. These obtained samples have been exploited in different applications which are also described in depth in corresponding chapters. The main applications studied are namely HER, Methanol electrooxidation (MeOH-EOx) as well as Surface-enhanced Raman Spectroscopy (SERS) where the samples have been utilized as electrocatalysts and active substrates respectively. The samples have demonstrated promising performance in each of the mentioned applications showcasing great potential as cheaper,

efficient, stable and sustainable alternatives for the said applications. All the results obtained during the period of these three years of the PhD have been compiled in the following four chapters of this dissertation. The following paragraphs aim to provide a glimpse at the contents of each chapter briefly underlining the main points.

The coming chapter consists of detailed explanation about the experimental and theoretical methods employed in this thesis.

The third chapter deals with the study of NS Mo oxides, explaining the methods and techniques involved in their fabrication as well as their potential application as electrocatalyst for HER. In this work, Mo_3Al_8, an intermetallic compound, has been used as a precursor to obtain NS Mo oxides. First, the precursor was prepared into ribbons by arc-melting and melt-spinning techniques subsequently. The as-quenched ribbon was then subjected to single and double-step free corrosion studied in 1 M KOH, 1 M HF and 1.25 M $FeCl_3$ at room temperature. In both cases, NS Mo oxides have been obtained on a surface layer a few microns thick. The as-quenched ribbon and the as-prepared NS samples have been fully characterized using various techniques such as X-ray diffraction (XRD), scanning electron microscopy (SEM), energy dispersive X-ray spectrometry (EDS), etc. Two of the as-prepared samples were tested for their electrocatalytic capability for HER in 0.5 M H_2SO_4 giving low onset potential (-50 mV, -45 mV), small Tafel slopes (92 mV dec^{-1}, 9 mV dec^{-1}) and high exchange current densities (0.08 mA cm^{-2}, 0.35 mA cm^{-2} respectively). The proposed NS Mo oxides are cost-effective and sustainable due to the cheap and abundant starting material used and the simple synthetic route, paving the way for their possible application as HER electrocatalysts.

In the fourth chapter, we report the facile synthesis of low-cost NPG samples, their thorough characterization and impressive applications in HER, SERS and MeOH-EOx. The method of dealloying has been chosen as the synthetic technique and the alloy precursor used for the dealloying process is the Fe-rich metastable $Au_{33}Fe_{67}$ supersaturated solid solution. The Au-Fe system is quite an interesting case which has been illuminated in depth. With a huge miscibility gap between Au and Fe at room temperature, the conventional methods of obtaining a solid solution precursor alloy fall short here. To tackle this, the technique of melt-spinning was employed which resulted in a metastable supersaturated solid solution of the desired composition at room temperature by the phenomenon of rapid solidification in the form of ribbons. The resultant microstructure of the Au-Fe precursor has been extensively described. Two different batches of NPG samples have been obtained from the as-quenched ribbon by chemical dealloying in 1 M HNO_3 and 1 M HCl at 70 °C for different durations of time. The obtained NPG samples are homogeneous with tunable ligament size and shape, easy-to-handle and free-standing. The as-quenched ribbon and the dealloyed samples have been structurally and compositionally investigated using XRD, Field-Emission SEM (FESEM) and EDS techniques. Taking advantage of the typically enhanced surface area, one of the NPG samples has been tested for its electrocatalytic activity for HER in 0.5 M H_2SO_4. Low values of onset potential (-4 mV) and Tafel slope (47 mV dec^{-1}) while high exchange current density (0.12 mA cm^{-2}) with remarkable stability of more than 20 h have been

achieved. Surface-Enhanced Raman Scattering (SERS) was also explored with the same NPG sample using 4,4′-bi-pyridine as the probe molecule. Strong SERS effect has been observed with low detection limit of 10^{-15} M. Evidently, the NPG sample performs excellently as a competent and durable alternative to Pt-based electrocatalysts for HER as well as an economical and highly sensitive SERS-active substrate for potential applications in life science and ultrasensitive instrumentation. Another NPG sample has been examined as an electrocatalyst for MeOH-EOx profiting, again, off its large surface area. In a basic solution of methanol (MeOH) and KOH the sample displays a low peak potential of 0.47 V vs Ag/AgCl for MeOH-EOx with high peak current density of 0.43 mA/cm^2. In addition, it demonstrates outstanding stability and high poisoning tolerance. Thus, the proposed NPG sample acts as an economic, efficient and stable alternative electrocatalyst for MeOH-EOx. As a whole, the properties and results put forth by the NPG samples make them brilliant, inexpensive, sustainable alternatives for HER, SERS and MeOH-EOx. Furthermore, it is highly crucial to emphasize that a metastable precursor has been favourably obtained from an immiscible Au-Fe system. The fabrication process from start to end has been intentionally opted to be a sustainable, cost-effective, rapid and feasible one. Pairing Au with cheap and abundant Fe and fabricating an Fe-rich precursor gives an exceedingly cost-effective starting material. No usage of critical raw materials is involved. Then, employing a straight-forward and rapid dealloying procedure to obtain the NPG samples, makes for an overall inexpensive and sustainable production.

The fifth chapter deals with the study of another interesting class of nanostructured materials, i.e., nanowires, focussing on the elemental discussion about their fabrication and properties. Dense and mesoporous FePd nanowires (NWs) with different compositions and diameters have been fabricated by template- and micelle-assisted electrodeposition into nanoporous anodic alumina and polycarbonate templates using pulsed-potentiostatic electrodeposition technique. The structural and magnetic properties of the obtained NWs were investigated by XRD, FESEM, EDS, transmission electron microscopy (TEM) and vibrating sample magnetometer (VSM). Interesting physical, chemical and magnetic properties have been demonstrated by the obtained nanowires.

The sixth and the final chapter presents the important conclusions and highlights of this research work.

Overall, this dissertation aims to present a complete, compact and comprehensive study on different classes of nanostructured materials and their remarkable performance in various applications backed by solid experimental and theoretical evidences.

Chapter II

EXPERIMENTAL

FABRICATION TECHNIQUES

1. Vacuum Arc Melting Furnace

To synthesize the precursor alloys arc melting technique has been used which is a simple but effective method. It is also the most conventional melting process that produces metal ingots of high homogeneity for various applications. It consists of forming an alloy by melting the pure elements in the stoichiometry desired by discharging an electrical arc due to the application of a large tension between two electrodes. A schematic diagram of the arc melting method can be found in Figure 1.

Basic Principle:

Heat is generated by the electric arc that is struck between the metals and a tungsten electrode. This generated heat then serves to melt the metals placed in a crucible in the copper hearth to form an alloy.

There are three main parts to the system:

(i) Power source

A standard Tungsten Inert Gas (TIG) welding unit is used as a power source.

(ii) Chiller

The chiller facilitates cold circulation of water that cools both the electrodes and the copper hearth.

(iii) Vacuum unit

The chamber is evacuated to avoid oxidation of the melt. Then it is filled back with argon gas. Ar being an inert gas does not react with molten metal. Hence, melting is performed in argon atmosphere.

Procedure to synthesize a sample:

After the tension is applied, by turning a millimetric screw the cathode is brought close to the pure elements placed on the Cu crucible. Argon gas must flow through the furnace chamber at a pressure of 1-1.5 bar. When the cathode reaches close to the metals, the Ar gas is ionized that discharges an arc which melts the pure elements. The metals can be heated to a temperature in excess of 2000 ºC. The molten elements are then mixed after few seconds of melting and at this point the tension can be suspended. Once the molten metals are solidified, a master alloy is formed which can be 'turned over' by a 'tweezer mechanism'. It happens without breaking the vacuum and then the master alloy can be re-melted. This cycle of melting, solidification, 'turn over' of sample and re-melting is typically repeated three times to attain a better compositional homogeneity of the master. The synthesis process of a sample includes a number of meltings, with the sample being turned over each time in order to ensure a good homogeneity of the elements in the alloy. The sample is weighted after each melting to control possible weight losses, which must be negligible to maintain the desired stoichiometry. At least one of the elements must be metallic, because on the contrary the arc cannot be discharged. Alloys are easy to obtain with this method, but it also presents a drawback: sample cooling is not homogeneous when the arc is broken off. At the bottom of the sample, where there is contact with the water-cooled Cu crucible, the cooling of the sample is faster than at the top of the latter. During the brief cooling process, the top sample crystallises forming characteristic faceted- and bright- sides, like a football ball. At the bottom, the alloy does not crystallise in facets and it simply presents a metallic look.

Applications:

(i) Melt elements to form an alloy using a high temperature arc.
(ii) Re-melt alloys to improve homogeneity.
(iii) Suction cast the melt in a copper mold.

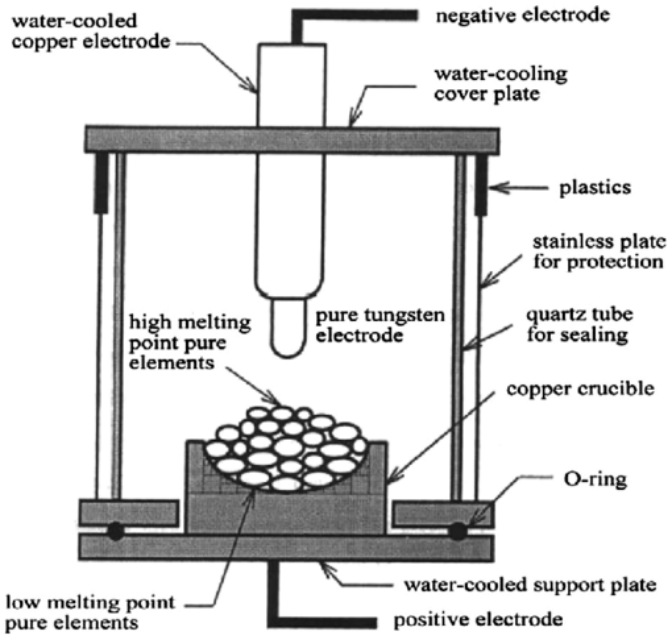

Figure 1. A schematic diagram of the arc melting method

2. Rapid Solidification

Rapid solidification (RS) is a commonly used method. In general, this technique can be defined as the fast extraction of thermal energy of metals or alloys from liquid state to solid state at room temperature. The metal in the liquid state is very short in contact with the cold surface, causing instant supercooling to occur in the liquid metal over 100°C during the solidification. RS affects the microstructure (see Fig. 1) and phase equilibrium and offers the following advantages:

1) Refinement of microstructure;
2) Extension of solid solubility;
3) Increased chemical homogeneity;
4) Precipitation of non-equilibrium crystalline phases; and
5) Formation of amorphous phases.

In order to achieve RS the following criteria must be satisfied:

(i) Realization of excessive cooling before the occurrence of solidification

(ii) High velocity of the solidification front during continuous solidification

(iii) Achieve a high cooling rate during solidification.

Rapid cooling takes place just in the line of solidification in first two methods. High cooling rates allows influential conduction of thermal energy in all stages of solidification process. The main parameter to achieve high cooling rate is to reduce at least one size of solidifying metal or alloy and exposing the alloys to high heat subtraction rates.

There are several various rapid solidification techniques for production of superior metals. The most widespread technique is the melt spinning method.

• Melt Spinning

Melt spinning is a well-known technique used for rapid cooling of molten liquids to produce metallic metastable solid solutions in the form of thin strips (called ribbons). This approach, which was introduced by Duwez and his group in 1960 has led to synthesizing of several hundred binary, ternary, and multicomponent amorphous and metallic glassy systems during the last five decades. This method is nowadays standard in industrial applications for producing different dimensions of ribbons due to its high cooling rate and the ability to process large volumes of materials. It is worth mentioning that melt spinning of molten metallic system does not only lead to the formation of amorphous and metallic glassy alloys, but also leads to the formation of other non-equilibrium phases, such as nano-crystalline, quasi-crystalline phases and supersaturated solid solution.

Figure 2 can be referred for the schematic illustratration of the basic configuration of a single-roller melt-spinning apparatus (left image) for preparing ribbon-like metallic materials (right image). In a typical melt-spinning process, certain amount (5-100 g) of small pieces of alloy is placed inside a crucible (usually made of quartz glass or sometimes made of boron nitride for high-temperature use) surrounded by induction coil. Applying high current leads to rise in the temperature of the alloy inside the crucible, and accordingly it melts. Then, a thin stream of molten liquid is ejected by Ar-pressurization through a fine nozzle onto the surface of a fast-rotating copper wheel, which usually rotates at 5,000-7,000 rpm. This rotating wheel is cooled internally, usually by water or high thermal conductive materials, such as copper. The heat of the molten liquid is absorbed into the roller rapidly and a cooling rate is on the order of 10^4–10^7 K/s aided by the high-rotation of the wheel. Such high rates of rapid solidification compel the atoms of the molten metal alloy system to freeze and form a supersaturated solid solution. The cooling rate of the melt-spinning process depends on the following factors: the thickness of the melt to be cooled, which is normally controlled by changing the revolution rate of the quenching roller; the pour rate of the molten alloy, which is normally controlled by the opening diameter of the ejecting nozzle and pressure; the heat transfer from the melt to the roller surface, which depends on interface energy between the melt and the roller surface, heat conductivity of the roller material, heat transfer between the roller and cooling water, and so on. The cooling rate must be carefully optimized in order to avoid unfavourable grain growth, which is a key to achieve the desired material properties for melt-spun ribbons. After the rapidly quenched material leaves the rotating wheel, it is further cooled down by radiation and heat transfer to the surrounding gas, which is normally inert gas such as Ar or N_2 for air-sensitive materials. Therefore, all the above factors need to be considered when the experiment is designed and performed during the melt spinning process. Both twin-roller and single roller methods were introduced to produce rapidly solidified metallic ribbons, although the single-roller method is most widely used nowadays because of its simplicity and reproducibility.

There are many production parameters that affect the physical and mechanical properties of the produced ribbons such as wheel speed, liquid metal temperature, distance between nozzle and wheel surface, ejecting gas pressure and nozzle geometry. Among these variants, wheel speed is the most important factor. It is seen that the sizes of the ribbons decrease with increasing wheel speed. Moreover, when the linear velocity increases, also the cooling rate is increased, and this gives less time for the formation of dendrites and the grain growth, promoting a more homogenous alloy and small grain size. Among the size parameters, the ribbon thickness is the most important factor that effects the cooling rate and microstructure of the ribbons. The ribbon thickness decreases significantly with increasing wheel speed. The SEM micrographs of the produced ribbons had two different surface morphologies on the wheel side and air side. The wheel side surface of the ribbons is relatively smooth and has air pockets due to existence of poor heat transfer between the wheel and melted alloy. The air side of the ribbons has rough surface with metal flow lines parallel to melt flow direction. The grain sizes of rapidly solidified ribbons produced with higher wheel speed is smaller than that for low-speed ribbons.

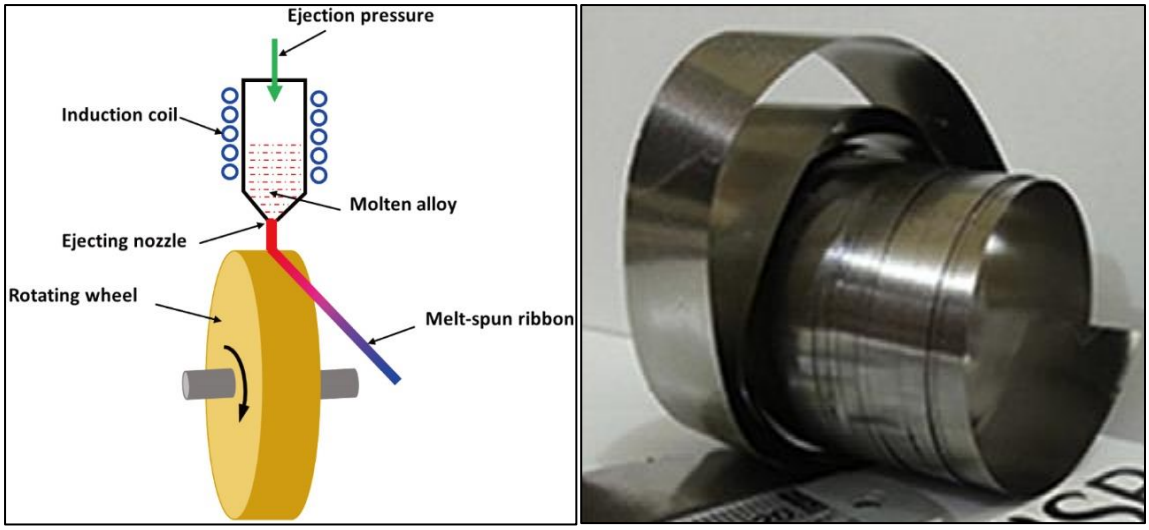

Figure 2. Schematic presentation illustrates the basic configuration of a single-roller melt-spinning apparatus (left) for preparing ribbon-like metallic materials (right).

CHARACTERIZATION TECHNIQUES

1. X-Ray Diffraction

X-rays have photon energies in the range 100 ev – 100 kev. In structural characterisation, mainly short wavelength x-rays are used, with a range of 10>0.1 Angstroms. X-rays are typically produced by synchrotron radiation or by x-ray tubes. A schematic representation of an XRD machine is provided in Figure 3. X-ray tubes are the main source used in laboratory x-ray instruments. Synchrotron facilities are far more expensive to use, but give improved results due to being more than a thousand times more intense than x-ray tubes.

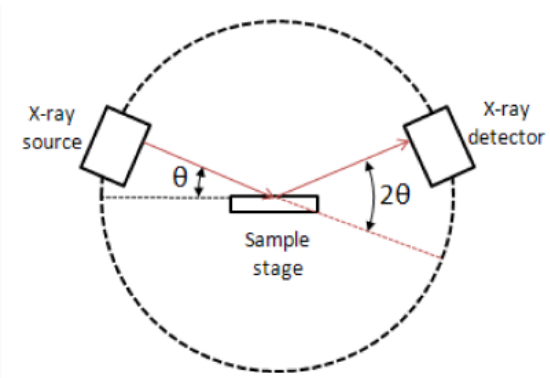

Figure 3. Schematic diagram of an XRD machine.

When an x-ray beam hits the sample, it interacts with electrons in the atoms. Some photons in the incident beam will be deflected away from their original path. The deflected photons with unchanged wavelength have been elastically scattered (photons not lost energy), it is these photons that are measured in diffraction experiments since they hold information about the electron distribution in the material. The peaks generated in x-ray diffraction are related to the atomic distances by Bragg's law. Figure 4 below schematically demonstrates the Bragg's equation.

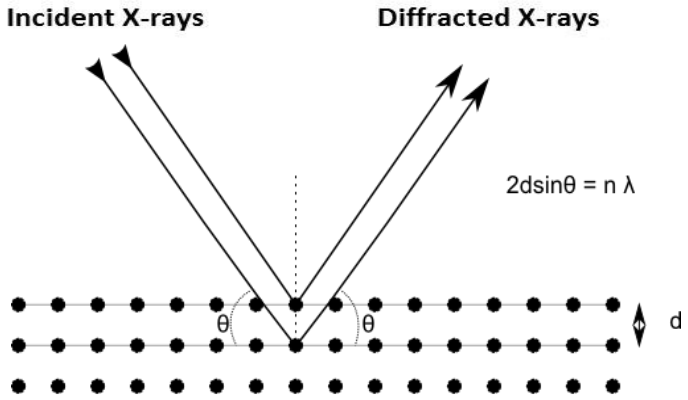

Figure 4. Schematic representation of the Bragg equation.

2. Scanning Electron Microscopy (SEM)

Scanning electron microscopes (SEMs) have become powerful and versatile tools for material characterization, especially in recent years, as the size of materials used in various applications continues to shrink. SEM is designed for directly studying the surfaces of solid objects that utilizes a focused beam of electrons of relatively low energy as an electron probe that is scanned in a regular manner over the specimen producing magnified detailed images of an object. SEM can examine each particle, including the aggregate particles, individually; thus, the method is considered to be an absolute measurement of particle size. One can easily visualize crystal shape, surface morphology, dispersed and agglomerated nanoparticles, and surface functionalization. It can also be coupled to image analysis computers for examination of each field for particle distribution. SEM is widely used to investigate the microstructure and chemistry of a range of materials. Electrons are created and fired using an electron gun which accelerates down the microscope passing through a series of lenses and apertures creating a focused beam which then interacts with the surface of a sample. The electrons that are reflected or knocked off the near-surface region of a sample are then utilized to create high resolution images that provide information on a material's surface composition and topography.

Sample Collection and Preparation:

Sample preparation can be minimal or elaborate for SEM analysis, depending on the nature of the samples and the data required. Minimal preparation includes acquisition of a sample that will fit into the SEM chamber and some accommodation to prevent charge build-up on electrically insulating samples. Most electrically insulating samples are coated with a thin layer of conducting material, commonly carbon, gold, or some other metal or alloy. The choice of material for conductive coatings depends on the data to be acquired: carbon is most desirable if elemental analysis is a priority, while metal coatings are most effective for high resolution electron imaging applications. In its simplest form, preparation for SEM involves securing a specimen on to a metal support 'stub' and, if the sample material is non-conducting, coating the surface with a conducting thin layer of metal. The requirement for conductivity is to prevent the build-up of electrical charge on the specimen surface once it is bombarded with electrons within the instrument and also to enhance the secondary image.

Instrumentation:

Figure 5 illustrates the main SEM components which include:

- ***Electron Source ("Gun"):*** First, electrons are generated at the top of the column by the electron source. These are emitted when their thermal energy overcomes the work function of the source material. They are then accelerated and attracted by the positively-charged anode. In conventional SEMs, the source of electrons is generally a heated tungsten filament, which provides ease of operation, low cost, and simplicity. More intense sources include lanthanum hexaboride (LaB6) tips and field emission guns and these are used where greater brightness is required. Accelerating voltages used typically range from less than 1 kV up to 40 kV. The higher voltages can provide greater resolving power, but at the risk of excessive penetration into many specimens and damage by the electron beam. Lower voltages are used to image fine structure on sample surfaces.

- ***Electron column:*** Electrons, produced at the top of the column, are accelerated downwards where they pass through a combination of lenses and apertures to produce a fine beam of electrons. lenses are used to control the path of the electrons. Because electrons cannot pass through glass, the lenses that are used are electromagnetic. They simply consist of coils of wires inside metal pole pieces. When current passes through the coils, a magnetic field is generated. As electrons are very sensitive to magnetic fields, their path inside the microscope column can be controlled by these electromagnetic lenses simply by adjusting the current that is applied to them. Generally, two types of electromagnetic lenses are used: the condenser lens is the first lens that electrons meet as they travel towards the sample. This lens converges the beam before the electron beam cone opens again and is converged once more by the objective lens before hitting the sample. The condenser lens defines the size of the electron beam (which defines the resolution), while the main role of the objective lens is to focus the beam onto the sample. In many cases, apertures are combined with the lenses to control the size of the beam.

- ***Vacuum System:*** The entire electron column needs to be under vacuum. Like all components of an electron microscope, the electron source is sealed inside a special chamber to preserve vacuum and protect it against contamination, vibrations, and noise. Besides protecting the electron source from being contaminated, vacuum also allows the user to acquire a high-resolution image. In the absence of vacuum, other atoms and molecules can be present in the column. Their interaction with electrons causes the electron beam to deflect and reduces the image quality. High vacuum also increases the collection efficiency of electrons by the detectors that are in the column.

- ***Sample stage and chamber:*** The sample is positioned on a movable stage in the chamber of the microscope before a vacuum is created in the chamber via a series of pumps. The sample chamber is sturdy and insulated from vibration. The sample chambers also manipulate the specimen, placing it at different angles and moving it in all directions. The electron beam hits the surface of the sample mounted on this stage under vacuum. The sample surface is scanned by moving the electron-beam coils. The electron beam scans the sample in a raster pattern This beam scanning enables information about a defined area of the sample. The interaction of the electron beam with the sample generates a number of signals, which can then be detected by appropriate detectors capable of (i) producing the most detailed images of an object's surface and (ii) revealing the composition of a substance. The SEM's lens system also contains scanning coils, which are used to raster the beam onto the sample. Scan coils control the position of the electron beam above the objective lens. These coils allow for the beam to scan across the surface of the sample, enabling information about a defined area to be collated.

- ***Computer and display*:** Images are formed by modulating the brightness on a monitor (which is scanned in synchrony with the electron beam) according to the interactions generated by the beam moving over the specimen.

- ***Detectors:*** for all signals of interest.

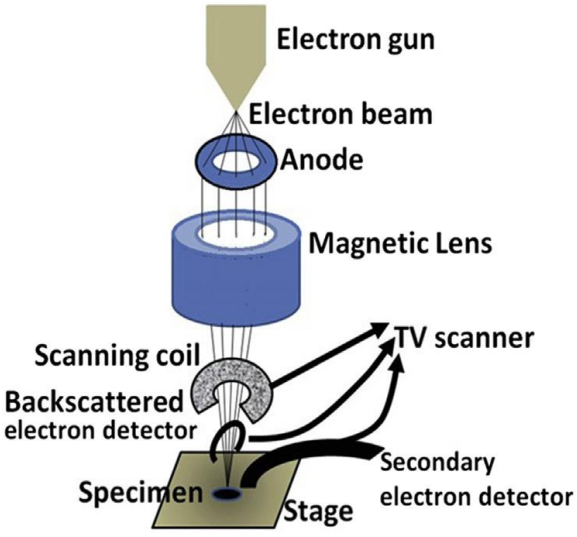

Figure 5. Components of a scanning electron microscope (SEM).

Sample-Electron Interaction:

The scanning electron microscope (SEM) produces images by scanning the sample with a high-energy beam of electrons. As the electrons interact with the sample, they produce secondary electrons, backscattered electrons, and characteristic X-rays. These signals are collected by one or more detectors to form images which are then displayed on the computer screen. When the electron beam hits the surface of the sample, it penetrates the sample to a depth of a few microns, depending on the accelerating voltage and the density of the sample. Many signals, like secondary electrons and X-rays, are produced as a result of this interaction inside the sample. The electrons in the beam interact with the sample, producing various signals that can be used to obtain information about the surface topography and composition. If these are collected and amplified, they can be used to create an image corresponding to the surface topography of the specimen. The great depth of focus of the microscope is achieved by the convergence angle of the primary electron beam and the relatively long working distance between the final lens and the specimen. This depth of focus enables production of images that appear to be three-dimensional. The maximum resolution obtained in an SEM depends on multiple factors, like the electron spot size and interaction volume of the electron beam with the sample. While it cannot provide atomic resolution, nowadays, following development of electron guns, electromagnetic lens systems and vacuum systems, some SEMs can achieve resolution below 1 nm. Typically, modern full-sized SEMs provide resolution between 1-20 nm whereas desktop systems can provide a resolution of 20 nm or more.

Types of signals:

When a fine beam of electrons is focused on to the surface of a specimen, these accelerated electrons carry significant amounts of kinetic energy, and this energy is dissipated as a variety of signals produced by electron-sample interactions when the incident electrons are decelerated in the solid sample. The signals that derive from electron-sample interactions reveal information about the sample including external morphology (texture), chemical composition, and crystalline structure and orientation of materials making up the sample. These signals include low-energy secondary electrons, high-energy back-scattered electrons, diffracted back-scattered electrons (EBSD that are used to determine crystal structures and orientations of minerals), photons (characteristic X-rays that are used for elemental analysis and continuum X-rays), visible light (cathodoluminescence-CL), and heat. Figure 6 exhibits these different types of signals and the area of the sample from which they originate.

The two types of electrons used commonly for imaging samples in SEM are secondary electrons (SE) and backscattered (BSE). SE originate from the atoms of the sample; they are a result of inelastic interactions between the electron beam and the sample. By contrast BSE belong to the primary electron beam and are reflected after elastic interactions between the beam and the sample. Because BSEs come from deeper regions of the sample whereas SEs

originate from surface regions, the two carry different types of information. SE imaging provide more detailed surface information and thus are most valuable for showing morphology and topography on samples. The more secondary electrons emitted from any one spot on the surface of the specimen, the greater the signal from the detector, and the brighter the area seen at that point in the image on the monitor. BSE images show high sensitivity to differences in atomic number; the higher the atomic number, the brighter the material appears in the image and this can be used to map the distribution of elements in the specimen. So, BSE are most valuable for illustrating contrasts in composition in multiphase samples (i.e., for rapid phase discrimination). As they tend to arise from deeper within the surface of the specimen however, backscatter electrons are not as good as secondary electrons for resolving surface topography.

BSEs and SEs are detected by different types of detectors. For the detection of BSEs, solid state detectors are placed above the sample, concentrically to the electron beam, to maximize BSE collection. For the detection of SEs, the Everhart-Thornley detector is mainly used. It consists of a scintillator inside a Faraday cage, which is positively charged and attracts the SEs. The scintillator is then used to accelerate the electrons and convert them into light before reaching a photomultiplier for amplification. The SE detector is placed at an angle at the side of the electron to increase the efficiency of detecting SEs, which are then used to form a 3D-image of the sample shown on a PC monitor. X-ray generation is produced by inelastic collisions of the incident electrons with electrons in discrete orbitals (shells) of atoms in the sample. As the excited electrons return to lower energy states, they yield X-rays that are of a fixed wavelength (that is related to the difference in energy levels of electrons in different shells for a given element). Thus, characteristic X-rays are produced for each element in a mineral that is "excited" by the electron beam. Every material produces X-rays that have a specific energy; X-rays are the material's fingerprint. In many microscopes, detection of X-

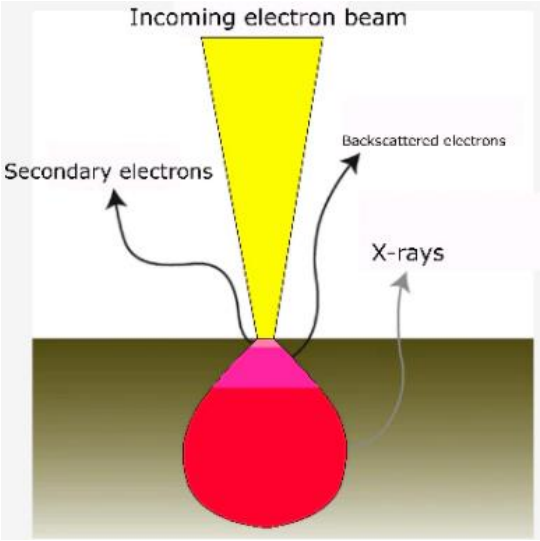

Figure 6. Different types of signals used by an SEM and the area of the sample from which they originate.

rays generated from the electron-matter interaction is widely used to perform elemental analysis of the sample. SEM analysis is considered to be "non-destructive"; that is, x-rays generated by electron interactions do not lead to volume loss of the sample, so it is possible to analyze the same materials repeatedly. The SEM is also capable of performing analyses of selected point locations on the sample; this approach is especially useful in qualitatively or semi-quantitatively determining chemical compositions (using EDS), crystalline structure, and crystal orientations (using EBSD).

Applications:

The SEM is routinely used to generate high-resolution images of shapes of objects (SEI) and to show spatial variations in chemical compositions: (i) acquiring elemental maps or spot chemical analyses using EDS, (ii) discrimination of phases based on mean atomic number (commonly related to relative density) using BSE, and (iii) compositional maps based on differences in trace element "activators" (typically transition metal and Rare Earth elements) using CL. The SEM is also widely used to identify phases based on qualitative chemical analysis and/or crystalline structure. Precise measurement of very small features and objects down to 50 nm in size is also accomplished using the SEM. Back-scattered electron images (BSE) can be used for rapid discrimination of phases in multiphase samples. SEMs equipped with diffracted backscattered electron detectors (EBSD) can be used to examine micro-fabric and crystallographic orientation in many materials. Moreover, Field emission scanning electron microscopy (FESEM) has narrower probing beams at low and high electron energy, so it provides improved spatial resolution while minimizing sample damage. The in-lens FESEM provides topographical information at magnifications of 250-1,000,000 with ion-free images. FESEM allows detection of small-area contamination spots at electron accelerating voltages, compatibility with energy dispersive X-ray spectroscopy, application of low kinetic energy electrons closer to the immediate material surface, and elimination of conducting coatings on insulating materials.

Strengths:

There is arguably no other instrument with the breadth of applications in the study of solid materials that compares with the SEM. The advantages of SEM include the detailed three-dimensional (3D) topographical imaging and the versatile information obtained from different detectors. Most SEMs are comparatively easy to operate, with user-friendly "intuitive" interfaces. Many applications require minimal sample preparation. For many applications, data acquisition is rapid (less than 5 minutes/image for SEI, BSE, spot EDS analyses). Modern SEMs generate data in digital formats, which are highly portable. great depth of field.

Limitations:

The disadvantages of SEM are its size and cost. SEM is expensive to operate. The preparation of samples can result in artefacts. A critical disadvantage is that SEM is limited to solid, inorganic samples small enough to fit inside a vacuum chamber that can handle moderate vacuum pressure. Samples must be solid and they must fit into the microscope chamber. Maximum size in horizontal dimensions is usually on the order of 10 cm, vertical dimensions are generally much more limited and rarely exceed 40 mm. For most instruments samples must be stable in a vacuum on the order of 10^{-5} - 10^{-6} torr. Samples likely to outgas at low pressures (rocks saturated with hydrocarbons, "wet" samples such as coal, organic materials or swelling clays, and samples likely to decrepitate at low pressure) are unsuitable for examination in conventional SEM's. However, "low vacuum" and "environmental" SEMs also exist, and many of these types of samples can be successfully examined in these specialized instruments. EDS_detectors on SEM's cannot detect very light elements (H, He, and Li), and many instruments cannot detect elements with atomic numbers less than 11 (Na). Most SEMs use a solid state x-ray detector (EDS), and while these detectors are very fast and easy to utilize, they have relatively poor energy resolution and sensitivity to elements present in low abundances when compared to wavelength dispersive x-ray detectors (WDS) on most electron probe micro-analyzers (EPMA). An electrically conductive coating must be applied to electrically insulating samples for study in conventional SEMs, unless the instrument is capable of operation in a low vacuum mode.

3. Transmission Electron Microscopy (TEM)

The first commercial transmission electron microscope was available in the 1940s when it was recognized that significant improvements in resolution could be made over the light microscope through the use of an electron beam rather than a light beam. Commencing circa 1950, the development of TEM revolutionized microscopy, progressively bringing it to new levels of magnification and resolution. Papers appeared describing progressively better techniques for specimen processing, as the transmission electron microscope became easier to use and more widely available.

Transmission electron microscopy TEM can be used to study the growth of layers, their composition and defects in semiconductors. High resolution can be used to analyze the quality, shape, size and density of quantum wells, wires and dots. TEMs can magnify objects up to 2 million times. Thus, TEMs can reveal the finest details of internal structure - in some cases as small as individual atoms. That is why TEM is a very powerful tool for material science to observe the features of very small specimens. The TEM setup employs a fine electron beam, created by a high-voltage, electric current-heated tungsten filament, focused by magnetic lenses. The technology uses an accelerated beam of electrons, which passes through a very thin specimen and the interactions between the electrons and the atoms can be used to enable a scientist to visualize specimens, observe features such as structure and morphology and generate a highly-magnified image. Chemical analysis can also be

performed. Once the image is finally focused with the magnetic lenses, the film is exposed or the image is captured with a digital camera.

Figure 7 displays the schematic diagram of the components of a TEM. It has four essential systems:

- ***Electron gun and condenser system:*** A hairpin tungsten filament of an electron gun, encased in a column at high vacuum, is heated to generate a cloud of electrons, which is accelerated through a hole in an anode to produce a narrow beam that is fired towards the specimen. This beam is focussed onto the object in the form of a small, thin, coherent beam by the condenser system. This system consists of electromagnetic lens having a high aperture that eliminates high angle electrons. The gun accelerates the electrons to extremely high speeds using electromagnetic coils and voltages of up to several million volts. TEMs employ a high voltage electron beam in order to create an image.

- ***Vacuum system:*** Another component of the TEM is the vacuum system, which is essential to ensure electrons do not collide with gas atoms. A low vacuum is first achieved using either a rotary pump or diaphragm pumps which enable a low enough pressure for the operation of a diffusion pump, which then achieves vacuum level that is high enough for operations. High voltage TEMS require particularly high vacuum levels and a third vacuum system may be used. TEM operates under high vacuum in order to minimize the scattering.

- ***Image-producing system:*** This consists of the objective lens, movable specimen stage, and intermediate and projector lenses, which focusses the electrons passing through the specimen to form a real, highly magnified image. The beam then strikes the specimen and parts of it are transmitted depending upon the thickness and electron transparency of the specimen. The objective lens focuses the portion of the beam that is emitted from the sample into an image. The objective lens is usually of short focal length and produces a real intermediate image that is further magnified by the projector lens or lenses. The quality of the final image in the electron microscope depends largely upon the accuracy of the various mechanical and electrical adjustments with which the various lenses are aligned to one another and to the illuminating system.

- ***Image recording system:*** The image-recording system usually consists of a fluorescent screen for viewing and focusing the monochromatic electron image and a digital camera for permanent records. An image of the specimen with its assorted parts shown in different shades according to its density appears on the screen. The darker areas of the image represent those areas of the sample that fewer electrons are transmitted through while the lighter areas of the image represent those areas of the sample that more electrons were transmitted through. The image produced by the TEM is called a micrograph.

Specimen preparation:

A TEM specimen must be thin enough to transmit sufficient electrons to form an image with minimum energy loss. Therefore, specimen preparation is an important aspect of the TEM analysis.

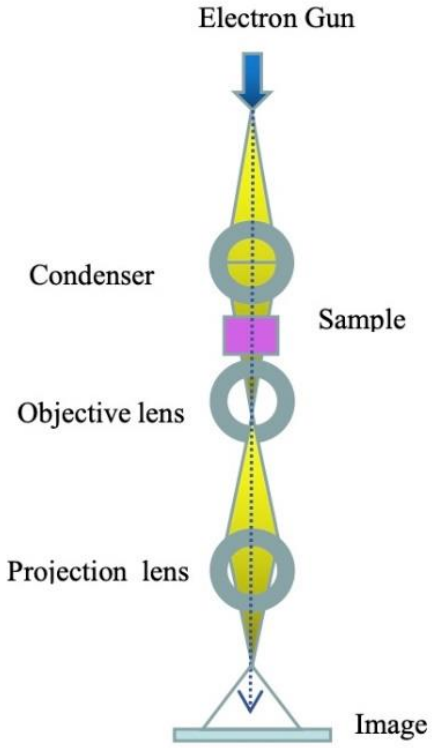

Figure 7. Schematic diagram of the components of a TEM.

Limitations:

When considering using TEM as a diagnostic or research tool, one must appreciate its limitations. First and foremost, it routinely provides a black-to-white scale, two-dimensional image.

4. Vibrating Sample Magnetometer (VSM)

A magnetometer is an instrument to measure the intensity of the magnetic moment. The most commonly used magnetometric technique to characterize magnetic materials is vibrating sample magnetometry (VSM). VSM is a very sensitive, accurate, precise and versatile technique to measure the magnetic moment as a function of magnetic field. It works on the principle of Faraday's law of magnetic induction stating that a time changing of magnetic moment will produce a voltage drop. Finally magnetic materials having a high magnetic

moment are not defined as permanent magnet. Its definition is more complex and roughly speaking they are able to retain a high magnetisation value when demagnetized. VSMs can measure the magnetic properties of magnetically soft (low coercivity) and hard (high coercivity) materials in many forms: solids, powders, single crystals, thin films, or liquids. They can be used to perform measurements from low to high magnetic fields and temperatures. And, they possess a dynamic range extending from 10^{-8} emu (10^{-11} Am^2) to above 10^3 emu (1 Am^2), enabling them to measure materials that are both weakly magnetic (ultrathin films, nanoscale structures, etc.) and strongly magnetic (permanent magnets). The measurement of the hysteresis loop of a sample, i.e., magnetization as a function of applied field, gives the idea about the usefulness of the material by deducing its saturation magnetization, coercivity, remanence, permeability and susceptibility as well as the variation of magnetization with temperature.

Figure 8 below shows a schematic diagram of a VSM instrument. A magnetic material sample is first magnetized via a uniform external magnetic field. The sample is then sinusoidally vibrated via linear actuator or a mechanical vibrator. Due to this harmonic vibration of the sample in the uniform magnetic field voltage is induced in a stationary coil called pickup or sensing coils. The induced voltage is proportional to the sample's magnetic moment, which in turn, is directly dependent on the strength of the applied magnetic field. The current is proportional to the magnetization of the sample - the greater the induced current, the greater the magnetization. Typically, the induced voltage is measured via a lock-in amplifier where the output is used to generate the hysteresis curve of a material during the sweep of the applied external magnetic field. It is thus the detection coil geometry and configuration which decides the sensitivity of measurement. By employing electromagnetism principles, the induced voltage in the detection coil can be calculated.

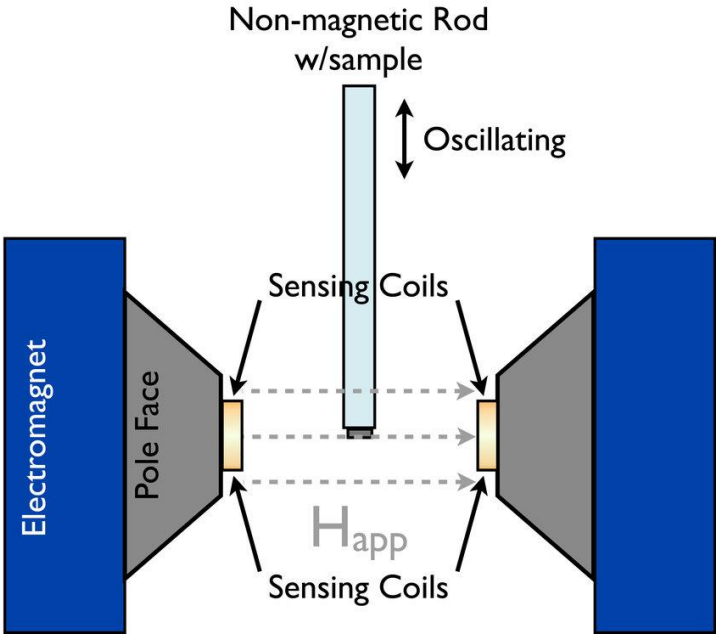

Figure 8. Schematic representation of a VSM instrument.

MODELLING TECHNIQUE

CALPHAD Method:

While designing new materials and their manufacturing processes, understanding of phase equilibria and the underlying thermodynamics is crucial. In this view, phase diagrams easily serve as roadmaps for materials development. But the graphical representation of materials consist of more than two or three components becomes quite challenging which limits their usefulness. Moreover, the phase diagrams for many multicomponent systems are only partially known. To tackle this issue, The CALPHAD (CALculation of PHAse Diagrams) method comes into the picture. This method is a powerful tool based on a parametric description of the Gibbs free energy as a function of temperature and composition. It allows to calculate a phase diagram based on experiments and thermodynamic analysis. The basis of this approach is the fact that a phase diagram is a manifestation of the equilibrium thermodynamic properties of the system, which are the sum of the properties of the individual phases, so this method assesses the thermodynamic properties of all the phases in a system to construct the phase diagram of the concerned system. It is employed to model thermodynamic properties for each phase and simulate multicomponent phase behaviour. Thus, it enables the development of thermodynamic and property databases, that in conjunction with extrapolation methods of the descriptions of binary and ternary systems to higher-order systems, allow the calculation of data for higher-order systems. It has become paramount for studying the alloy development, process design, microstructure evolution and prediction of material properties.

REFERENCE:

Following books have been referred to explain the techniques in this chapter:
1. Materials Science and Engineering, William Callister, 2014.
2. Engineered Nanoparticles - Ashok K. Singh, 2016.
3. Nanoparticle Technology Handbook - Makio Naito, Masuo Hosokawa, Toyokazu Yokoyama, Kiyoshi Nogi, 2018.

Chapter III

NANOSTRUCTURED MOLYBDENUM OXIDES

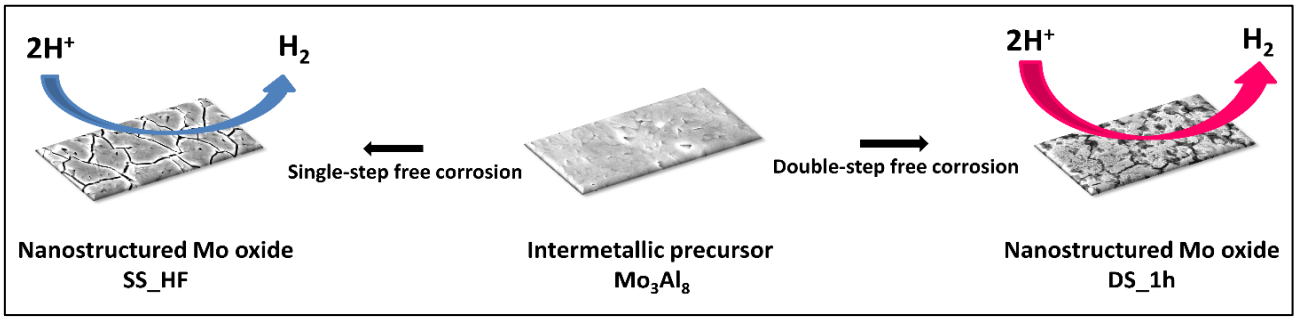

1. Introduction

Nanostructured materials have attracted great interest recently and have been found to possess a lot of technological applications in various fields such as catalysis, actuation, sensors, molecular sieves, fuel cell and surface-enhanced Raman scattering (SERS). [1] Characterized by a large surface area to volume ratio and enhanced catalytic properties[2,3] along with other unique mechanical, physical and chemical properties, nanostructured materials have emerged to be excellent candidates as electrocatalysts for HER.

Nanostructured metals and metal oxides possess enhanced surface area and augmented chemical and physical properties [2,4]. The main and easy route to obtain a nanostructured material starting from an alloy is the chemical or electrochemical etching conducted by means of aqueous media. In accordance with the alloy's initial composition and the applied condition, i.e., type, concentration, pH and temperature of the electrolyte, time of treatment, corrosion can be classified as general corrosion when the alloy is dissolved completely in the etching solution or selective when just one component of the alloy is maintained after the etching. The selective etching process can cause the dissolution of the less noble element and the oxidation of the other and, in some cases the formation of a nanostructured oxide of the remaining element; this is due to the etching condition in conjunction with the natural tendency of elements, such as molybdenum, chromium and aluminium [5], to easily passivate and react with the oxygen present in the environment. In particular, Al is dissolved during the selective corrosion of Mo-Al binary systems while Mo oxidizes and formation of a continuous passive layer occurs over the surface. This passive oxide film is superiorly stable in acidic pH and loses its stability as the pH of the solution rises due to the formation of soluble surface species [6–8]. In other words, due to the formation of a highly protective oxide film, acidic electrolytes are comparatively less corrosive to molybdenum while alkaline media allows for continuous dissolution of molybdenum oxides [6,9].

Molybdenum is an attractive metal which is in widespread industrial usage owing to its excellent properties – high thermal and electrical conductivity, high melting point, low

thermal expansion, low vapour pressure and high temperature and wear resistance.[5,6,10] It is known, as an alloying element, to enhance the corrosion resistance and mechanical properties of steels.[6,11] Molybdenum compounds have an array of applications as well - gas sensors,[12] heterogeneous catalysis,[13] electrocatalysis,[12] capacitors,[12] electrochromism,[14] photochromism,[12] and lithium-ion batteries.[15] Due to the variable oxidation states of molybdenum, tuning of the crystal structure, morphology and oxygen vacancy is facilitated, which makes its oxide compounds suitable for electrochemical activities. Synthesis and analytical detection of numerous vital molecules has been successfully achieved using molybdenum oxide based heterogeneous catalysis.[16] As gas sensors, molybdenum oxides have been well applied to NO, NO_2, CO, H_2, NH_3, and other gases.[6] MoO_3 is a versatile compound with noteworthy applications in electronics, catalysis, sensors, energy-storage units, biosystems, superconductors, lubricants, thermoelectric and electrochromic systems, etc.[17,18] Variable oxidation states of molybdenum facilitate the morphology, crystal structure, and oxygen vacancy tuning, making its oxide compounds suitable for electrochemical activities. Due to the extensive variations and tunable properties, Molybdenum based materials have garnered rising interest in the electrocatalytic HER.[19,20] Chalcogenide derivatives of Mo have been evidently favorable as building blocks in nanomaterial design in photocatalysis and hydrogen evolution reaction (HER).[21] Molybdenum oxides and other compounds such as Mo_2C,[22] $MoSe_2$,[23] MoN,[24] and MoS_2[25] have been the focus of active investigation as HER electrocatalysts with MoS_2 being the most broadly studied which exhibited favourable catalytic activity.

To obtain a nanostructured Mo oxide, a binary intermetallic compound has been employed, i.e., Mo_3Al_8. Intermetallic compounds are defined as solid phases comprising of two or more metallic elements with an ordered structure and often a well-defined and fixed stoichiometry. [26–29] They have typically high melting point and are generally mechanically hard. [26,30] They have complex crystal structures which causes them to be brittle at ambient temperature. [30] The main and easy route to get a nanostructured material starting from such precursor is the chemical or electrochemical etching conducted by means of aqueous media. In accordance with the initial composition of the alloy and the applied condition, i.e., type, concentration, pH and temperature of the electrolyte, time of treatment, corrosion can be classified as general corrosion when the alloy is dissolved completely in the etching solution or selective when just one component of the alloy is maintained after the etching. For the preparation of nanostructured molybdenum oxides, selective etching process can be utilized which causes the dissolution of the less noble element and the formation of a nanostructured oxide of the remaining element; this is due to the etching condition in junction with the natural tendency of elements, such as molybdenum, chromium and aluminium,[5] to easily passivate and react with the oxygen present in the environment. In particular, during the selective corrosion of Mo-Al binary systems, when Al is dissolved Mo oxidizes and a continuous passive layer is formed over the surface. This passive oxide film is superiorly stable in acidic pH and loses its stability as the pH of the solution increases due to the formation of soluble surface species.[6–8] In other words, acidic electrolytes are comparatively less corrosive to molybdenum due to the formation of a highly protective

barrier oxide film while molybdenum oxides undergo continuous dissolution in alkaline media.[6,9]

As a clean, efficient and sustainable alternative to fossil fuels Hydrogen gas (H_2) has emerged to be of great importance for the future of energy generation and storage.[31,32] However, production of H_2 from the electrocatalytic hydrogen evolution reaction (HER) still remains a challenge and has been intensively explored using a range of materials.[33] So far, noble metals, such as platinum, have shown the best performance as HER catalysts.[31] But it comes with its drawbacks, i.e., high cost, limited availability and inadequate long-term durability due to the catalyst deactivation. [34,35] So, the development of cheap earth-abundant electrocatalysts for hydrogen evolution with elevated catalytic activity, efficiency and stability is of vast significance in the field of clean energy.[31] Efforts to fabricate and develop an efficient and durable non-Pt catalysts with comparable catalytic activity have been at the forefront in recent years for energy-related applications because of the incessant energy demand worldwide.[36] As mentioned before, characterized by a large surface area to volume ratio and enhanced catalytic properties[2,3] along with other unique mechanical, physical and chemical properties, nanostructured materials have emerged to be excellent candidates as electrocatalysts for HER. For instance, the literature shows reports on the use of molybdenum coated palladium nanocubes [37]; Au-Ni alloy nanoparticles supported on reduced graphene oxide [38]; gold aerogel supported on graphite carbon nitrite [39]; N, P co-doped carbon nanofiber networks [40]; M_3C (M: Fe, Co, Ni) nanocrystals encased in graphene nanoribbons [41] Pd-Ru nanoparticles encapsulated in porous carbon nanosheets [42]; urchin-like CoP nanocrystals [43]; Phosphorus doped MoS_2 [44]; nanostructured porous gold film [45]; anodized NPG [46]; and amorphous MoS_2 on NPG [33] among many others as alternative materials to Pt regarding HER. Due to the extensive variations and tunable properties, molybdenum-based materials have garnered rising interest in the electrocatalytic HER [19,20]. Molybdenum oxides [47,48] and other compounds such as Mo_2C [22], $MoSe_2$ [23], MoN [24] and MoS_2 [25,49] have been the focus of active investigation as HER electrocatalysts with MoS_2 being the most broadly studied which exhibited favourable catalytic activity.

This chapter focusses on producing nanostructured molybdenum oxides utilizing the strategy of selective corrosion in the quest of producing low-cost and efficient electrocatalyst for HER. The intermetallic compound Mo_3Al_8, has been selected as a crystalline precursor having the composition 28 at. % Mo and 72 at. % Al. Selective single-step and double-step free corrosion have been performed in various electrolytes with different concentrations at room temperature playing with the time of the treatment. Taking advantage of their increased surface area and typically high number of active sites, the molybdenum oxide samples obtained have been tested as non-precious electrocatalysts for the HER. The materials reported in this chapter have been obtained using comparatively cheap and abundant precursor and a simple, fast and sustainable synthetic route that does not involve the use of critical raw materials. They are characterized by a good overall HER activity, paving the way for possible application of these materials as HER electrocatalysts as cost-effective alternative to Pt-based electrocatalysts. Being free-standing and easy-to-handle materials,

they can potentially be economical and sustainable candidates for large-scale industrial production.

2. Experimental

The Mo_3Al_8 master alloy of nominal composition 28 at. % Mo and 72 at. % Al was prepared by arc-melting bars of pure elements (99.999 % Mo and Al) after evacuating and purging the furnace several times in Ti-gettered Ar atmosphere. The ingot was melt-spun from a silica crucible at a linear speed of 25 m/s onto a hardened Cu wheel in a closed chamber kept under protective Ar atmosphere.

Different trials of chemical and electrochemical corrosion were performed using electrolytes, namely 1 M KOH, 1 M HF. 1.25 M $FeCl_3$, 1 M H_2SO_4, 1 M Na_2S and piranha solution (3 parts H_2SO_4: 1-part H_2O_2) for different durations at room temperature and 70 °C. The samples reported in this paper have been obtained from single and double-step free corrosion of the as-quenched alloy ribbon performed at room temperature for durations ranging from 1 h to 24 h in 1 M KOH, 1 M HF, and 1.25 M $FeCl_3$. All electrolytes were prepared from chemical grade reagents and deionized water. This synthesis was repeated several times in order to check the reproducibility and the same results were always obtained.

Samples were analyzed before and after treatments a Panalytical X-pert X-ray Diffractometer in Bragg–Brentano geometry with monochromatic Cu Kα radiation, scanning electron microscopy (Inspect SEM, FEI), field-emission scanning electron microscopy (FIB-FESEM/EBSD/EDS/TOF-SIMS Tescan S9000G microscope) and energy-dispersive X-ray spectroscopy (Oxford Ultim-Max 100 connected with the FESEM).

The electrocatalytic activity of the obtained samples towards HER was evaluated in 0.5 M H_2SO_4 aqueous solution at room temperature, using a three-electrode cell (saturated Ag/AgCl double-bridge reference electrode, Pt-grid counter and the sample as the working electrode). Linear sweep voltammetry (LSV) was performed at 2 mV s^{-1} for comparison with the data from the literature. [50] A sheet of pure Pt (2 cm^2) was polished on the surface as per conventional metallography and used for comparison with the samples in the same experimental conditions. All potentials were reported to the reversible hydrogen electrode (RHE) adding a value of (0.199 + 0.059 pH) V. The electrochemically active surface area of the samples (ECSA) was estimated using the double layer capacitance method. [31,51,52] All measurements were performed in 0.5 M H_2SO_4 solution using a three-electrode cell similar to that utilized for the HER tests. Cyclic Voltammetry (CV) curves were obtained in the potential range of 100 mV around the open circuit potential (OCP), assuming that only non-Faradaic processes take place at the electrode-solution interface in this potential range, at scan rates of 10, 20, 30, 40, 50, 70, 90 and 100 mV/s. Then, at the middle of this potential range the current obtained in the middle of each cycle (i.e., average of the cathodic current and the anodic current) was plotted against the scan rates mentioned above. The plots

obtained are provided in Figure 12 later in the discussion. The current density was then normalized using the ECSA obtained for each sample.

3. Results and Discussion

Figure 1 (a) shows the SEM secondary electron image of the as-quenched ribbon surface that exhibits a surface morphology with narrow sheet or plate-like structures woven together and overlapped closely. This morphology can be related to the shape of the crystalline grains as they grow on the surface during rapid solidification. Therefore, the presence of grain boundaries separating neighbouring crystals is responsible for the roughness observed in Figure 1 (a). From this SEM image (Figure 1 (a)) it is possible to estimate the crystals dimension that is on average below 10 µm. This particular morphology is of interest for the next steps of synthesis of the nanostructured molybdenum oxides being roughness and grain boundaries easy places for chemical etching.

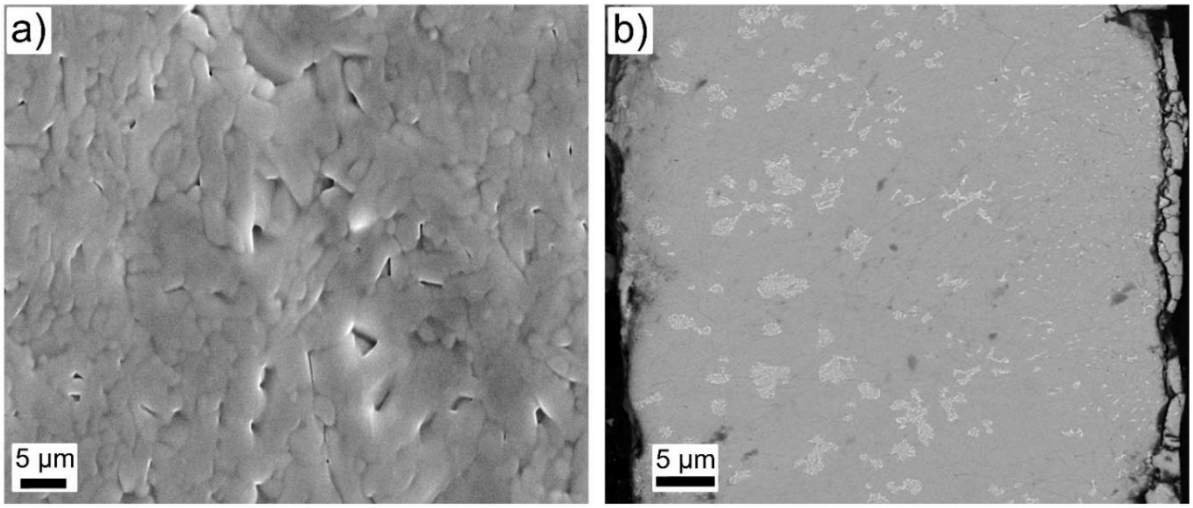

Figure 1. (a) Scanning electron microscopy-Secondary electron (SEM-SE) image of surface view of as-prepared ribbon and (**b**) SEM-back-scattered electron (BSE) image of mirror-polished cross-section of as-prepared ribbon.

Two phases were found to be present in the mirror-polished cross-section of the as-prepared ribbon, i.e., Mo_3Al_8 and $AlMo_3$, as observed in the back-scattered SEM images in Figure 1 (b), where the darker phase can be attributed to Mo_3Al_8 due to its lower average atomic number, while the lighter phase is related to $AlMo_3$. The amount of $AlMo_3$ in Figure 1 (b) is limited, meaning the composition of the master alloy ingot was just slightly above than what is required for obtaining only the linear compound Mo_3Al_8. The microstructure present in Figure 1 (b) can be clearly attributed to the formation of Mo_3Al_8 with a peritectic reaction at

high temperature, followed by a eutectoid reaction at 1838 K being present areas in which alternated lamella of Mo_3Al_8 and $AlMo_3$ are visible.

The XRD data in Figure 2 (a) show the typical patterns associated with Mo_3Al_8 intermetallic phase obtained from the wheel-side of the as-quenched ribbon. Phase determinations were made using Standard ICDD (International Centre for Diffraction Data) card no. 03-065-6867 for Mo_3Al_8 and 03-065-4685 for $AlMo_3$. A textural effect at (-312) and (401) reflections are observed in the pattern taken from the air-side (Figure 2 (b)): solidification front starts in the region of the ribbon which is in direct contact with the wheel of the melt- spinning apparatus and then proceeds in the direction along which the heat is subtracted during the rapid quenching process, causing an orientation of crystals.

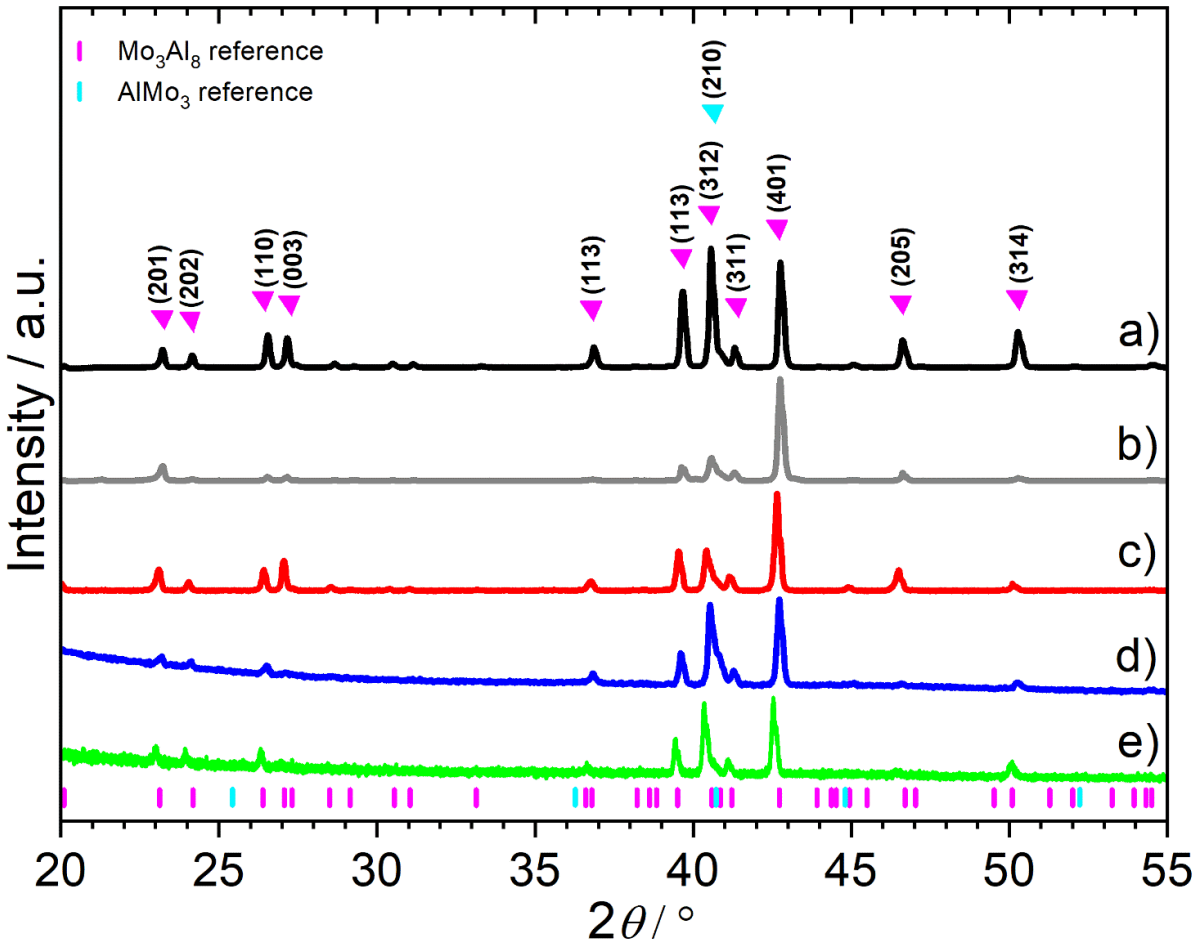

Figure 2. X-ray diffraction (XRD) pattern of (**a**) the wheel-side of the as-quenched ribbon; (**b**) the air-side of the as-quenched ribbon; (**c**) the air side of the sample obtained by single-step free corrosion in 1 M KOH at room temperature for 6 h (denoted as SS_KOH); (**d**) wheel side of the sample obtained by single-step free corrosion in 1 M HF at room temperature for 24 h (denoted as SS_HF) and; (**e**) wheel side of the sample obtained by double-step free corrosion first in 1.25 M $FeCl_3$ for 1 h and then in 1 M HF for 6 h both at room temperature (denoted as DS_1h).

The composition of the as-spun ribbon was carefully analyzed by means of EDS, performing average spot analyses, compositional maps and line scans. The EDS spectrum (Figure 3 (a)) presents the main Al and Mo peaks; the average composition was determined to be 32 at. % Mo and 68 at. % Al with a standard deviation of 3 at. %. The EDS compositional maps show a widespread and uniform presence of Al and Mo throughout the surface of the as-spun ribbon. Obviously, more Mo was found in the $AlMo_3$ minority phase. The line scan data (Figure 3 (b)) portrays a uniform trend in the Al and Mo intensity signals interrupted by a jump in the composition when the scanning line intercepts the $AlMo_3$ phase. This observation further supports the findings from the SEM images and XRD analyses described above.

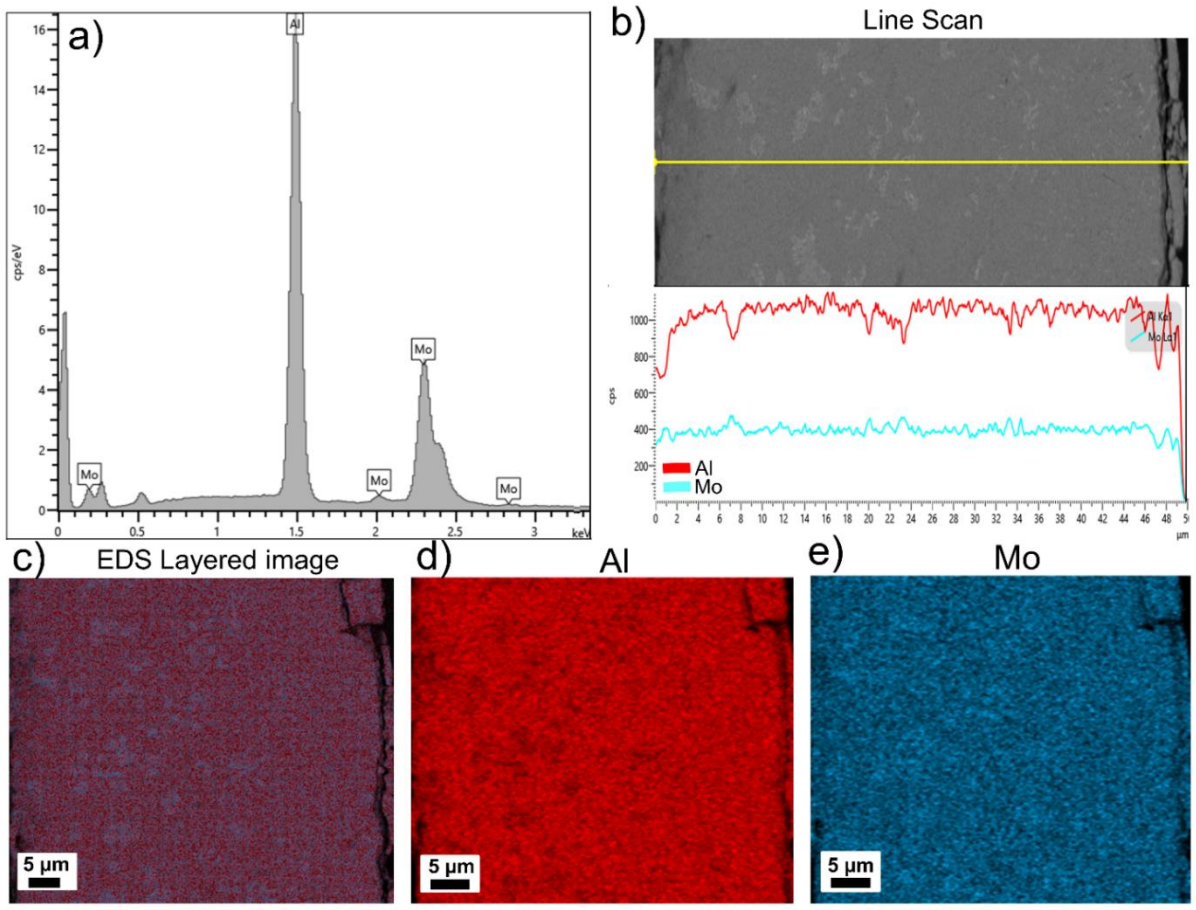

Figure 3. Energy-dispersive X-ray spectroscopy (EDS) analyses of the cross-section of the as-quenched ribbon: (**a**) EDS spectrum; (**b**) Line scan—red signal for Al and cyan signal for Mo; (**c**) Layered compositional map depicting Mo and Al content; (**d**) Map showing only Al content and; (**e**) Map showing only Mo content.

3.1. Free Corrosion

A number of trials of chemical and electrochemical corrosion were performed using an array of electrolytes for different durations at room temperature and 70 °C, as mentioned above in

the Experimental section. Some of the obtained samples suffered from an excess of embrittlement and the SEM images can be found in Figure 4. These samples were not further studied being the goal of this study to propose mechanically stable, free-standing and easy-to-handle materials. In this respect, the most promising samples, in terms of mechanical stability and desired composition, turned out to be the ones prepared by single-step and double-step free corrosion using KOH, HF and $FeCl_3$ at room temperature varying the time of the treatment as demonstrated in scheme 1. KOH and HF were selected as the etching electrolytes for selective corrosion of Al. $FeCl_3$ was used in the first step of the double-step free corrosion treatment to add another level of corrosion and facilitate nanostructuration in the morphology of the ribbon.

From here onwards the samples have been denoted in the following manner - the sample prepared by single-step free corrosion in 1 M KOH at room temperature for 6 h is SS_KOH; the sample prepared by single-step free corrosion in 1 M HF at room temperature for 24 h is SS_HF; the sample prepared by double-step free corrosion first in 1.25 M $FeCl_3$ for 1 h and then in 1 M HF for 6 h both at room temperature is DS_1h and; the sample prepared by double-step free corrosion first in 1.25 M $FeCl_3$ for 3 h and then in 1 M HF for 6 h both at room temperature is DS_3h.

3.1.1. Single-Step Free Corrosion

With the intent to remove the maximum amount of Al and induce the nanostructural roughening in the whole thick ness of the sample, free corrosion was performed in 1 M KOH for 6 h at room temperature and the obtained sample was characterized.

The XRD pattern of the air-side of SS_KOH (Figure 2 (c)) resembles that of the air-side of the as quenched ribbon (Figure 2 (b)). The surface of the as-treated sample, SS_KOH (Figure 5 (a)) is divided into crack patterns of micrometric size. Cracks could be due to stress corrosion and differences in volume between the pristine intermetallic alloy and the formed oxides. The inset of Figure 5 (a) reports a magnified image of the sample surface where a rough morphology can be observed, spread from the top of the patterned surface and extended only up to a few microns inside the cross-section. As for the rest of the cross-section, no nanostructured morphology was observed. From the compositional analysis by EDS, it is revealed that the ratio Al/Mo on the surface and in the cross-section of the as-treated sample is similar to the ratio Al/Mo of the as-quenched ribbon. As a result, no selective corrosion was achieved but a general corrosion with the formation of a scale composed by mixed Al and Mo oxides. By contrast, in XRD, just the pristine intermetallic alloy was observed. This could be explained by the low scattering factor of oxides with respect to metals and to the low symmetry of the Mo_3Al_8 phase. On one hand the oxides have a low scattering intensity with respect to metals, while on the other, weak peaks related to the oxide phases can be superimposed by the high number of peaks related to the Mo_3Al_8 phase. The effect of a different electrolyte was studied by using 1 M HF. High temperature treatment was avoided as it would be too harsh for the sample causing brittleness and worsening its

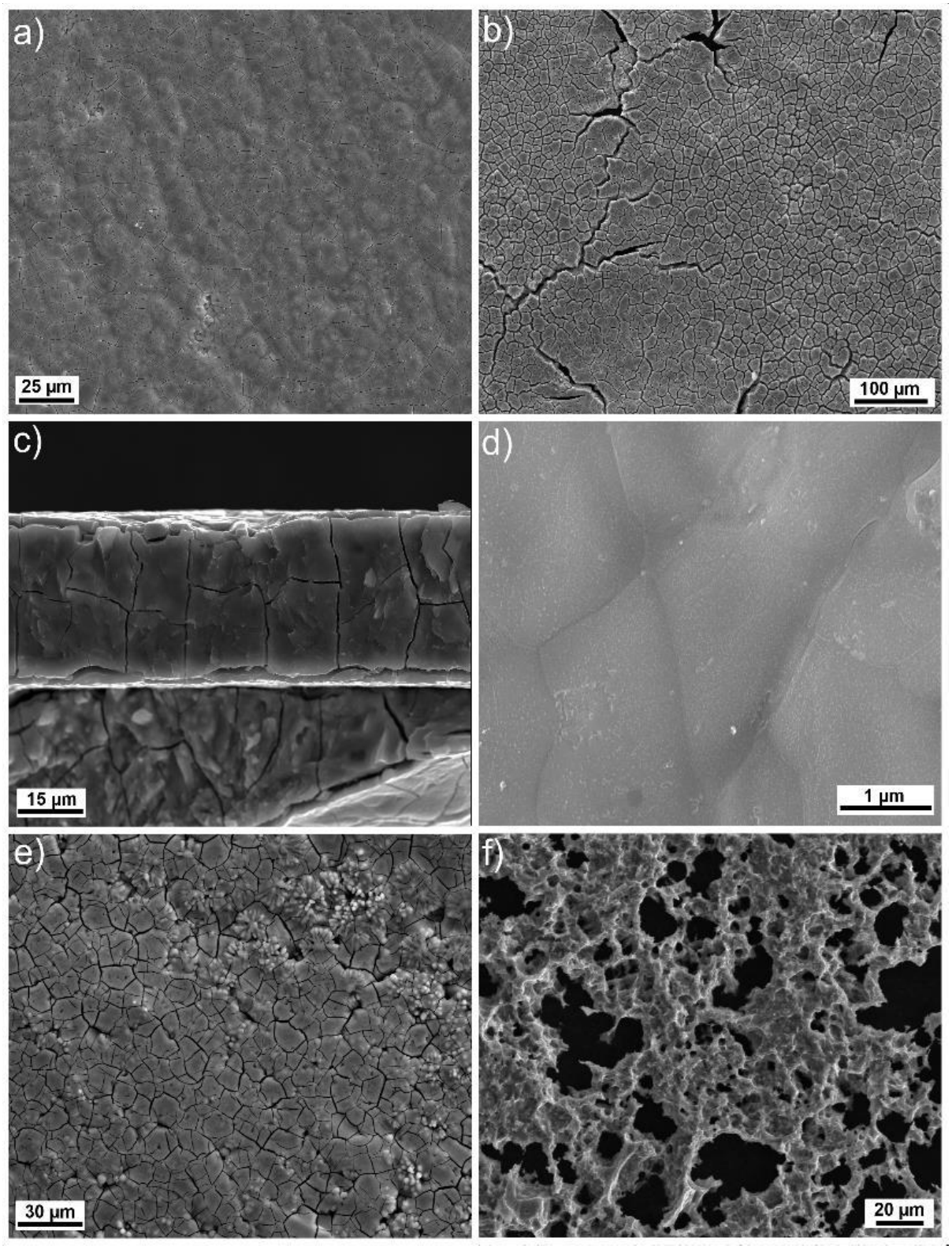

Figure 4. SEM images of sample obtained by (**a**) free corrosion in 1 M KOH for 6 h at 70 °C; (**b**) electrochemical corrosion at 0.8 V in 1 M KOH for 2 h at room temperature; (**c**) electrochemical corrosion at -0.4 V in 1 M HF for 1 h at 70 °C; (**d**) electrochemical corrosion at 0.15 V in 1 M H_2SO_4 for 1 h at 70 °C; (**e**) free corrosion in 1 M Na_2S for 6 h at 70 °C; and (**f**) free corrosion in piranha solution (3:1) for 18 h at room temperature.

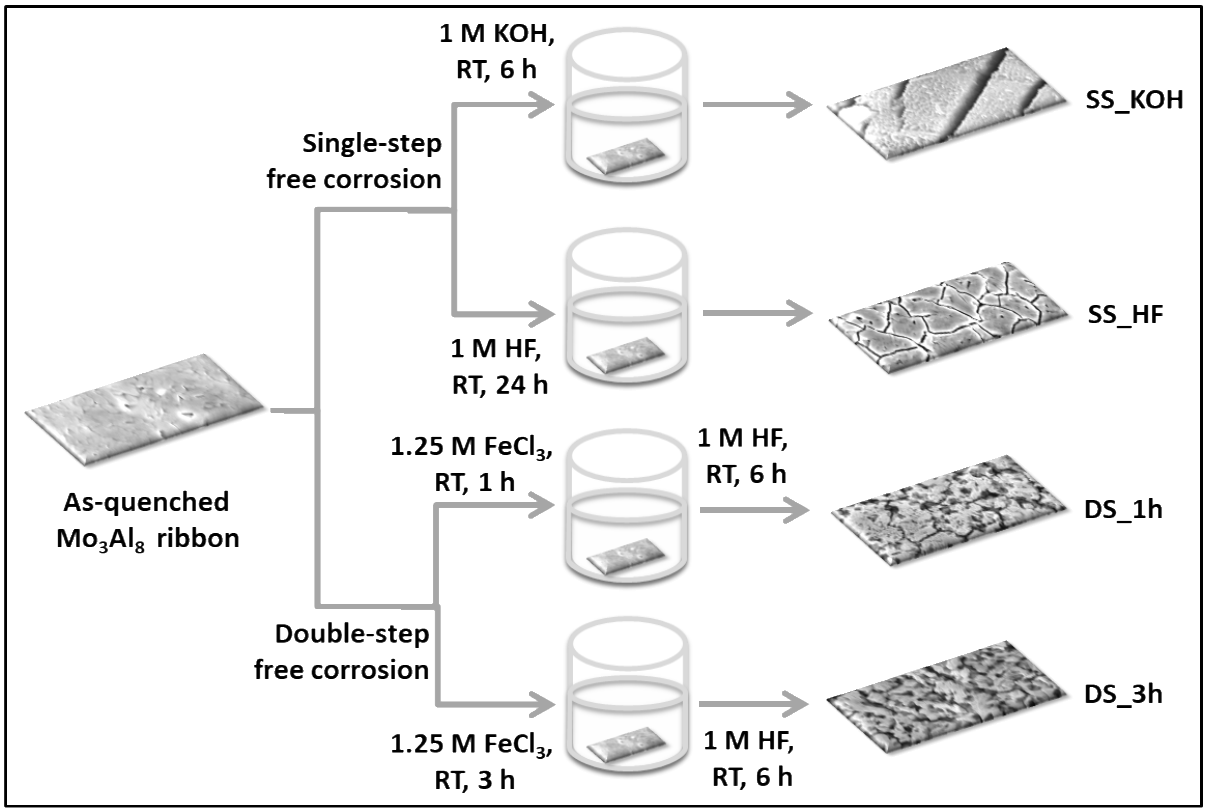

Scheme 1. Scheme demonstrating the overall free corrosion process.

stability. Accordingly, free corrosion was performed at room temperature in 1 M HF for 6 h but no appreciable formation of Mo oxides was obtained. When the treatment time was increased to 24 h, the surface of the resultant sample (named SS_HF) was observed to be cracked, as already seen in the previous case, but inside the patterned region a compact layer of Mo oxides is present (Figure 5 (b)). This cracked pattern is not extended in the whole cross-section of the ribbon but only up to about 9 microns approximately (Figure 5 (c)).

The XRD pattern shown in Figure 2 (d) presents a likeness to that of the wheel side of the as-quenched ribbon (Figure 2 (a)) due to similar reason explained for the previous sample. In the EDS line scan of SS_HF in Figure 6 it can be seen that starting from the left part of the cross-sectional image the counts per second (cps) signals for Mo (in cyan) and Al (in blue) maintain their intensity as the scan continues along the thickness of the sample represented by the yellow line on the cross-sectional image. As soon as a void is encountered due to the inhomogeneity of the sample, there is a fall in both the signals. After crossing the void area, both the signals jump to their usual intensities. Towards the outer edge of the cross-section, highlighted by the red line segment A, oxygen signal in green comes into the picture (within the red box A). Mo signal is slightly enhanced while Al signal is reduced drastically. This suggests the formation of the Mo oxide. In Figure 7 (a) the compositional analysis of the cross-section of SS_HF done by EDS has been shown in the form of mappings. It can be seen

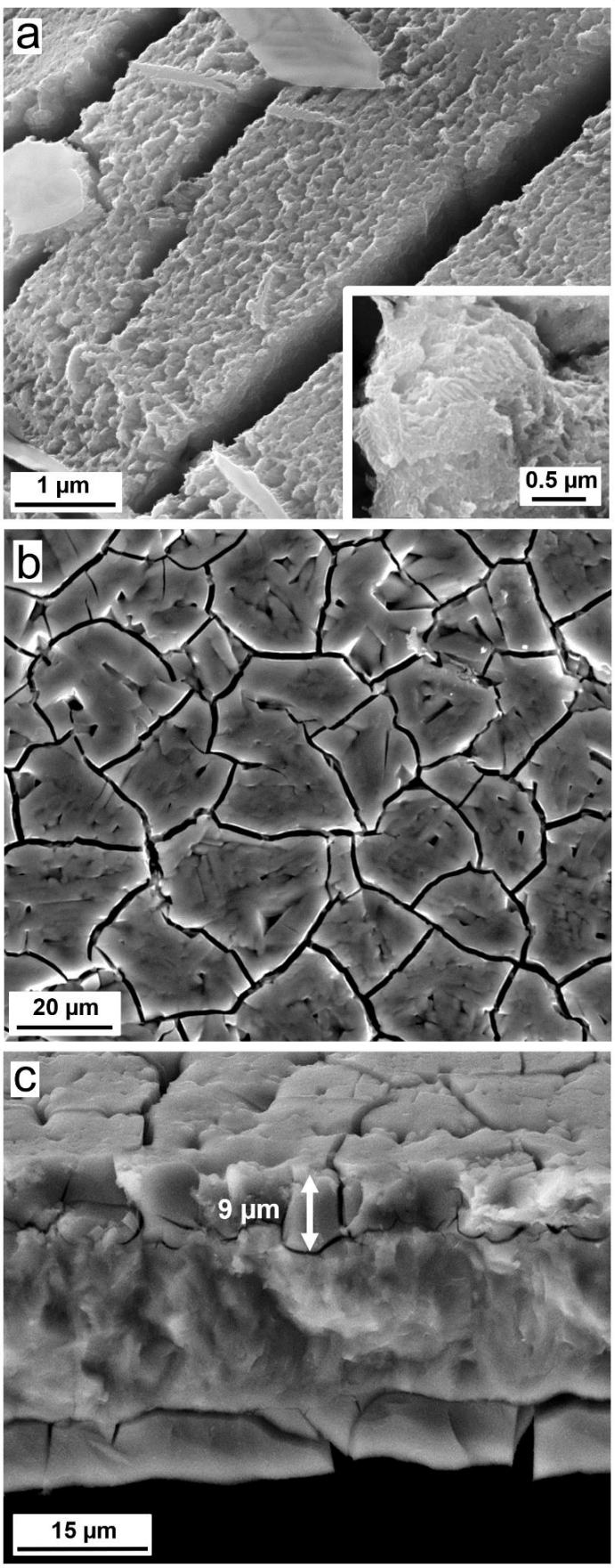

Figure 5. SEM images of (**a**) surface view of SS_KOH, (**b**) surface view of SS_HF and (**c**) cross-sectional view.

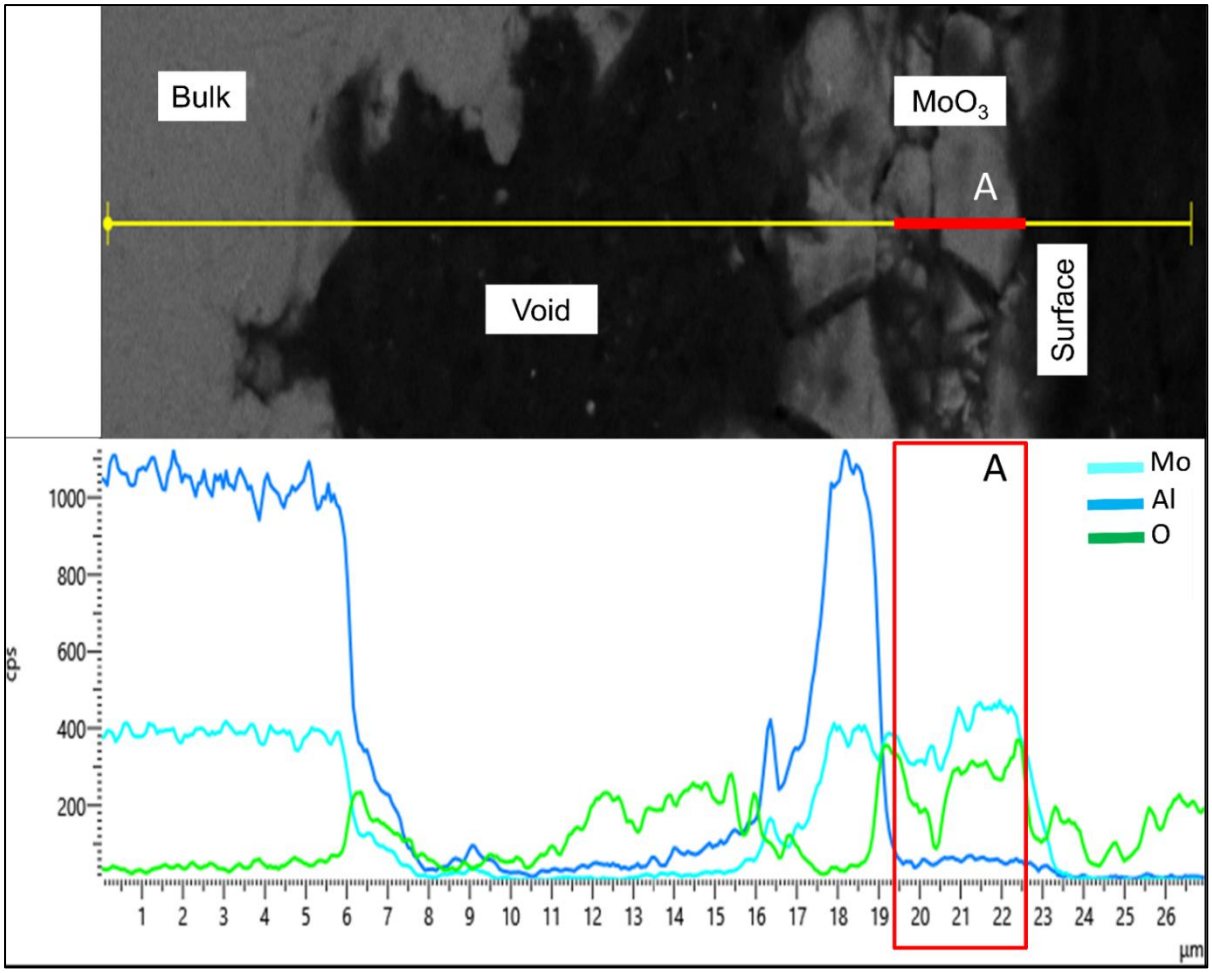

Figure 6. EDS line scan of SS_HF: blue signal for Al, cyan for Mo and green for O.

that the selective corrosion has only taken place on the outer edge of the cross-section (highlighted by a mix of green and cyan colours) which represents the surface of the sample. A prominent attendance of oxygen is displayed in the corroded region along with the abundance of Mo. This implies that this corroded edge is composed of Mo oxide. Also, there are no notable traces of Al in this corroded layer. And, the bulk of the cross-section lacks any signs of corrosion as the Al and Mo compositions are not depleted and oxygen is absent. The EDS analysis shows the presence of MoO_3 on the edges. Figure 6 (b–d) display the elemental maps of Mo, O and Al further clarifying the scenario in which Mo and O are prominently present on the outer edge while Al has disappeared.

The explanation for the behaviour observed in both the above samples, i.e., SS_KOH and SS_HF, can be attributed to the specific reactivity of Al and Mo in the experimental conditions applied for the selective corrosion treatment, i.e., 1 M KOH (pH = 14) and 1 M HF (pH = 1.56) respectively. A superimposed Pourbaix diagram showing the regions of stability, passivation and corrosion of both elements has been reported in Figure 8 (a). [6] It depicts that Mo dissolves in aqueous solutions with neutral-to-alkaline pH due to the

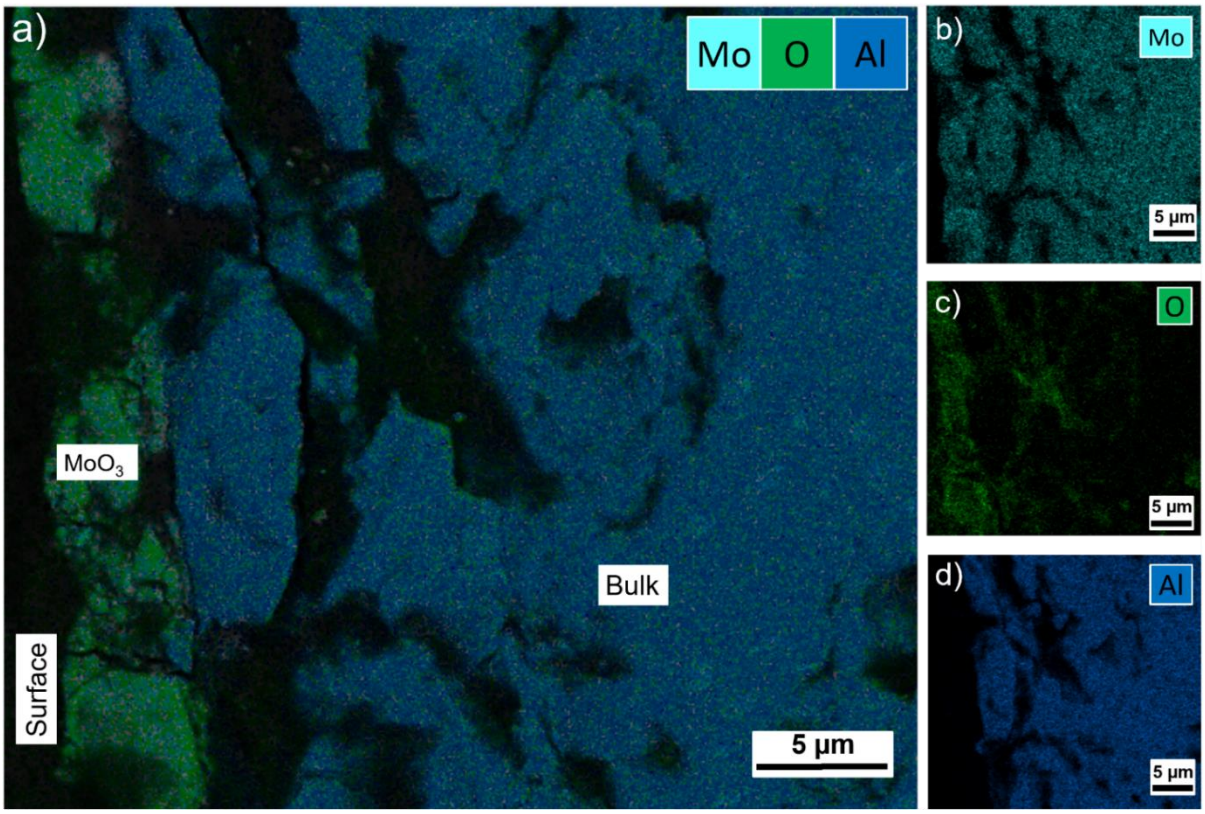

Figure 7. EDS analysis of SS_HF: (**a**) layered compositional map depicting Mo, O and Al content; (**b**) Mo elemental map; (**c**) O elemental map; and (**d**) Al elemental map.

amplified stability of molybdenum oxyanions.[5,53] In a strongly basic condition and at a potential higher than -0.89 V vs. SHE, Mo is unstable in the metallic state and is converted to molybdate (MoO_4^{2-}) ion while for a wider range of potential Al is fully corroded. Figure 8 (b) shows the open-circuit potentials vs SHE of the pure Al and Mo, and the as-quenched Mo_3Al_8 ribbon. In 1 M KOH (Figure 8 (b), solid lines) the open-circuit potentials are found to be 1.42 V, -0.33 V and -0.62 V, respectively, for pure Al and Mo, and as-quenched ribbon meaning that the pure elements and the ribbon are all in the condition of corrosion. Moreover, molybdenum is only weakly resistant to hydroxides [5] and oxidizing alkalis convert it into molybdate.[54] Hence, the morphology observed under alkaline etching in case of SS_KOH, in agreement with XRD and EDS results, is due to a general corrosion rather than a selective corrosion process.

In the case of SS_HF, Figure 8 (b) represents the OCP curves obtained for pure Al and Mo, and the as-quenched Mo_3Al_8 ribbon in 1 M HF in dot-dashed lines. The OCP value of -1.15 V for pure Al lies in the corroded region of the Pourbaix diagram and that of 0.28 V for pure Mo lies in the oxidized region. The Pourbaix diagram shows that in aqueous solutions with acidic pH, Mo forms passive oxides on its surface.[5,53] While Al is corroded in the strongly acidic condition (pH $\leq$ 2), a value of E_{ocp}= -0.22 V vs. SHE measured for the as-quenched ribbon falls in the region of Mo^{3+} ions. This means that being in acidic media, at first Mo^{3+}

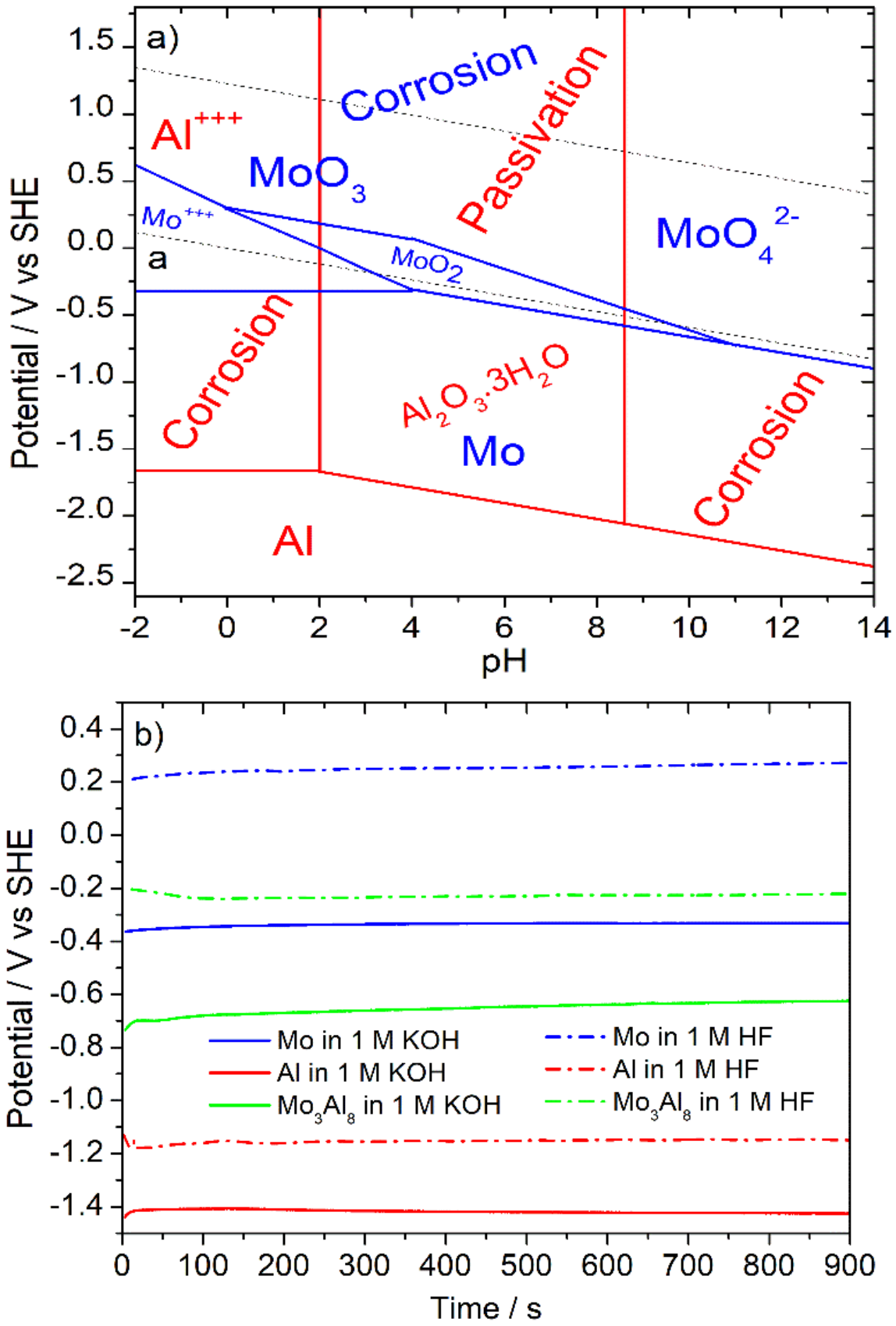

Figure 8. (a) Superimposed Pourbaix diagrams of pure Al and Mo showing the regions of stability, passivation and corrosion of each element. (**b**) Evolution of the open-circuit potential of pure Al and Mo, as references, and the as-quenched Mo_3Al_8 ribbon.

ions are formed at relatively low electrode potentials and then as the reaction proceeds the surface is covered with a passivating layer of MoO_2 or MoO_3.[54] In addition, molybdenum does not dissolve appreciably in non-oxidizing acids and is relatively unaffected by the presence of halide ions, relatively resistant to most localized corrosion processes.[5,54] Therefore, it has good performance in hydrohalide acids, i.e., HF in this case.[5] As a consequence, selective corrosion takes place where Al is dissolved on the top surface while Mo undergoes oxidation and forms a compact passive oxide layer on the terraces which results in the formation of nanostructured molybdenum oxides.[7,53]

3.1.2. Double-Step Free Corrosion

The double-step free corrosion was undertaken with the intention that applying dedicated individual steps of general and selective corrosion would result in a Mo oxide-rich product with improved nanostructural morphology and surface area. The first step of the treatment was particularly dedicated to corrode and expose the surface using a corrosive electrolyte. This would cause roughness and simultaneously remove stable Al and Mo oxides covering the sample surface that can impede the dissolution process. The second step was targeted to remove the Al content via selective corrosion with the help of a suitable electrolyte.

For the first step, $FeCl_3$ was chosen which is a well-known corrosive agent and has been reported in literature as being successfully used as an etchant for Al and its alloys.[55] In addition, oxidizing conditions severely reduce molybdenum's corrosion resistance, and aeration causes a significant boost in corrosion.[5] Therefore, $FeCl_3$, being a reducing acid containing oxidizer, rapidly attacks molybdenum.

The as-quenched ribbon was treated in 1.25 M $FeCl_3$, chosen from literature, at room temperature from 1 h to 8 h.[55] Only the samples obtained after 1 h and 3 h of treatment were taken into account as the rest suffered from brittleness due to the prolonged treatments. However, the observed pitting corrosion was limited to the surface of the obtained samples.

Considering the effect of HF in eliminating high amounts of Al observed for sample SS_HF as previously described, 1 M HF was used for the second step and the free corrosion was performed for 6 h at room temperature for the samples treated for 1 h and 3 h, namely DS_1h and DS_3h respectively. From the SEM images of DS_1h (Figure 9 (a, b)) it can be observed that the sample acquired an inhomogeneous porosity as a result of pitting corrosion. After 6 h of treatment in HF, the sample was affected by the electrolyte on a surface layer of 3 µm. The composition was measured by the EDS which showed the presence of MoO_3 on the surface. Figure 10 presents the line scan analysis of the cross-section in which the trends are similar to that already seen in the case of SS_HF. The cps signals for Mo (in cyan) and O (in green) are visible in the outer region of the cross-section (highlighted by the red line segment B and red box B) with negligible Al signal indicating the presence of Mo oxide. Continuing the scan, the oxide layer is passed by and the pristine phase appears which is demonstrated by the fall in O signal and simultaneous emergence of Al signal along with a slight decrease in Mo

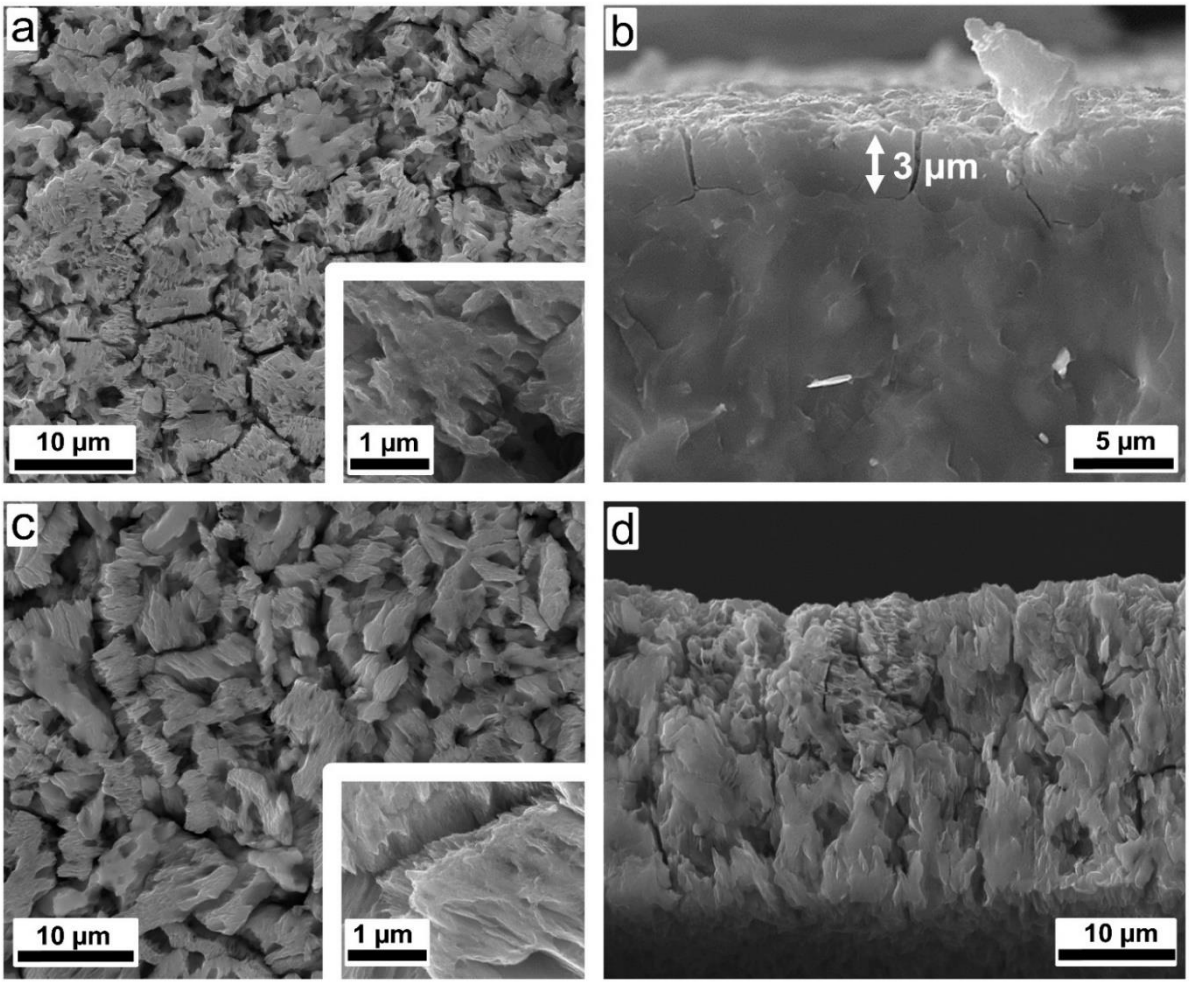

Figure 9. SEM images (on the left: surface view; on the right: cross-sectional view) of (**a**,**b**) DS_1h and (**c**,**d**) DS_3h.

signal. The signals drop throughout the existence of the void which rise back once the void is crossed and the pristine phase prevails. The Mo signal in cyan retains its intensity throughout the cross-section demonstrating no significant decrease in the Mo concentration in the volume of the sample, suggesting that Mo is resistant to dissolution by HF and, rather, forms a passive oxide layer. It other words, the chemical etching using 1 M HF did not reduce the concentration of Mo but Al content has been notably removed by the etching treatment in a 3 µm layer where Mo oxides have formed. Thus, HF has only acted upon Al, as intended, selectively eliminating it and facilitating formation of Mo oxides. As analysed earlier in Section 3.1.1. 'Single-step free corrosion', the Pourbaix diagram (Figure 8 (a)) validates this observation. Based on the OCP values of pure Al and Mo from Figure 8 (b), i.e., -1.15 V and 0.28 V vs SHE respectively, pure Al lies in the corroded region of the diagram while pure Mo lies in the oxidized region. This means that treatment of the as-quenched ribbon (OCP = -0.22 V) with 1 M HF results in selective corrosion with Al being corroded while Mo undergoes oxidation forming a passivating layer of nanostructured Mo

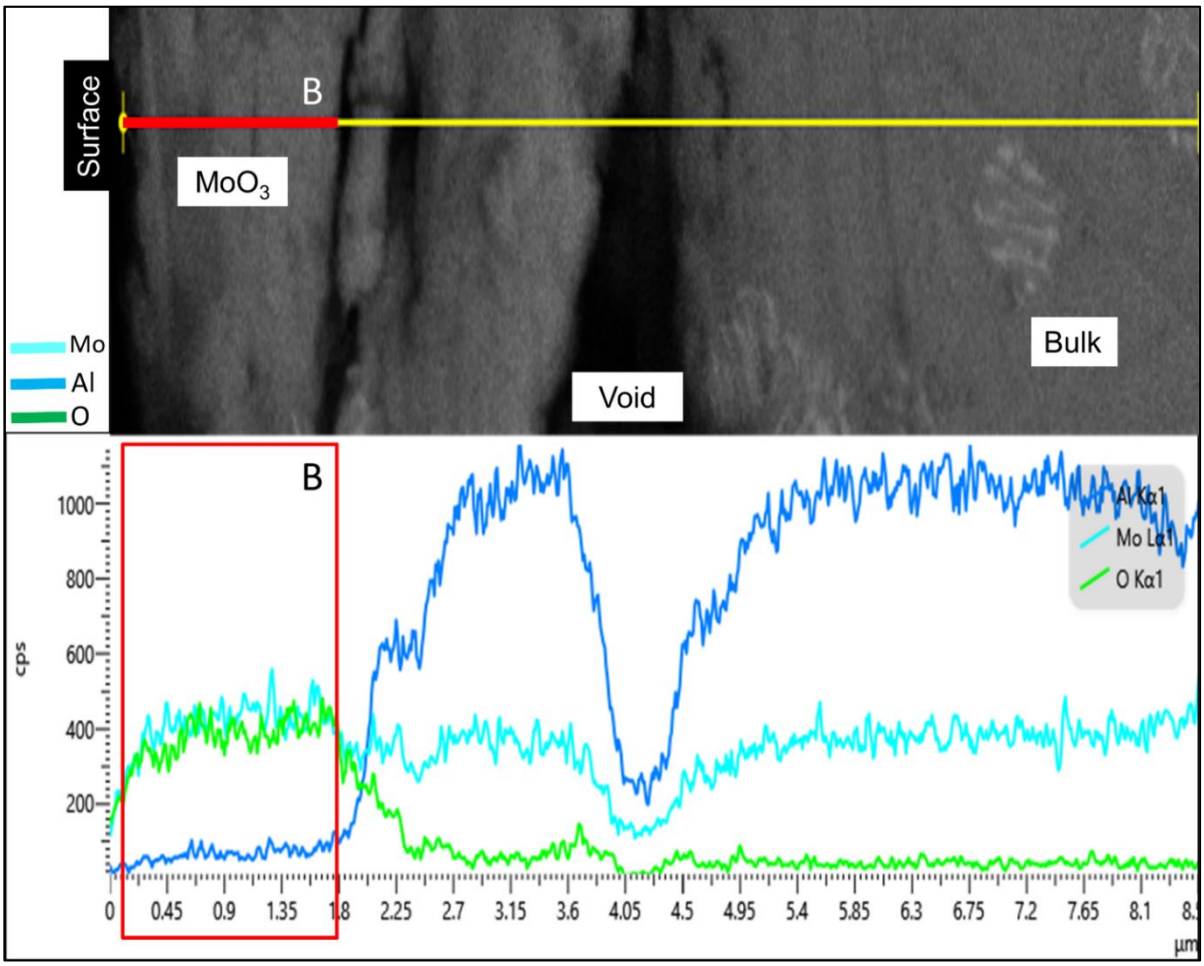

Figure 10. EDS line scan of DS_1h: cyan for Mo, blue signal for Al and green for O.

oxides. Figure 11 (a) shows the Mo-oxide-rich outer-region of the cross-section highlighted by the mix of cyan and green signals for Mo and O respectively. Figure 11 (b–d) display the elemental maps of Mo, O and Al that add up to the overall observation of the presence of Mo oxide on the sample surface. The bulk of the cross-section is protected from the corrosion as shown by the unchanged Al and Mo compositions, the Mo and Al signals in the line scan and the elemental maps.

In the case of DS_3h, the SEM images (Figure 9 (c,d)) display a more homogeneous nanostructural surface with nanoplates. This can be linked to the extended duration of the first step of the corrosion process that increased the depth of etching and facilitated constant and stable treatment.[55] For the same reason a slightly nanostructural morphology can be noticed in the cross-section as well. The EDS results confirm the high content of Mo oxide on the surface by the action of HF in the second step. Observing this carefully, it can be inferred that the resultant microstructure resembles the as-quenched ribbon morphology. The corrosion must have started around the boundaries of the plate-like grains and the defects on the surface of the as-quenched ribbon (as shown in Figure 1 earlier). As a result, there is the

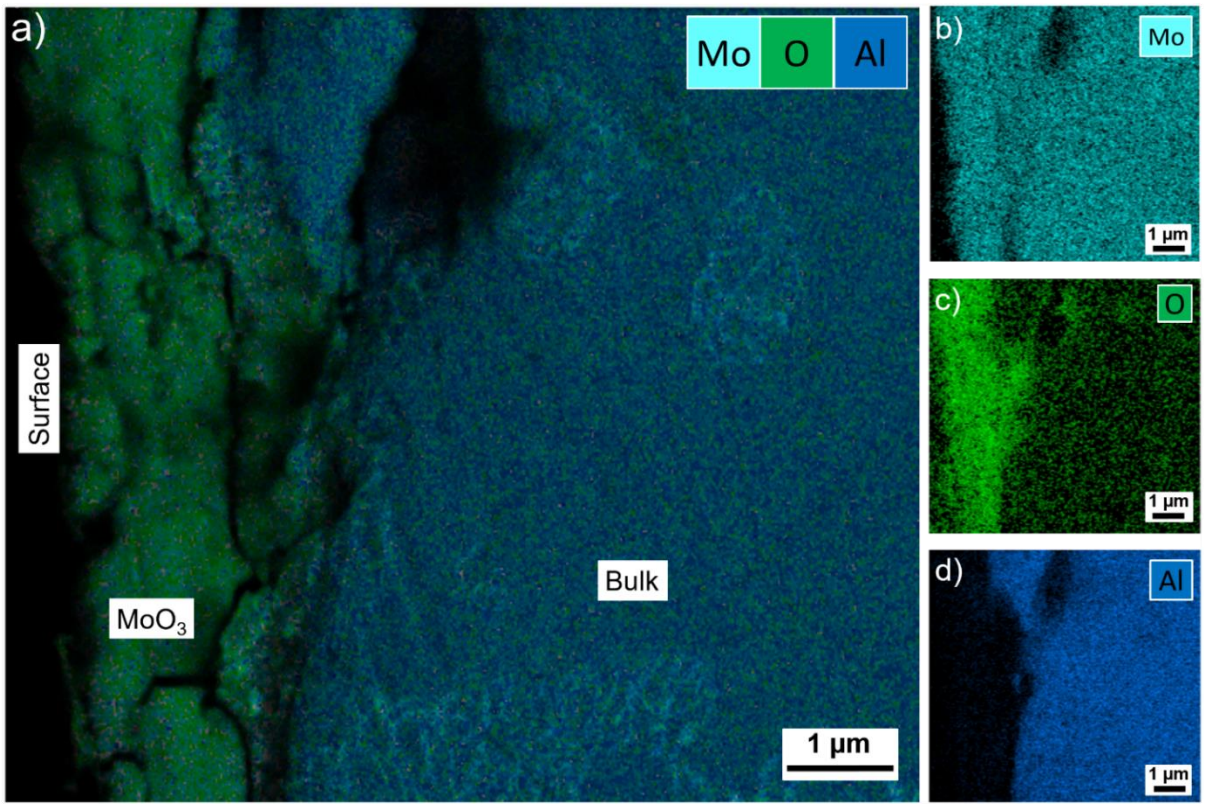

Figure 11. EDS analyses of DS_1h: (**a**) layered compositional map depicting Mo, Al and O content; (**b**) Mo elemental map; (**c**) O elemental map and; (**d**) Al elemental map.

formation of nanoplates along with grooves in the microstructure. The overlapping and compactness have been reduced compared to that in the as-quenched ribbon. The nanoplates also pose a roughened and layered texture increasing their surface area.

From the XRD data of DS_1h (Figure 2 (e)) it is revealed that the obtained pattern largely mimics that of the as-quenched ribbon (Figure 2 (a). This is due to the negligible contribution of the 3 µm layer of Mo oxide to the XRD pattern as it has been overlapped by the major contribution of the Mo_3Al_8 intermetallic phase present in the bulk and to the low scattering factor of oxides with respect to metals as previously described for the other samples. Similar results were obtained for DS_3h.

Thus, a nanostructural molybdenum oxides rich sample with enhanced surface area was successfully obtained by using a double-step free corrosion process.

3.2. Hydrogen Evolution Reaction studies

Since, Mo oxides have been proven as active electrocatalysts for HER, we tested our samples, SS_HF and DS_1h, for the same.[19,31,48] The ECSA was estimated using the

double layer capacitance method as described earlier in the 'Experimental' section. CV curves can be found below in Figure 12. The obtained ECSA has been used to normalize the current density for each sample.

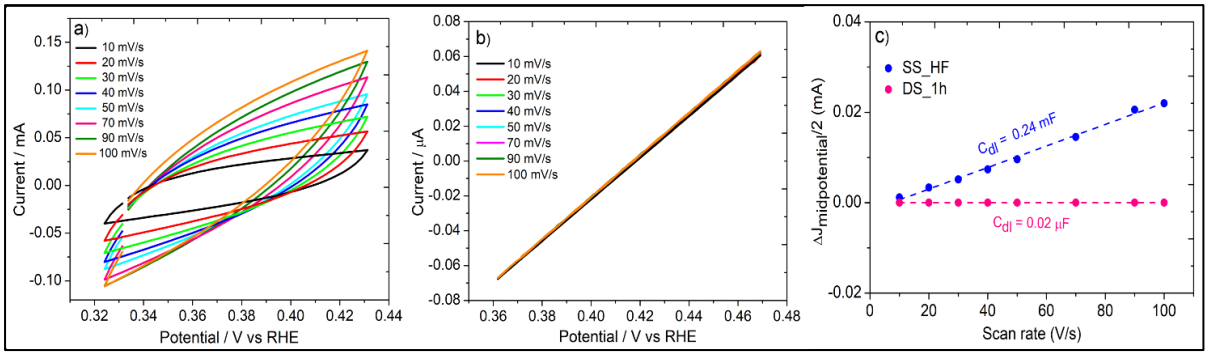

Figure 12. ECSA analysis of SS_HF and DS_1h: CV curves for (**a)** SS_HF, (**b)** DS_1h and (**c)** corresponding dependence of $\Delta J_{midpotential/2}$ and scan rate for SS_HF and DS_1h.

Figure 13 (a) reports LSV polarization curves for pure Pt, SS_HF and DS_1h. The current density involved in the whole range explored is always higher for Pt compared with that of SS_HF and DS_1h. The onset potential, which marks the onset of a large increment in current, comes out as -50 mV for SS_HF and -45 mV for DS_1h. These values top those of some already reported electrocatalysts such as -80 mV for core-shell nanocomposite based on Au nanoparticle@Zn-Fe-embedded porous carbons (Au@Zn-Fe-C) [56]; 198 mV for $CoTe_2$ nanoparticles [57]; -58 mV for N-graphene/Co-embedded porous carbon derived from Metal Organic Frameworks [58]; and 82 mV for hierarchical β-Mo_2C nanotubes.[59]

DS_1h reaches the current density of -10 mA cm^{-2} at an overpotential of -1.24 V. The Tafel plots of the samples and the Pt reference were estimated in the region below the onset potential by linearly fitting data with the Tafel equation,

$$\eta = b \log j + a$$

where η is the overpotential, j is the current density and b is the Tafel slope.[60] Tafel slope is a guide to determine the mechanism and the rate-determining step (r.d.s.) for the HER, based on the classical combination or Tafel reaction and (iii) desorption or Heyrovsky reaction.[61,62] The first step is ruled by the discharged process where a proton and a transferred electron interact, forming an adsorbed hydrogen atom on the electrode surface.[63] Then, the reaction could follow either the Tafel or the Heyrovsky reaction: in the former case, two adsorbed hydrogen atoms combine to evolve H_2, whereas in the second case, an adsorbed hydrogen atom, a proton from the solution and another electron react to generate H_2. The rate-determining step (r.d.s.) of the HER can be evaluated by the examination of the Tafel slope: a slope of 120 mV/dec or higher indicates that the r.d.s. is the Volmer reaction; slopes of 40 mV/dec are found when the r.d.s is the Heyrovsky reaction

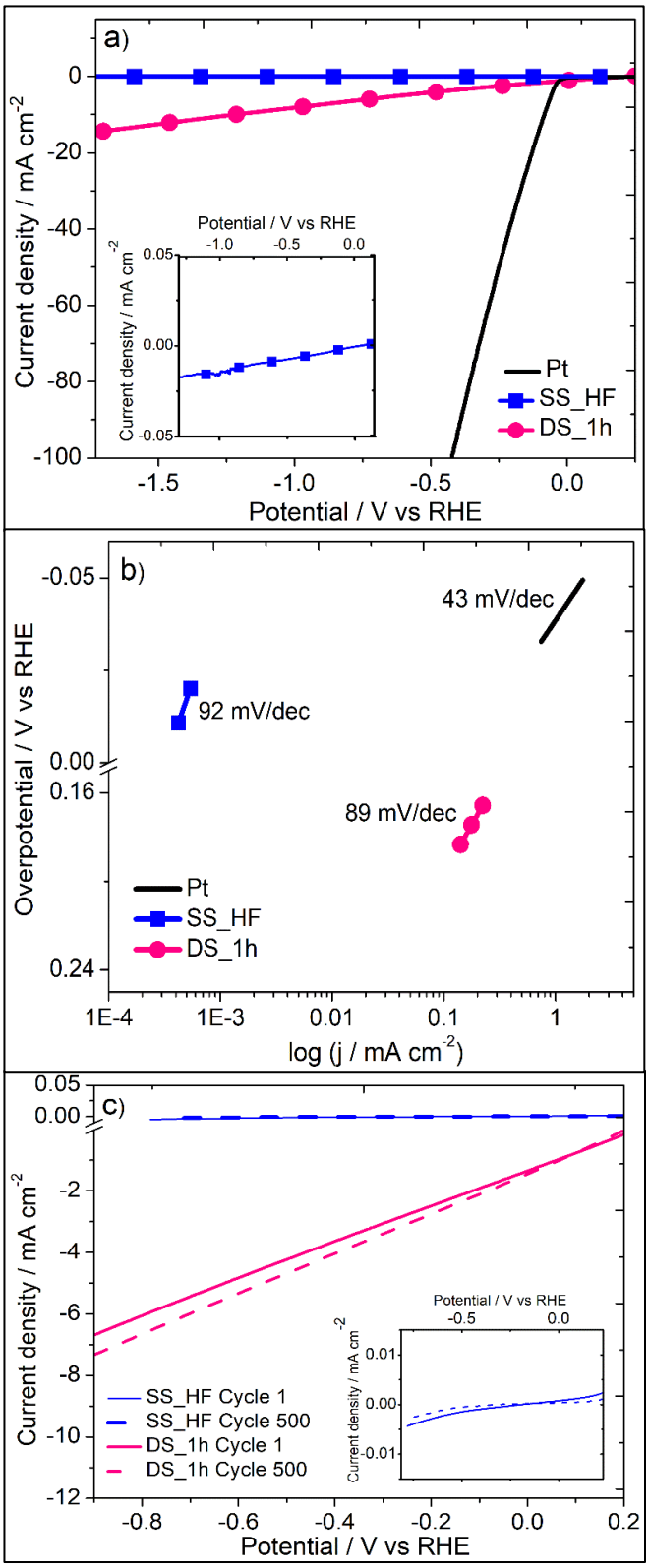

Figure 13. For pure Pt (solid black line), SS_HF (blue line with cubes) and DS_1h (dotted pink line) (**a**) linear sweep voltammetry (LSV) polarisation curves, inset shows the magnified view of the curve for SS_HF; (**b**) Tafel slope; and (**c**) LSV polarization curves after 500 cycles of potential scans for SS_HF and DS_1h, inset shows the magnified view of the curves for SS_HF.

while when the r.d.s. is the Tafel step, slope decreases to a value of 30 mV/dec.[64]

From Figure 13 (b), low Tafel slope values of 92 mV/dec for SS_HF and 89 mV/dec for DS_1h have been obtained signaling that Volmer is the rate-determining step.[64,65] This also suggests that with increasing applied potentials a faster surge in the HER rate will occur for both the samples. To compare with the literature, the Tafel slopes obtained in this work noticeably outdo the value of 130 mV/dec for Au@Zn-Fe-C mentioned previously [56]; 120 mV/dec for Co-doped MoS_2 nanosheets, Co-MoS_2-0.5 [66]; 370 mV/dec and 138 mV/dec for Pd-based nanoalloys assembled on reduced graphene oxide, rGO-$Fe_{48}Pd_{52}$ and rGO-$Au_{48}Pd_{52}$ respectively [67]; 125 mV/dec for Co-MOF, CTGU-5 [68]; 165 mV/dec reported for Au-Pd alloy nanoparticles electrodeposited on microwave assisted sol-gel-derived carbon ceramic electrodes, namely Au-MWCCE [69]; 126 mV/dec for N-graphene/co-embedded porous carbon derived from MOFs [58]; 94 mV/dec for nanostructured core–shell CoS_2@MoS_2/CP [70]; mV/dec for 100 mV/dec for Ni/Mo_2C nanoparticles coated with graphene shells, NiMo_2C@C [71]; 96 mV/dec for Co_9S_8/$CoS_{1.097}$/rGO prepared from Co-MOF [72]; and 116.9 mV/dec for Ni-doped Mo_2C coating on carbon fiber paper, Ni-Mo_2C/CFP [73].

From the intercept of the Tafel plot high values of exchange current densities for SS_HF and DS_1h are determined as 0.08 mA cm^{-2} and 0.35 mA cm^{-2}, respectively. It is known that if the exchange current density is high, the surface of the electrode is more active which means that the charge has to overcome lower energy barrier in moving from electrolyte to the catalyst surface, and vice versa.[74] Accordingly, electrochemical reaction is fast and high current generation takes place at a given overpotential.[74] The obtained exchange current density values surpass a number of those formerly reported in literature such as, 8.32×10^{-9} mA cm^{-2} for the aforementioned Au-MWCCE [69]; 1.92×10^{-3} mA cm^{-2} for N-doped carbon coated Co–Ni alloy with reduced graphene oxide decoration (CoNi@N-C/rGO) [75]; 0.017 mA cm^{-2} for hierarchical β-Mo_2C nanotubes [59]; 9.2×10^{-4} mA cm^{-2} for cocoon-like molybdenum sulfide nanostructures (MoS_2-Mo-1h) [76]; 5.9×10^{-5} mA cm^{-2} for $CoTe_2$ nanoparticles [57]; and 0.017 mA cm^{-2} reported for Pd-modified carbon fibre electrode.[77,78] The value of 0.35 mA cm^{-2} for DS_1h exceeds that of 0.13 mA cm^{-2} for aforementioned rGO-$Au_{48}Pd_{52}$ [67] and 0.126 mA cm^{-2} for nanostructured porous gold film [45]. Figure 13 (c) illustrates the LSV polarization curves of SS_HF and DS_1h after 500 cycles of potential scans showing their efficient durability. Moreover, chronoamperometric measurements were also performed in 0.5 M H_2SO_4 applying a potential of -0.48 V vs. RHE that remains constant during the measurement (Figure 14). The current is found to be generally stable for a period of more than 15 h for both the samples, once again confirming their remarkable stability for HER. The XRD patterns of the samples after the chronoamperometric stability test have been provided in Figure 15, showing no significant differences compared to the XRD patterns obtained before the test as already provided in Figure 2. SEM images were also obtained for the samples after the chronoamperometric stability test (Figure 16) where no changes in the morphology can be noticed. Moreover, EDS analysis was performed and no variations in the composition was detected with respect to the as prepared sample.

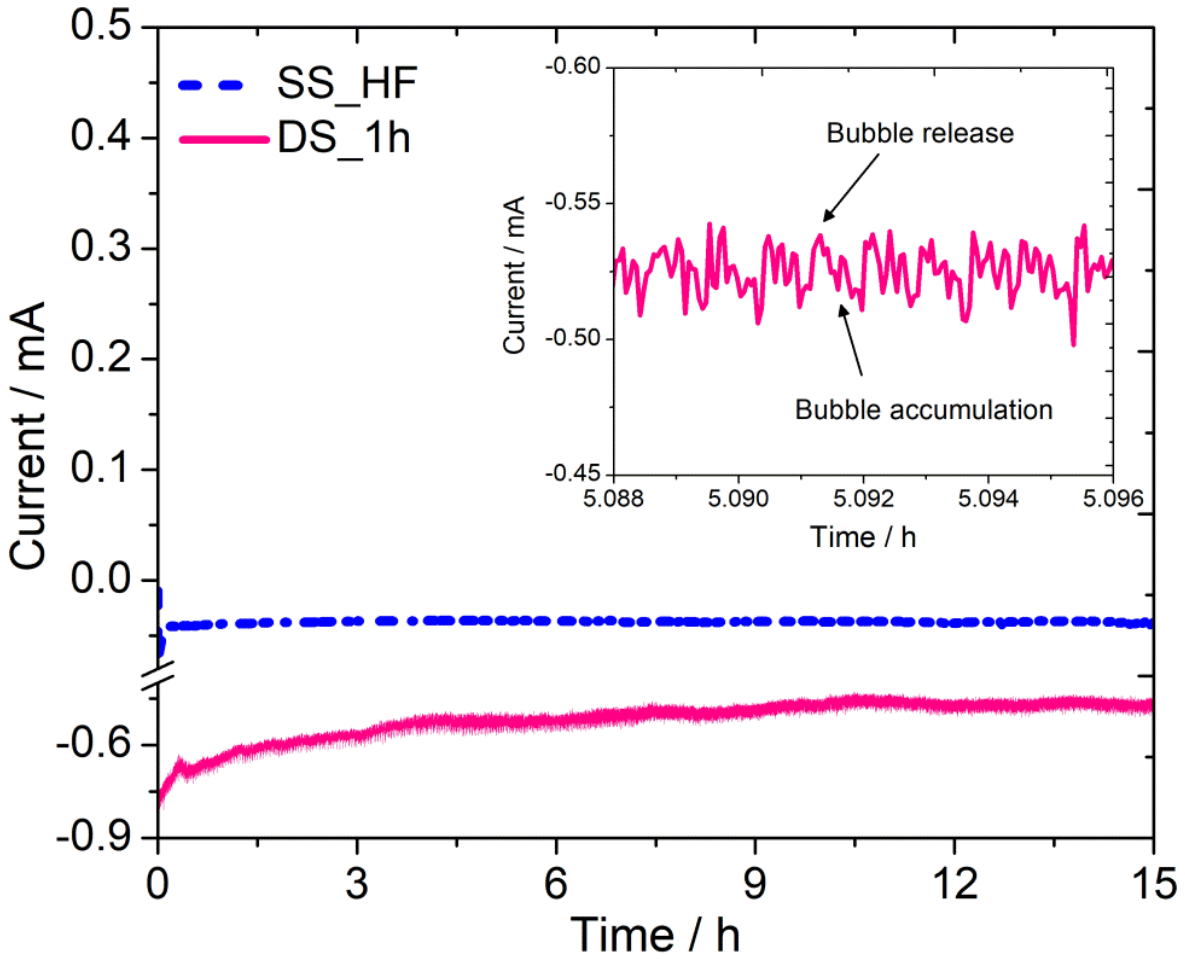

Figure 14. Chronoamperometric measurements for SS_HF and DS_1h in 0.5 M H_2SO_4 at -0.48 V vs RHE.

Active sites for molybdenum oxides are reported in literature to be related to variations in the oxidation states of the material. The possible anion vacancies, which are viewed as the electrochemical active sites, stimulate the HER, favour the electrochemical kinetics and can also significantly increase the electrical conductivity of the electrode.[79–81] A similar behaviour can be inferred for SS_HF and DS_1h samples.

Based on the above results it is clear that DS_1h shows smaller onset potential and Tafel slope than SS_HF. It also gives higher exchange current density than SS_HF. Moreover, only DS_1h is capable of reaching the current density of -10 mA cm^{-2}. These findings can be credited to its nanostructured morphology with larger surface area compared to that of SS_HF which increases the number of active sites enhancing the overall HER activity.

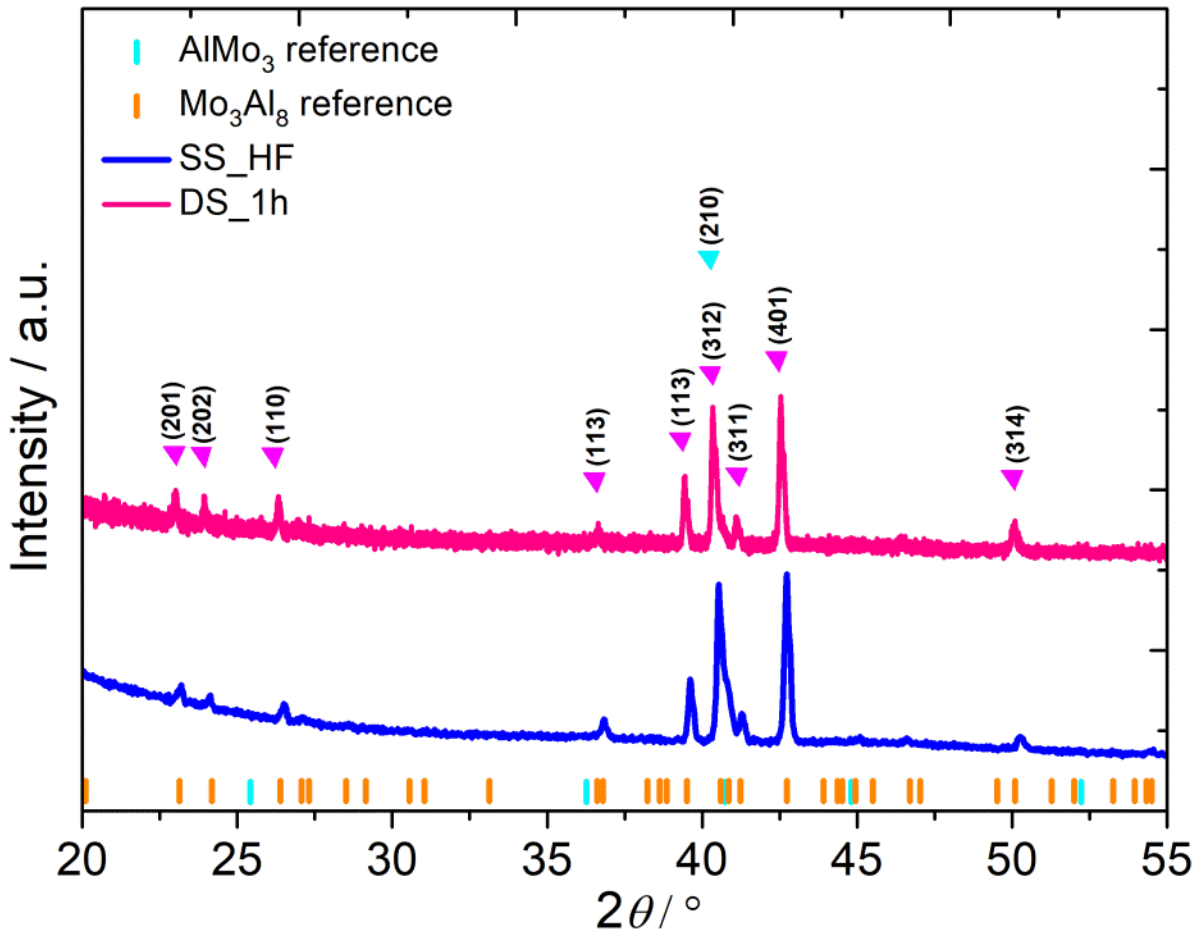

Figure 15. XRD patterns of SS_HF and DS_1h after the chronoamperometric stability test in 0.5 M H_2SO_4 at -0.48 V vs RHE for 15 h.

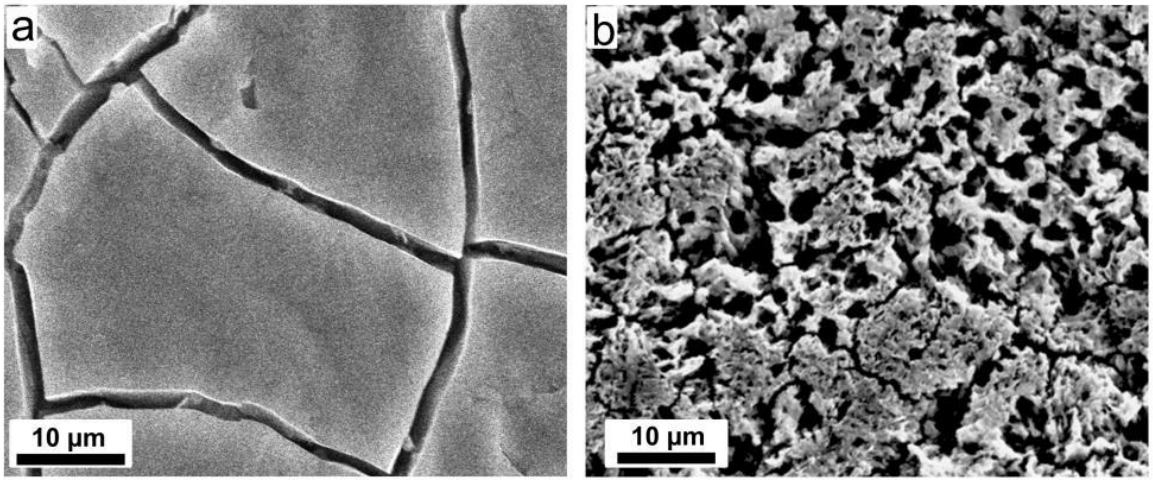

Figure 16. SEM images of SS_HF and DS_1h after the chronoamperometric stability test in 0.5 M H_2SO_4 at -0.48 V vs RHE for 15 h.

4. Conclusions

Nanostructured molybdenum oxides have been obtained using an intermetallic Mo_3Al_8 precursor formed into ribbons by arc melting and melt-spinning techniques. The precursor was subjected to single and double-step free corrosion in 1 M KOH, 1 M HF and 1.25 M $FeCl_3$ at room temperature for varying durations. In the case of single-step free corrosion using KOH, the morphology, characterized by a rough surface with pores, was ascribed to general corrosion as confirmed by the EDS analysis which gave nominal composition on the sample surface and in the bulk. On treating the sample with HF, about 9 µm thick layer of MoO_3 was obtained. However, the layer was compact and the nanostructural morphology could not be achieved. Overall, HF was found to be much more active in removing the Al content from the sample surface and cross-section as compared to KOH in case of single-step free corrosion. When it came to double-step free corrosion, one of the samples, after treatment with $FeCl_3$ for 1 h and HF for 6 h, subsequently exhibited nanostructural morphology on the surface - 3 µm thick layer rich in MoO_3. None of the treatments could fully generate nanostructuration in the cross-section of the samples. However, in terms of both morphology and composition of the as-treated sample, double-step free corrosion proved to be better than the single-step. Two samples, i.e., SS_HF and DS_1h were selected to be tested as electrocatalysts for the HER in 0.5 M H_2SO_4. The measured values for SS_HF and DS_1h respectively are low onset potential of -50 mV and -45 mV; small Tafel slopes 92 mV dec^{-1} and 89 mV dec^{-1} indicating Volmer as the rate-determining step; and high exchange current density of 0.08 mA cm^{-2} and 0.35 mA cm^{-2}. DS_1h is able to reach a current density of -10 mA cm^{-2} at an overpotential of -1.24 V. Both the samples show stability up to 15 h with no significant changes in their properties. As a whole, these are good findings considering the fact that the samples are obtainable via a fast, simple, low-cost and sustainable overall process including the starting material. The samples can be further developed to enhance their electrocatalytic activity in HER.

5. References

[1] C. Zhang, Z. Xie, X. He, P. Liang, Q. Zeng, Z. Zhang, Fabrication and characterization of nanoporous Cu–Sn intermetallics via dealloying of ternary Mg–Cu–Sn alloys, CrystEngComm. 20 (2018) 6900–6908. https://doi.org/10.1039/C8CE01328D.

[2] E.M. Paschalidou, F. Scaglione, A. Gebert, S. Oswald, P. Rizzi, L. Battezzati, Partially and fully de-alloyed glassy ribbons based on Au: Application in methanol electro-oxidation studies, J. Alloys Compd. 667 (2016) 302–309. https://doi.org/10.1016/j.jallcom.2016.01.181.

[3] Y. Xue, F. Scaglione, P. Rizzi, L. Battezzati, P. Denis, H.-J. Fecht, Electrodeposited platinum on de-alloyed nanoporous gold with enhanced electro-catalytic performance, Appl. Surf. Sci. 476 (2019) 412–417. https://doi.org/10.1016/j.apsusc.2019.01.099.

[4] Y. Xue, F. Scaglione, P. Rizzi, L. Battezzati, P. Denis, H.-J. Fecht, Electrodeposited

platinum on de-alloyed nanoporous gold with enhanced electro-catalytic performance, Appl. Surf. Sci. 476 (2019) 412–417. https://doi.org/10.1016/j.apsusc.2019.01.099.

[5] T. Richardson, B. Cottis, D. Scantlebury, R. Lindsay, S. Lyon, M. Graham, Shreir's Corrosion, Elsevier, 2010. https://doi.org/10.1016/C2009-1-28357-2.

[6] V.S. Saji, C.-W. Lee, Molybdenum, Molybdenum Oxides, and their Electrochemistry, ChemSusChem. 5 (2012) 1146–1161. https://doi.org/10.1002/cssc.201100660.

[7] W.A. Badawy, F.M. Al-Kharafi, Corrosion and passivation behaviors of molybdenum in aqueous solutions of different pH, Electrochim. Acta. 44 (1998) 693–702. https://doi.org/10.1016/S0013-4686(98)00180-7.

[8] D. Lützenkirchen-Hecht, R. Frahm, Corrosion of Mo in KOH: Time resolved XAFS investigations, J. Phys. Chem. B. 105 (2001) 9988–9993. https://doi.org/10.1021/jp003414n.

[9] L. De Rosa, C.R. Tomachuk, J. Springer, D.B. Mitton, S. Saiello, F. Bellucci, The wet corrosion of molybdenum thin film - Part I: Behavior at 25°C, Mater. Corros. 55 (2004) 602–609. https://doi.org/10.1002/maco.200303785.

[10] E.I. Stiefel, Molybdenum Compounds, Kirk-Othmer Encycl. Chem. Technol. (2001). https://doi.org/doi:10.1002/0471238961.1315122519200905.a01.pub2.

[11] T. J.A. Richardson, Shreir's Corrosion vol III, Elsevier B.V., 2010, n.d.

[12] Y.X. Li, Q.B. Yang, X.F. Yu, A. Trinchi, A.Z. Sadek, W. Wlodarski, K. Kalantar-zadeh, Nano structured molybdenum oxide gas sensors, Proc. IEEE Sensors. (2006) 232–234. https://doi.org/10.1109/ICSENS.2007.355764.

[13] S. Losse, H. Junge, Recent Progress in Catalysis and Photochemistry for Energy Technologies, ChemSusChem. 3 (2010) 1409–1410. https://doi.org/10.1002/cssc.201000321.

[14] L. Zheng, Y. Xu, D. Jin, Y. Xie, Novel Metastable Hexagonal MoO3 Nanobelts: Synthesis, Photochromic, and Electrochromic Properties, Chem. Mater. 21 (2009) 5681–5690. https://doi.org/10.1021/cm9023887.

[15] Y. Shi, B. Guo, S.A. Corr, Q. Shi, Y.-S. Hu, K.R. Heier, L. Chen, R. Seshadri, G.D. Stucky, Ordered Mesoporous Metallic MoO2 Materials with Highly Reversible Lithium Storage Capacity, Nano Lett. 9 (2009) 4215–4220. https://doi.org/10.1021/nl902423a.

[16] X.R. Shi, J. Wang, K. Hermann, Theoretical cluster studies on the catalytic sulfidation of MoO3, J. Phys. Chem. C. 114 (2010) 6791–6801. https://doi.org/10.1021/jp911639e.

[17] P. Martin-Ramos, I. Fernández-Coppel, M. Avella, J. Martín-Gil, α-MoO3 Crystals with a Multilayer Stack Structure Obtained by Annealing from a Lamellar MoS2/g-C3N4 Nanohybrid, Nanomaterials. 8 (2018) 559. https://doi.org/10.3390/nano8070559.

[18] I.A. de Castro, R.S. Datta, J.Z. Ou, A. Castellanos-Gomez, S. Sriram, T. Daeneke, K. Kalantar-zadeh, Molybdenum Oxides – From Fundamentals to Functionality, Adv.

Mater. 29 (2017) 1701619. https://doi.org/10.1002/adma.201701619.

[19] Y. Zhang, J. Zang, C. Han, S. Jia, P. Tian, H. Gao, Y. Wang, Molybdenum oxide and molybdenum carbide coated carbon black as an electrocatalyst for hydrogen evolution reaction in acidic media, Int. J. Hydrogen Energy. 42 (2017) 26985–26994. https://doi.org/10.1016/j.ijhydene.2017.09.077.

[20] L. Li, T. Zhang, J. Yan, X. Cai, S. (Frank) Liu, P Doped MoO3−x Nanosheets as Efficient and Stable Electrocatalysts for Hydrogen Evolution, Small. 13 (2017) 1700441. https://doi.org/10.1002/smll.201700441.

[21] B.L. Abrams, J.P. Wilcoxon, Nanosize Semiconductors for Photooxidation, Crit. Rev. Solid State Mater. Sci. 30 (2005) 153–182. https://doi.org/10.1080/10408430500200981.

[22] L. Liao, S. Wang, J. Xiao, X. Bian, Y. Zhang, M.D. Scanlon, X. Hu, Y. Tang, B. Liu, H.H. Girault, A nanoporous molybdenum carbide nanowire as an electrocatalyst for hydrogen evolution reaction, Energy Environ. Sci. 7 (2014) 387–392. https://doi.org/10.1039/C3EE42441C.

[23] F.H. Saadi, A.I. Carim, J.M. Velazquez, J.H. Baricuatro, C.C.L. McCrory, M.P. Soriaga, N.S. Lewis, Operando synthesis of macroporous molybdenum diselenide films for electrocatalysis of the hydrogen-evolution reaction, ACS Catal. 4 (2014) 2866–2873. https://doi.org/10.1021/cs500412u.

[24] L. Ma, L.R.L. Ting, V. Molinari, C. Giordano, B.S. Yeo, Efficient hydrogen evolution reaction catalyzed by molybdenum carbide and molybdenum nitride nanocatalysts synthesized via the urea glass route, J. Mater. Chem. A. 3 (2015) 8361–8368. https://doi.org/10.1039/c5ta00139k.

[25] H. Wang, C. Tsai, D. Kong, K. Chan, F. Abild-Pedersen, J.K. Nørskov, Y. Cui, Transition-metal doped edge sites in vertically aligned MoS2 catalysts for enhanced hydrogen evolution, Nano Res. 8 (2015) 566–575. https://doi.org/10.1007/s12274-014-0677-7.

[26] Y. Jiang, Y. He, C.T. Liu, Review of porous intermetallic compounds by reactive synthesis of elemental powders, Intermetallics. 93 (2018) 217–226. https://doi.org/10.1016/j.intermet.2017.06.003.

[27] J.A. Horton, C.T. Liu, M.L. Santella, Microstructures and mechanical properties of Ni3Al alloyed with iron additions, Metall. Trans. A. 18 (1987) 1265–1277. https://doi.org/10.1007/BF02647196.

[28] L.M. Pike, I.M. Anderson, C.T. Liu, Y.A. Chang, Site occupancies, point defect concentrations, and solid solution hardening in B2 (Ni,Fe)Al, Acta Mater. 50 (2002) 3859–3879.

[29] Y.H. He, Y. Jiang, N.P. Xu, J. Zou, B.Y. Huang, C.T. Liu, P.K. Liaw, Fabrication of Ti–Al Micro/ Nanometer-Sized Porous Alloys through the Kirkendall Effect, Adv. Mater. 19 (2007) 2102–2106. https://doi.org/10.1002/adma.200602398.

[30] A. Dasgupta, R.M. Rioux, Intermetallics in catalysis: An exciting subset of multimetallic catalysts, Catal. Today. (2019).

https://doi.org/10.1016/j.cattod.2018.05.048.

[31] R.S. Datta, F. Haque, M. Mohiuddin, B.J. Carey, N. Syed, A. Zavabeti, B. Zhang, H. Khan, K.J. Berean, J.Z. Ou, N. Mahmood, T. Daeneke, K. Kalantar-zadeh, Highly active two dimensional α-MoO 3−x for the electrocatalytic hydrogen evolution reaction, J. Mater. Chem. A. 5 (2017) 24223–24231. https://doi.org/10.1039/C7TA07705J.

[32] M.M. Najafpour, A. Shirazi Amin, S.E. Balaghi, B. Deljoo, Y. Mousazade, T. Jafari, M. Aindow, S.L. Suib, Transformation of La0.65Sr0.35MnO3 in electrochemical water oxidation, Int. J. Hydrogen Energy. 42 (2017) 8560–8568. https://doi.org/10.1016/j.ijhydene.2016.11.016.

[33] F. Scaglione, Y. Xue, F. Celegato, P. Rizzi, L. Battezzati, Amorphous molybdenum sulphide @ nanoporous gold as catalyst for hydrogen evolution reaction in acidic environment, J. Mater. Sci. 53 (2018) 12388–12398. https://doi.org/10.1007/s10853-018-2490-2.

[34] R. Wu, J. Zhang, Y. Shi, D. Liu, B. Zhang, Metallic WO2-Carbon Mesoporous Nanowires as Highly Efficient Electrocatalysts for Hydrogen Evolution Reaction, J. Am. Chem. Soc. 137 (2015) 6983–6986. https://doi.org/10.1021/jacs.5b01330.

[35] J. Zhu, L. Hu, P. Zhao, L.Y.S. Lee, K.-Y. Wong, Recent Advances in Electrocatalytic Hydrogen Evolution Using Nanoparticles, Chem. Rev. 120 (2020) 851–918. https://doi.org/10.1021/acs.chemrev.9b00248.

[36] L.P. Hernández-Saravia, A. Sukeri, M. Bertotti, Fabrication of nanoporous gold-islands via hydrogen bubble template: An efficient electrocatalyst for oxygen reduction and hydrogen evolution reactions, Int. J. Hydrogen Energy. 44 (2019) 15001–15008. https://doi.org/https://doi.org/10.1016/j.ijhydene.2019.04.186.

[37] W. Yan, W. Wu, K. Wang, Z. Tang, S. Chen, Oxygen reduction reaction and hydrogen evolution reaction catalyzed by carbon-supported molybdenum-coated palladium nanocubes, Int. J. Hydrogen Energy. 43 (2018) 17132–17141. https://doi.org/10.1016/j.ijhydene.2018.07.097.

[38] G. Darabdhara, M.R. Das, M.A. Amin, G.A.M. Mersal, N.Y. Mostafa, S.S. Abd El-Rehim, S. Szunerits, R. Boukherroub, Au Ni alloy nanoparticles supported on reduced graphene oxide as highly efficient electrocatalysts for hydrogen evolution and oxygen reduction reactions, Int. J. Hydrogen Energy. 43 (2018) 1424–1438. https://doi.org/10.1016/j.ijhydene.2017.11.048.

[39] M.K. Kundu, T. Bhowmik, S. Barman, Gold aerogel supported on graphitic carbon nitride: an efficient electrocatalyst for oxygen reduction reaction and hydrogen evolution reaction, J. Mater. Chem. A. 3 (2015) 23120–23135. https://doi.org/10.1039/C5TA06740E.

[40] D. Yan, S. Dou, L. Tao, Z. Liu, Z. Liu, J. Huo, S. Wang, Electropolymerized supermolecule derived N, P co-doped carbon nanofiber networks as a highly efficient metal-free electrocatalyst for the hydrogen evolution reaction, J. Mater. Chem. A. 4 (2016) 13726–13730. https://doi.org/10.1039/C6TA05863A.

[41] X. Fan, Z. Peng, R. Ye, H. Zhou, X. Guo, M3C (M: Fe, Co, Ni) Nanocrystals Encased

in Graphene Nanoribbons: An Active and Stable Bifunctional Electrocatalyst for Oxygen Reduction and Hydrogen Evolution Reactions, ACS Nano. 9 (2015) 7407–7418. https://doi.org/10.1021/acsnano.5b02420.

[42] J. Tian, W. Wu, Z. Tang, Y. Wu, R. Burns, B. Tichnell, Z. Liu, S. Chen, Oxygen Reduction Reaction and Hydrogen Evolution Reaction Catalyzed by Pd–Ru Nanoparticles Encapsulated in Porous Carbon Nanosheets, Catalysts. 8 (2018) 329. https://doi.org/10.3390/catal8080329.

[43] H. Yang, Y. Zhang, F. Hu, Q. Wang, Urchin-like CoP Nanocrystals as Hydrogen Evolution Reaction and Oxygen Reduction Reaction Dual-Electrocatalyst with Superior Stability, Nano Lett. 15 (2015) 7616–7620. https://doi.org/10.1021/acs.nanolett.5b03446.

[44] X. Ren, F. Yang, R. Chen, P. Ren, Y. Wang, Improvement of HER activity for MoS2: insight into the effect and mechanism of phosphorus post-doping, New J. Chem. 44 (2020) 1493–1499. https://doi.org/10.1039/C9NJ05229A.

[45] A. Sukeri, M. Bertotti, Nanoporous gold surface: An efficient platform for hydrogen evolution reaction at very low overpotential, J. Braz. Chem. Soc. 29 (2018) 226–231. https://doi.org/10.21577/0103-5053.20170132.

[46] Y. Mie, H. Takayama, Y. Hirano, Facile control of surface crystallographic orientation of anodized nanoporous gold catalyst and its application for highly efficient hydrogen evolution reaction, J. Catal. 389 (2020) 476–482. https://doi.org/10.1016/j.jcat.2020.06.023.

[47] C. Tang, H. Zhang, K. Xu, Q. Zhang, J. Liu, C. He, L. Fan, T. Asefa, Unconventional molybdenum carbide phases with high electrocatalytic activity for hydrogen evolution reaction, J. Mater. Chem. A. (2019). https://doi.org/10.1039/c9ta04374h.

[48] Y. Jin, H. Wang, J. Li, X. Yue, Y. Han, P.K. Shen, Y. Cui, Porous MoO 2 Nanosheets as Non-noble Bifunctional Electrocatalysts for Overall Water Splitting, Adv. Mater. 28 (2016) 3785–3790. https://doi.org/10.1002/adma.201506314.

[49] T.F. Jaramillo, K.P. Jørgensen, J. Bonde, J.H. Nielsen, S. Horch, I. Chorkendorff, Identification of Active Edge Sites for Electrochemical H₂ Evolution from MoS₂ Nanocatalysts, Science (80-.). 317 (2007) 100 LP – 102. https://doi.org/10.1126/science.1141483.

[50] Z. He, Y. Huang, F. He, Preparation of nanoporous molybdenum film by dealloying an immiscible Mo–Zn system for hydrogen evolution reaction, RSC Adv. 6 (2016) 15390–15393. https://doi.org/10.1039/C5RA24426A.

[51] M. Lukaszewski, M. Soszko, A. Czerwiński, Electrochemical methods of real surface area determination of noble metal electrodes - an overview, Int. J. Electrochem. Sci. 11 (2016) 4442–4469. https://doi.org/10.20964/2016.06.71.

[52] Y. Qiu, Z. Wen, C. Jiang, X. Wu, R. Si, J. Bao, Q. Zhang, L. Gu, J. Tang, X. Guo, Rational Design of Atomic Layers of Pt Anchored on Mo 2 C Nanorods for Efficient Hydrogen Evolution over a Wide pH Range, Small. (2019). https://doi.org/10.1002/smll.201900014.

[53] A. Hovestad, P.M.M.C. Bressers, R.M. Meertens, C.H. Frijters, W.P. Voorthuijzen, Electrochemical etching of molybdenum for shunt removal in thin film solar cells, J. Appl. Electrochem. 45 (2015) 745–753. https://doi.org/10.1007/s10800-015-0829-9.

[54] E. Lange, M. Pourbaix: Atlas D'Équilibres Électrochimiques à 25 °C. Unter Mitwirkung zahlreicher Fachgelehrter. Mit vielen Figuren und Tabellen. 644 Seiten, 28×22 cm, Ganzleinen. Verlag Gauthier-Villard & Cie, Paris. Preis: 140 Frs., Berichte Der Bunsengesellschaft Für Phys. Chemie. (1963). https://doi.org/10.1002/bbpc.19630670824.

[55] O. Çakir, Chemical etching of aluminium, J. Mater. Process. Technol. 199 (2008) 337–340. https://doi.org/10.1016/j.jmatprotec.2007.08.012.

[56] J. Lu, W. Zhou, L. Wang, J. Jia, Y. Ke, L. Yang, K. Zhou, X. Liu, Z. Tang, L. Li, S. Chen, Core–Shell Nanocomposites Based on Gold Nanoparticle@Zinc–Iron-Embedded Porous Carbons Derived from Metal–Organic Frameworks as Efficient Dual Catalysts for Oxygen Reduction and Hydrogen Evolution Reactions, ACS Catal. 6 (2016) 1045–1053. https://doi.org/10.1021/acscatal.5b02302.

[57] T.-H. Lu, C.-J. Chen, M. Basu, C.-G. Ma, R.-S. Liu, The CoTe 2 nanostructure: an efficient and robust catalyst for hydrogen evolution, Chem. Commun. 51 (2015) 17012–17015. https://doi.org/10.1039/C5CC06806A.

[58] Y. Hou, Z. Wen, S. Cui, S. Ci, S. Mao, J. Chen, Hybrid Electrocatalysis: An Advanced Nitrogen-Doped Graphene/Cobalt-Embedded Porous Carbon Polyhedron Hybrid for Efficient Catalysis of Oxygen Reduction and Water Splitting (Adv. Funct. Mater. 6/2015), Adv. Funct. Mater. 25 (2015) 871–871. https://doi.org/10.1002/adfm.201570041.

[59] F.-X. Ma, H. Bin Wu, B.Y. Xia, C.-Y. Xu, X.W.D. Lou, Hierarchical β-Mo 2 C Nanotubes Organized by Ultrathin Nanosheets as a Highly Efficient Electrocatalyst for Hydrogen Production, Angew. Chemie Int. Ed. 54 (2015) 15395–15399. https://doi.org/10.1002/anie.201508715.

[60] W. Schmickler, J. O'M. Bockris, Shahed U.M. Khan: Surface electrochemistry, a molecular level approach. Plenum Press, New York, London, 1993. ISBN 0-306-44298-1, 1014 Seiten, Preis: $79.50, Berichte Der Bunsengesellschaft Für Phys. Chemie. 98 (1994) 1207–1207. https://doi.org/10.1002/bbpc.19940980933.

[61] X. Yang, W. Xu, S. Cao, S. Zhu, Y. Liang, Z. Cui, X. Yang, Z. Li, S. Wu, A. Inoue, L. Chen, An amorphous nanoporous PdCuNi-S hybrid electrocatalyst for highly efficient hydrogen production, Appl. Catal. B Environ. 246 (2019) 156–165. https://doi.org/https://doi.org/10.1016/j.apcatb.2019.01.030.

[62] M. Gong, W. Zhou, M.-C. Tsai, J. Zhou, M. Guan, M.-C. Lin, B. Zhang, Y. Hu, D.-Y. Wang, J. Yang, S.J. Pennycook, B.-J. Hwang, H. Dai, Nanoscale nickel oxide/nickel heterostructures for active hydrogen evolution electrocatalysis, Nat. Commun. 5 (2014) 4695. https://doi.org/10.1038/ncomms5695.

[63] A.P. Murthy, J. Theerthagiri, J. Madhavan, Insights on Tafel Constant in the Analysis of Hydrogen Evolution Reaction, J. Phys. Chem. C. (2018). https://doi.org/10.1021/acs.jpcc.8b07763.

[64] Q. Tang, D. Jiang, Mechanism of Hydrogen Evolution Reaction on 1T-MoS2 from First Principles, ACS Catal. 6 (2016) 4953–4961. https://doi.org/10.1021/acscatal.6b01211.

[65] B.E. Conway, B. V Tilak, Interfacial processes involving electrocatalytic evolution and oxidation of H2, and the role of chemisorbed H, Electrochim. Acta. 47 (2002) 3571–3594. https://doi.org/https://doi.org/10.1016/S0013-4686(02)00329-8.

[66] Q. Xiong, X. Zhang, H. Wang, G. Liu, G. Wang, H. Zhang, H. Zhao, One-step synthesis of cobalt-doped MoS2 nanosheets as bifunctional electrocatalysts for overall water splitting under both acidic and alkaline conditions, Chem. Commun. 54 (2018) 3859–3862. https://doi.org/10.1039/C8CC00766G.

[67] J.A.S.B. Cardoso, L. Amaral, Ö. Metin, D.S.P. Cardoso, M. Sevim, T. Sener, C.A.C. Sequeira, D.M.F. Santos, Reduced graphene oxide assembled Pd-based nanoalloys for hydrogen evolution reaction, Int. J. Hydrogen Energy. 42 (2017) 3916–3925. https://doi.org/10.1016/j.ijhydene.2016.11.100.

[68] Y.P. Wu, W. Zhou, J. Zhao, W.W. Dong, Y.Q. Lan, D.S. Li, C. Sun, X. Bu, Surfactant-Assisted Phase-Selective Synthesis of New Cobalt MOFs and Their Efficient Electrocatalytic Hydrogen Evolution Reaction, Angew. Chemie - Int. Ed. (2017). https://doi.org/10.1002/anie.201707238.

[69] A. Abbaspour, F. Norouz-Sarvestani, High electrocatalytic effect of Au-Pd alloy nanoparticles electrodeposited on microwave assisted sol-gel-derived carbon ceramic electrode for hydrogen evolution reaction, Int. J. Hydrogen Energy. 38 (2013) 1883–1891. https://doi.org/10.1016/j.ijhydene.2012.11.096.

[70] S. Li, S. Sirisomboonchai, X. An, X. Ma, P. Li, L. Ling, X. Hao, A. Abudula, G. Guan, Engineering interfacial structures to accelerate hydrogen evolution efficiency of MoS2 over a wide pH range, Nanoscale. (2020). https://doi.org/10.1039/d0nr00008f.

[71] X. Li, L. Yang, T. Su, X. Wang, C. Sun, Z. Su, Graphene-coated hybrid electrocatalysts derived from bimetallic metal-organic frameworks for efficient hydrogen generation, J. Mater. Chem. A. (2017). https://doi.org/10.1039/c6ta10405c.

[72] X. Sun, H. Huang, C. Wang, Y. Liu, T.L. Hu, X.H. Bu, Effective CoxSy Hydrogen Evolution Reaction Electrocatalysts Fabricated by In Situ Sulfuration of a Metal–Organic Framework, ChemElectroChem. (2018). https://doi.org/10.1002/celc.201801493.

[73] Z. Hu, J. Huang, Y. Luo, M. Liu, X. Li, M. Yan, Z. Ye, Z. Chen, Z. Feng, S. Huang, Wrinkled Ni-doped Mo2C coating on carbon fiber paper: An advanced electrocatalyst prepared by molten-salt method for hydrogen evolution reaction, Electrochim. Acta. (2019). https://doi.org/10.1016/j.electacta.2019.06.178.

[74] F. Barbir, Chapter Three - Fuel Cell Electrochemistry, 2013.

[75] L. Chen, S. Yang, K. Qian, W. Wei, C. Sun, J. Xie, In situ growth of N-doped carbon coated CoNi alloy with graphene decoration for enhanced HER performance, J. Energy Chem. 29 (2019) 129–135. https://doi.org/10.1016/j.jechem.2018.03.005.

[76] W. Li, X. Wang, D. Xiong, L. Liu, Efficient and durable electrochemical hydrogen

evolution using cocoon-like MoS2 with preferentially exposed edges, Int. J. Hydrogen Energy. 41 (2016) 9344–9354. https://doi.org/10.1016/j.ijhydene.2016.03.209.

[77] B. Pierozynski, Hydrogen evolution reaction at Pd-modified carbon fibre and nickel-coated carbon fibre materials, Int. J. Hydrogen Energy. 38 (2013) 7733–7740. https://doi.org/10.1016/j.ijhydene.2013.04.092.

[78] B. Pierozynski, T. Mikolajczyk, M. Turemko, E. Czerwosz, M. Kozlowski, Hydrogen evolution reaction at Pd-modified carbon fibre in 0.1 M NaOH, Int. J. Hydrogen Energy. 40 (2015) 1795–1799. https://doi.org/10.1016/j.ijhydene.2014.12.029.

[79] M. Wu, S. Ke, W. Chen, S. Zhang, M. Zhu, Y. Zhang, M.L. Foo, L. Tang, Optimization of the facet structure of cobalt oxide catalysts for enhanced hydrogen evolution reaction, Catal. Sci. Technol. (2020). https://doi.org/10.1039/c9cy01900f.

[80] A.K. Nayak, M. Verma, Y. Sohn, P.A. Deshpande, D. Pradhan, Highly active tungsten oxide nanoplate electrocatalysts for the hydrogen evolution reaction in acidic and near neutral electrolytes, ACS Omega. (2017). https://doi.org/10.1021/acsomega.7b01151.

[81] R. Kashfi-Sadabad, S. Yazdani, T.D. Huan, Z. Cai, M.T. Pettes, Role of Oxygen Vacancy Defects in the Electrocatalytic Activity of Substoichiometric Molybdenum Oxide, J. Phys. Chem. C. (2018). https://doi.org/10.1021/acs.jpcc.8b03536.

Chapter IV

NANOPOROUS GOLD

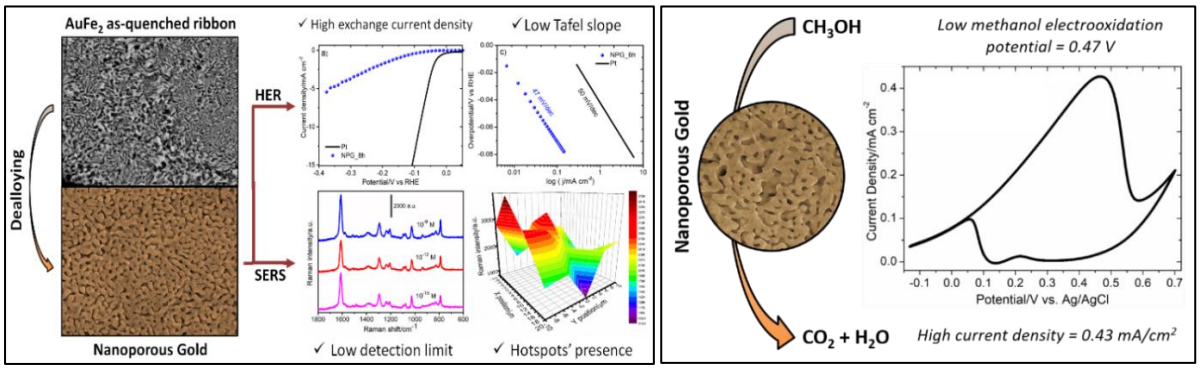

2. Introduction

Nanoporous (NP) metals have been well-renowned as tremendously favourable class of materials employed extensively in wide array of fields such as fuel cells, sensors, catalysis, hydrogen storage, molecular sieves, etc. [1] The credit goes to their unique physical and chemical properties such as bicontinuous porous morphology, high surface area-to-volume ratio, high thermal conductivity, high electrical conductivity, corrosion resistance and fatigue resistance.[2,3] NP metals are made of a three dimensional scaffold of bi-continuous ligament-pore framework based on an almost pure metal. [1,2,4–7] Their properties have been found to be strongly dependent on the characteristic length of porosity, namely the nano-pore and ligament sizes.[8–11] Nanoporous gold (NPG) is one such promising NP metal with a number of applications such as in electrocatalysis, SERS, as sensors etc. [12–15] Its high and tunable porosity, large specific surface area, good structural stability, innumerable active sites, high conductivity and facile preparation and bio-compatibility are some of its highlighting properties which make it quite a worthy candidate in a number of applications such as catalysis, sensing, materials for energy conversion to bio-related applications etc.[13,16]

In this study, the choice of metal to be alloyed with Au was largely dependent on: (i) mechanical strength; (ii) cheap and abundant availability; and (iii) the ease of selective dissolution using common electrolytes in simple experimental conditions. The master alloy was consciously and carefully prepared of an Fe-rich composition with the target of diminishing the amount of expensive Au as low as possible abiding by the parting limit. In accordance with the Au-Fe equilibrium phase diagram, the composition was set at 33 at. % Au and 67 at. % Fe. A careful look at the phase diagram clearly displays an extended miscibility gap of these metals in the solid state [17] due to the structural dissimilarity at room temperature of the body-centred cubic (bcc) Fe and face-centred cubic (fcc) Au and the

large difference in their lattice parameters [18]. Fe and Au are immiscible with very limited solubility at room temperature where only two phases are possible - either bcc phase rich in Fe or fcc phase rich in Au.[19] There is absence of any intermetallic compound. At room temperature metastable supersaturated solid solutions can be obtained using the rapid solidification technique which acts as a precursor alloy for the fabrication of NPG. [17] [19,20]

A technique which has gained substantial fascination as a straight-forward technique for tailoring NP metals is dealloying. It is a phenomenon of controlled etching where the less noble metal is selectively removed from an alloy.[21] During this process, accompanying the dissolution of the less noble elements, remnant more noble metal self-assemble into interconnected ligaments and open pores with random spatial arrangement by surface diffusion. [3,21] Dealloying can be used for both amorphous and crystalline alloy precursors – be it a binary or ternary system or metallic glasses. [4,22] The morphology of the obtained NP metal depends on the state of the chosen alloy precursor.[23,24] In case of dealloying a crystalline alloy, the parent microstructure is retained and a porous single crystal is evolved from each grain[9], contrary to the case of amorphous precursors in which ligaments result from the impingement of numerous fine crystals.[6,7,23] There are several types of dealloying, most common being chemical and electrochemical dealloying. The parting limit is the one of the most important parameters governing the process of chemical dealloying that needs to be carefully obeyed. It is defined as the minimum concentration of a more noble component in the alloy above which parting does not occur.[4,21] In case of electrochemical dealloying, other factors come into play that govern the outcome. They are - (i) a substantial difference in the electrochemical potential between the alloy components and (ii) a critical potential at which dealloying occurs. Careful selection of the etching electrolyte is important in both the types of dealloying which is facilitated by interpreting Pourbaix diagrams for electrochemical techniques. The dealloying method is remarkable in the way that it provides the scope of designing, tuning and producing suitable microstructures and morphologies by varying the experimental conditions, i.e., type and pH of electrolyte, dealloying time and temperature [3, 6, 14]. This means that the NP metal obtained by dealloying can be customized for specific uses in terms of pore and ligament's size and shape [25]. The dealloying of Au-based alloys to obtain NPG is quite feasible and has been studied extensively in a number of works [12,26].

Surface-Enhanced Raman Scattering (SERS) is a notable technique for trace-level molecular detection in biological and chemical systems owing to its high molecular sensitivity and specificity [14,27]. A combined effect of chemical [28] and electromagnetic enhancements [29] has been recognized as the cause of the strong SERS amplification. Species chemisorbed to the surface form a charge-transfer complex which generates the chemical effect [30] while the resonant coupling between the incident laser light and localized surface plasmons in the vicinity of the metallic substrate surface give rise to the electromagnetic effect [30,31] at nanopores, sharp edges and tips called "hot spots" [32,33]. Numerous evidences have been reported regarding successful utilization of NPG as a SERS substrate since they offer countless active sites augmenting the excitations of localized surface plasmons [5,33–35].

Thus, one of the produced NPG samples obtained from a simple synthetic procedure has been tested as a highly active, stable and low-cost alternative for SERS applications.

The incessant global energy needs have compelled the development of renewable, sustainable and efficient alternatives to fossil fuel resources. [36,37] In this regard, Direct methanol fuel cells (DMFCs) have garnered exploding intrigue over the past years towards production of sustainable energy. [38,39] They are electrochemical devices which convert the chemical energy of methanol in electric energy via methanol electro-oxidation. [11] Methanol being a liquid under ambient conditions in addition to its high specific energy, easy storage, low toxicity, lower cost, near room working temperature and abundant production makes for a brilliant energy source.[39–41] The methanol electro-oxidation reaction can be categorized into acidic and alkaline depending on the pH of the supporting electrolyte.[38] The methanol electro-oxidation reaction is the most integral part of DMFCs that takes place at the anode side of a DMFC. [39] The conventional electrocatalysts include Pt-based like Pt−Cu and Pt−Ru alloys. [39,42] But Pt certainly has its disadvantages, for instance, expensiveness, instability and susceptibility to poisoning. [40,43] Developing a sustainable electrocatalyst with low cost, enhanced activity and high durability, thus, becomes crucial. [40] In this thread, NPG stands out as the cheaper alternative supported by its nobility, resistance to surface oxidation and large surface area to volume ratio.[39]

In this chapter, NPG has been fabricated from a metastable supersaturated solid solution of $Au_{33}Fe_{67}$, acting as a cheap precursor. Chemical dealloying has been accomplished in a number of different experimental conditions concerning electrolytes, duration of the dealloying process and temperature of dealloying. The applications of the as-prepared NPG samples have been examined as electrocatalysts for Hydrogen gas is an excellent source of energy which can be harnessed by the HER, Methanol electrooxidation (MeOH-EOx) and active substrates for SERS credited to their augmented surface area to volume ratio and typically large number of active sites. The samples have displayed excellent results as expected which have been discussed further below. The important factors of affordability and sustainability of the proposed nanoporous metals have also been discussed which make it a competitive candidate among contemporary commercial materials.

2. Experimental

To prepare the $Au_{33}Fe_{67}$ master alloy of target composition 33 at. % Au and 67 at. % Fe, pure elements (99.99 % Au and 99.95 % Fe) were subjected to arc-melting in Ti-gettered Ar atmosphere evacuating and purging the furnace several times. The obtained ingot was rapidly solidified using melt-spinning technique from a silica crucible at a linear speed of 25 m s^{-1} onto a hardened Cu wheel in a closed chamber kept under protective Ar atmosphere. The obtained ribbons were long, continuous and homogeneous having 15 μm thickness and 8 mm width.

Dealloying of the as-quenched $AuFe_2$ ribbon was performed chemically and electro-chemic

ally at 70 °C for different durations ranging from 1 h to 16 h in two electrolytes, i.e., 1 M HNO_3 and 1 M HCl. All electrolytes were prepared from chemical grade reagents and deionized water. Samples were rinsed in deionized water several times, dried in air and stored in a closed and clean box before characterization.

The master alloy, as-quenched ribbon and as-dealloyed samples were observed using Panalytical X-pert X-ray Diffractometer in Bragg–Brentano geometry with monochromatic Cu K radiation for phase determination. The obtained XRD patterns were analysed using the Xpert Highscore software and peak assignments were done utilizing the ICDD database provided by the software. Moreover, Scanning Electron Microscopy (Inspect SEM, FEI), Field-Emission Scanning Electron Microscopy (FIB-FESEM/EBSD/EDS/TOF-SIMS Tescan S9000G microscope) and Energy Dispersive X-ray Spectroscopy (Oxford Ultim-Max 100 connected with the FESEM) were used for morphological and compositional analyses respectively.

The electrocatalytic activity of the obtained NPG towards HER was evaluated at room temperature in 0.5 M H_2SO_4 using the standard three-electrode cell configuration, i.e., saturated Ag/AgCl double-bridge reference electrode, Pt-grid counter-electrode and the NPG sample as the working electrode respectively. Linear Sweep Voltammetry (LSV) was conducted in 0.5 M H_2SO_4 from 0.54 V to -0.39 V vs RHE at 2 mV s^{-1} scan speed. As reference, a pure Pt sheet polished on the surface as per conventional metallography was used in the same experimental conditions. All potentials were reported to the reversible hydrogen electrode (RHE) adding a value of (0.199 + 0.059×pH) V. Electrochemically Active Surface Area (EASA) of the NPG samples was determined by electrochemical oxidation of 0.5 M KOH using Cyclic Voltammetry (CV) at a scan rate of 20 mV s^{-1} from 0.4 V to 1.6 V vs RHE [44,45] (Fig. 8). The area under the reduction peak of the graph collected from the CV reflects the amount of electrochemically active sites, thus giving the EASA [46] which came out to be 6.48 cm^2. The current density was then normalized using the obtained EASA.

To examine the electrocatalytic activity of the as-dealloyed samples towards methanol electrooxidation at room temperature a solution of 0.5 M KOH and 5 M CH_3OH was taken as the electrolyte. The standard three-electrode cell configuration was used as mentioned earlier. Preceding the electrocatalytic measurement the concerned sample was immersed in concentrated HNO_3 (65%) for 15 minutes, then rinsed in de-ionized water for 15 min to remove the acid inside pores completely. This process activates the sample preparing it for the electrocatalytic experiment. [15] Next, the sample underwent 500 cycles of potentiodynamic scans at a sweeping rate of 20 mV/s. To get an estimation of the Electrochemically Active Surface Area (EASA) of the NPG samples, electrochemical oxidation of 0.5 M KOH using Cyclic Voltammetry (CV) was performed at a scan rate of 20 mV s^{-1} from -0.13 V to 0.5 V vs Ag/AgCl. [44,45] The reduction peak of the CV curve was integrated to calculate the area under the graph. This area reveals the amount of electrochemically active sites, hence giving the EASA. [46] This EASA was later used to normalize the obtained current density. All the potentials regarding the MeOH-EOx study have been reported with respect to the Ag/AgCl electrode.

To conduct the SERS measurements a Renishaw inVia Raman Microscope with 785 nm laser line was used with an acquisition time of 20 s, a 50×ULWD objective and 0.05 % power at the sample; the SERS probe molecule was chosen to be 4,4′-bipyridine (bipy) [27]. Firstly, concentrated HNO_3 was used to clean the NPG sample for 5 min, then it was rinsed with de-ionized water for several times. Afterwards, the ethanol solution of 4,4′-bipyridine with concentrations of 10^{-9} M, 10^{-12} M and 10^{-15} M were used to immerse the sample for 20 minutes, which enabled adsorption of the probe molecules on the sample surface. After air-drying, the sample surface was measured. Based on characteristic peak at 1614 cm^{-1} SERS intensity mapping image was collected in a 20x30 μm^2 area with bipyridine concentration of 10^{-12} M. All solutions were prepared from chemical grade reagents and de-ionized water.

Thermodynamic calculations were performed by applying the Calphad method [47] and using the ThermoCalc software v. 2021a [48]. Thermodynamic parameters for the Au-Fe system were taken from the literature [49].

3. Results and discussion

3.1. Microstructures obtained from rapid solidification

Fig. 1 depicts the SEM back-scattered electron images (SEM-BSE) of the cross-section of the as-quenched ribbon for which description it is necessary to distinguish two areas in its cross-section, evident in Fig. 1 (a). At a first glance, the wheel-side area appears to be constituted by a finer microstructure, while a coarser one is observed in the air-side with a quite well-defined line of change of the microstructure in the middle of the ribbon. This is mainly due to the faster quenching rate during solidification that is acting in contact with the wheel with respect to the air-side where the heat extraction from the liquid is less efficient [50]. At a more precise analysis it is possible to see that in the wheel side only a matrix with embedded precipitates can be observed, as displayed in Fig. 1 (b), while in Fig. 1 (c) the air-side is observably composed of dark dendritic grains surrounded by a white matrix with embedded precipitates. In order to have a deeper understanding of the microstructure of the rapidly solidified ribbon, Calphad calculations were done for a better knowledge of the thermodynamics of the Au-Fe system. In Fig. 2 (a) the calculated AuFe phase diagram is reported together with the metastable miscibility gap (green curve) in the fcc phase, originating two composition sets, one Au-rich and the other γ-Fe-rich. Furthermore, the T_0 lines for fcc (red curve) and bcc (blue curve) phases are also reported in the same figure. The T_0 lines are the locus of points (temperatures as a function of composition) where the Gibbs free energy of the liquid and a solid phase are equal [51]. As it can be seen, the T_0 line of fcc phase for the $Au_{33}Fe_{67}$ composition lies at 1183°C, i.e., just 79 °C below the liquidus temperature and slightly higher than the peritectic temperature, so at undercoolings that can be easily achieved with quenching rates of the order of 10^6 K/s, i.e., those obtained during rapid solidification with a melt-spinning apparatus. On the contrary, the T_0 line for the formation of a bcc phase lies at far lower temperatures. Therefore, we can expect that the

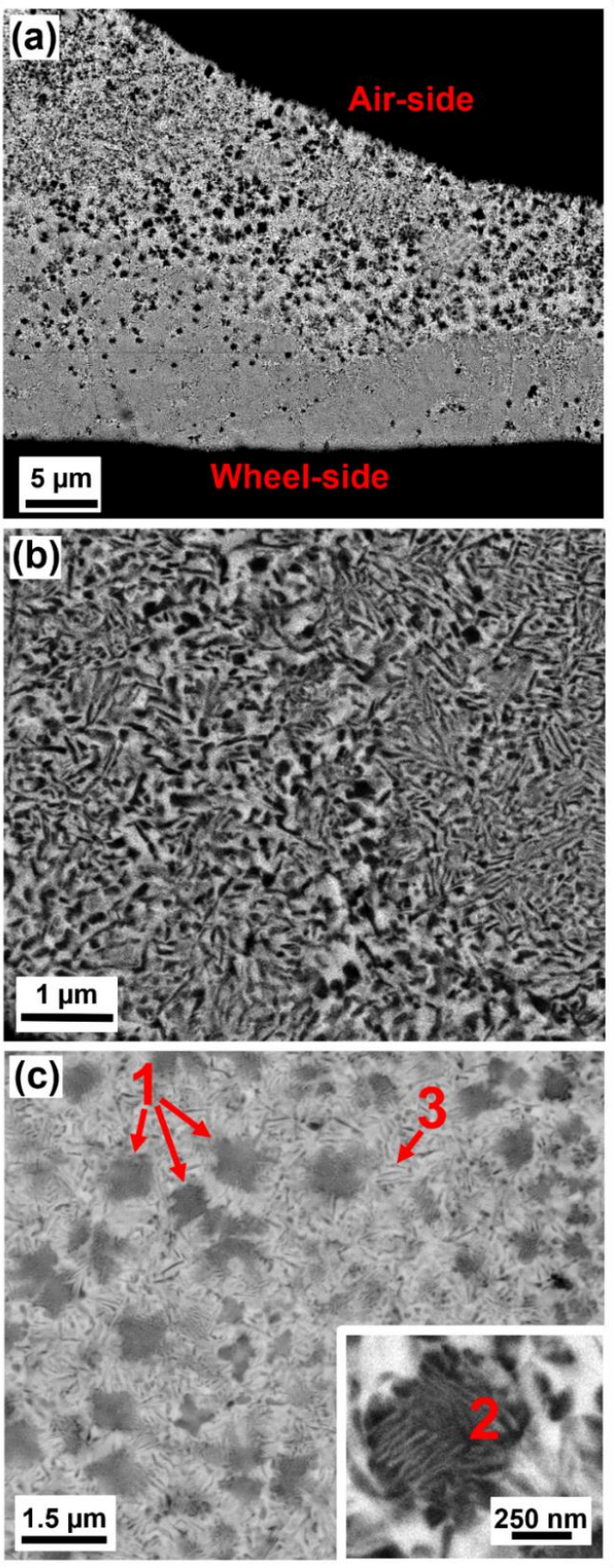

Fig. 1. SEM-BSE image of the as-quenched $Au_{33}Fe_{67}$ ribbon (a) cross-section; (b) wheel side of the cross-section; and (c) air side of the cross-section with the inset showing the magnification of the dendritic region with white lamellas.

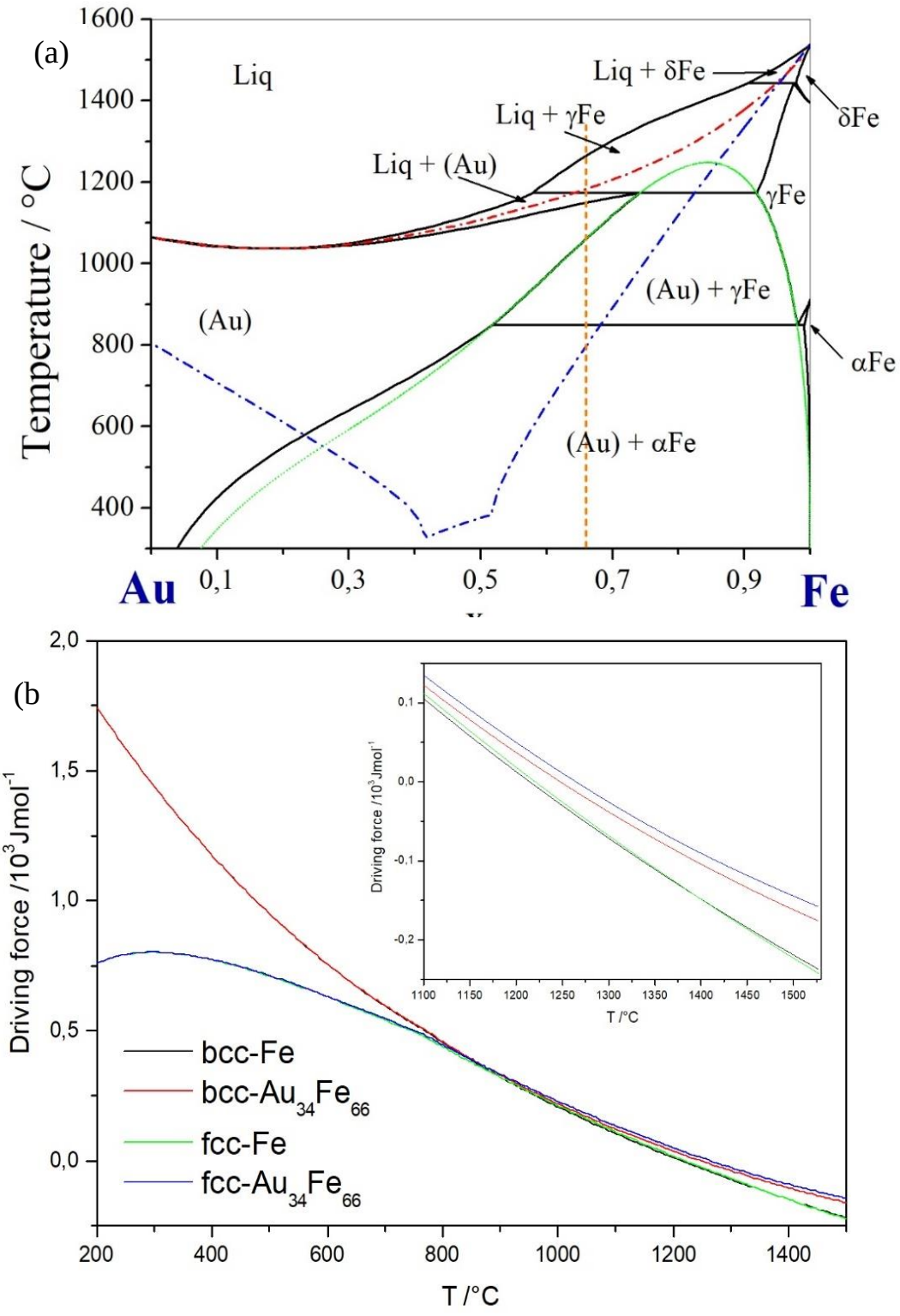

Fig. 2 (a). Au-Fe phase diagram (black curves) calculated using CALPHAD method. Green curve: fcc miscibility gap; T_0 line for the formation of a fcc phase (red curve) and bcc phase (blue curve). In orange is depicted the $Au_{33}Fe_{67}$ composition. (**b).** Driving forces for nucleation of pure Fe and $Au_{33}Fe_{67}$ solid solutions in both fcc and bcc structures from the liquid phase. Inset shows a magnification of the driving force curves for temperatures above 1100 ºC.

liquid phase, reaching the T_0 line on cooling, is partition-less transformed into a fcc solid solution with $Au_{33}Fe_{67}$ composition. This conclusion can be further supported by the calculated driving forces for nucleation of pure Fe in both fcc and bcc structures and $Au_{33}Fe_{67}$ solid solutions in bcc and fcc structures from the liquid phase, as reported in Fig. 2 (b). It is possible to see that at elevated temperatures the fcc solid solution has a slightly greater driving force for nucleation from the liquid with respect to the other phases (inset in Fig. 2 (b)), while at lower temperatures (around 850 °C) the bcc solid solution gains a higher driving force for the formation during solidification.

On this basis, the microstructure of each side of the ribbon can be interpreted as follows:

i) wheel side (Fig. 1 (b)): An fcc (Au) solid solution with $Au_{33}Fe_{67}$ composition is formed directly from the liquid during the solidification with a partition-less solidification. This can be allowed by a significant undercooling of the liquid alloy due to the rapid solidification. T_0 curve lies close to the liquidus line so a limited undercooling is sufficient to allow the partition-less solidification of the liquid with subsequent suppression of the peritectic reaction. During further cooling down, the metastable miscibility gap of the two fcc phases is reached and a consequent precipitation of a γ(Fe) phase can be expected from the fcc (Au) followed by the eutectoid reaction of the latter phase that mainly allows the change in structure of the fcc γ(Fe) into bcc α(Fe) with the formation of a limited amount of fcc (Au) with a eutectoidic microstructure (i.e., alternated lamellas of the two phases). At further cooling, from the fcc (Au) matrix, α(Fe) precipitates are formed (due to the large change in solubility of Fe in Au), while the already formed α(Fe) remains almost unchanged due to the small change in solubility of Au in Fe. So, to summarise, at the end of the solidification process, an fcc (Au) matrix can be observed (white phase in Fig. 1 (b)) with precipitates of bcc α(Fe) of different sizes depending on the temperatures at which they are formed during cooling down (black precipitates in Fig. 1 (b); moreover, alternated lamellas of the two phases must be present but these are difficult to be identified because of the large amount of alternated black and white grains.

ii) air-side (Fig. 1 (c)): The quenching rate is not rapid enough to allow the liquid to reach T_0 line in undercooling, therefore solidification from the liquid of the fcc γ(Fe) primary phase in dendritic shape can be expected. When the peritectic reaction occurs (at peritectic temperature or below) an fcc (Au) phase is formed due to the diffusion of Au atoms, present in the Au-rich liquid, into the fcc γ(Fe) dendrites. The diffusion coefficient of Au in Fe is low [50]. So, we can expect that at the acting solidification rates, the peritectic reaction is incomplete and the core of the former dendrites remains rich in Fe, i.e., fcc γ(Fe), while on the outer part of the pristine dendrites fcc (Au) is formed. When the solidification is completed below the solidus line the microstructure is therefore composed by two phases: i) fcc (Au) (the majority) and fcc γ(Fe) in small amount maintaining the original dendritic shape. During cooling down, the miscibility gap of the two fcc phases is reached so that fcc γ(Fe) precipitates are formed into the fcc (Au) phase. The eutectoid reaction allows the formation of a lamella like microstructure with the formation of alternated grains of bcc α(Fe) and fcc (Au); this microstructure is visible where the darker dendritic regions named 1 in Fig.

1 (c) are present in which white lamellas are visible. In the inset of Fig. 1 (c) a magnification of the dendritic regions is reported in which the eutectoid microstructure is evident (number 2 in inset of Fig. 1 (c)). Cooling down further to room temperature, the formation of bcc α(Fe) precipitates is observed in fcc (Au) visible as darker acicular structures in bright regions (number 3 in Fig. 1 (c)). This is due to the large slope of the solvus line and the large difference in solid solubility of Fe in Au at decreasing temperatures.

EDS analysis confirmed that the desired average composition was obtained, i.e., 33 at. % Au and 67 at. % Fe.

The wheel and air-side of the as-quenched ribbon were both characterized by XRD and no significant preferred orientation was detected in the patterns, while the phases described in the microstructure of the ribbons are confirmed. Fig. 3 (a) shows the XRD pattern of the as-quenched ribbon in which the peaks related to the metastable supersaturated solid solutions fcc (Au) and bcc α(Fe) are present denoted by orange dots and green squares respectively.

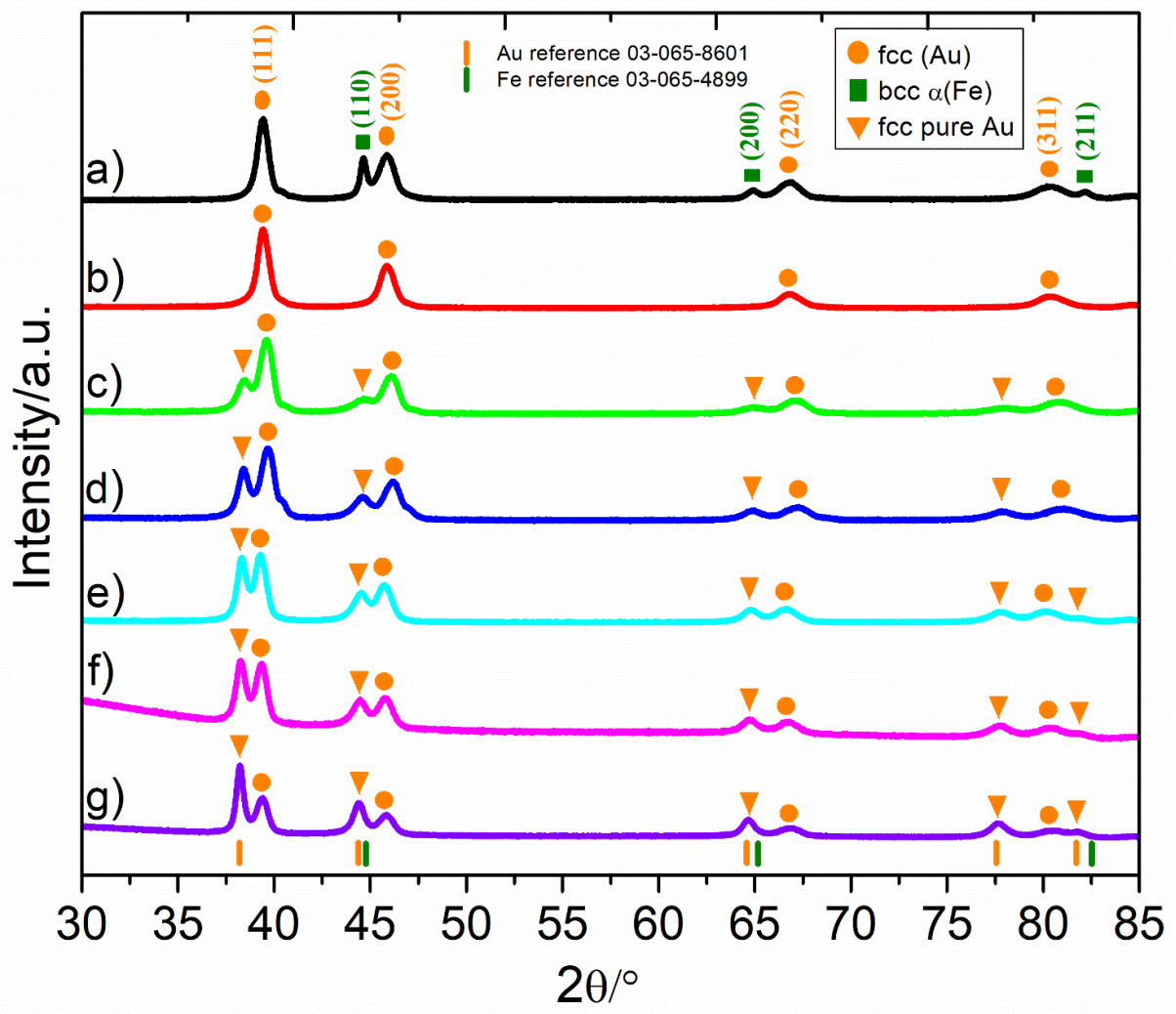

Fig. 3. XRD patterns for (a) the as-quenched ribbon, (b) NPG_1min, (c) NPG_5min, (d) NPG_10min, (e) NPG_30min and (f) NPG_1h and (g) NPG_8h.

The peaks have been assigned according to the ICDD Au reference pattern 03-065-8601 and Fe reference pattern 03-065-4899. It is known that the lattice parameter of solid solutions can change depending on the composition. In this case, fcc (Au) phase has a lower lattice parameter with respect to pure Gold as Fe atoms are incorporated in the Au structure and because of this the peaks in the XRD pattern are shifted towards higher diffraction angles [52]. This shift in the (Au) peaks can be easily noticed in the XRD pattern for the as-quenched ribbon. Similarly, the lattice parameter of the bcc α(Fe) solid solution increases, with respect to pure Fe, to accommodate Au atoms in the Fe lattice resulting in the shift of the Fe characteristic peaks towards smaller diffraction angles. This is corroborated by the lattice parameters of Au and Fe in the as-quenched ribbon calculated as 3.986 nm and 2.942 nm respectively.

3.2. Chemical dealloying

3.2.1. NPG from HNO_3

HNO_3 is a well-known and efficient electrolyte to remove Fe present in the alloy matrix simultaneously having no effect on the Au concentration. Chemical dealloying of the as-quenched ribbon was performed in 1 M HNO_3 at 70 °C for 1 min (NPG_1min), 5 min (NPG_5min), 10 min (NPG_10min), 30 min (NPG_30min), 1 h (NPG_1h), 2 h (NPG_2h), 4 h (NPG_4h), 6 h (NPG_6h) and 8 h (NPG_8h). Fig. 3 compiles the XRD patterns of the different as-prepared samples while Fig. 4 shows the SEM secondary electron (SEM-SE) and back-scattered electron (BSE) images of NPG_1min. In Fig. 3 (b), i.e., the XRD pattern for NPG_1min, it can be seen that after dealloying for 1 min the peaks of bcc α(Fe) phase have disappeared from the pattern signifying the removal of the less noble phase from the alloy microstructure due to a galvanic effect. Only the fcc (Au) phase present in the as-quenched ribbon is visible here that seems to be unaffected. This is also reflected in the SEM -SE image of NPG_1min in Fig. 4 (a) where the dendrites are noticeable as partially empty. Fig. 4 (b) displays the SEM-BSE image for the same sample highlighting this effect. Zooming in at these dendritic shapes, Fig. 4 (c) and Fig. 4 (d) give another glimpse at the dealloying effect on both the phases of the as-quenched ribbon. The dendritic shapes in the as-quenched ribbon consist, as previously described, of two phases: bcc α(Fe) and fcc (Au). After dealloying, tightly-knit network of remnant fcc (Au) phase is observable while the bcc α(Fe) has been eliminated as mentioned before. The SEM-SE and BSE images in Fig. 4 (e) and (f) enable to have a clear and closer look at the fcc (Au) lamellae present within the dendrites. When the time of dealloying is increased to 5 min, for NPG_5min we can observe in Fig. 3 (c) the emerging peaks of a new phase (marked by the orange triangles) with lattice parameter and structure being close to that of pure Au. This signals towards removal of Fe from the fcc (Au) solid solution with a proper dealloying mechanism probably starting when the bcc α(Fe) phase is completely dissolved into the electrolyte. It also indicates the inception of the formation of Au-rich ligaments by surface diffusion of the Au adatoms on the surface of the pristine fcc (Au) solid solution. This pristine phase, which is marked by the orange dots in the

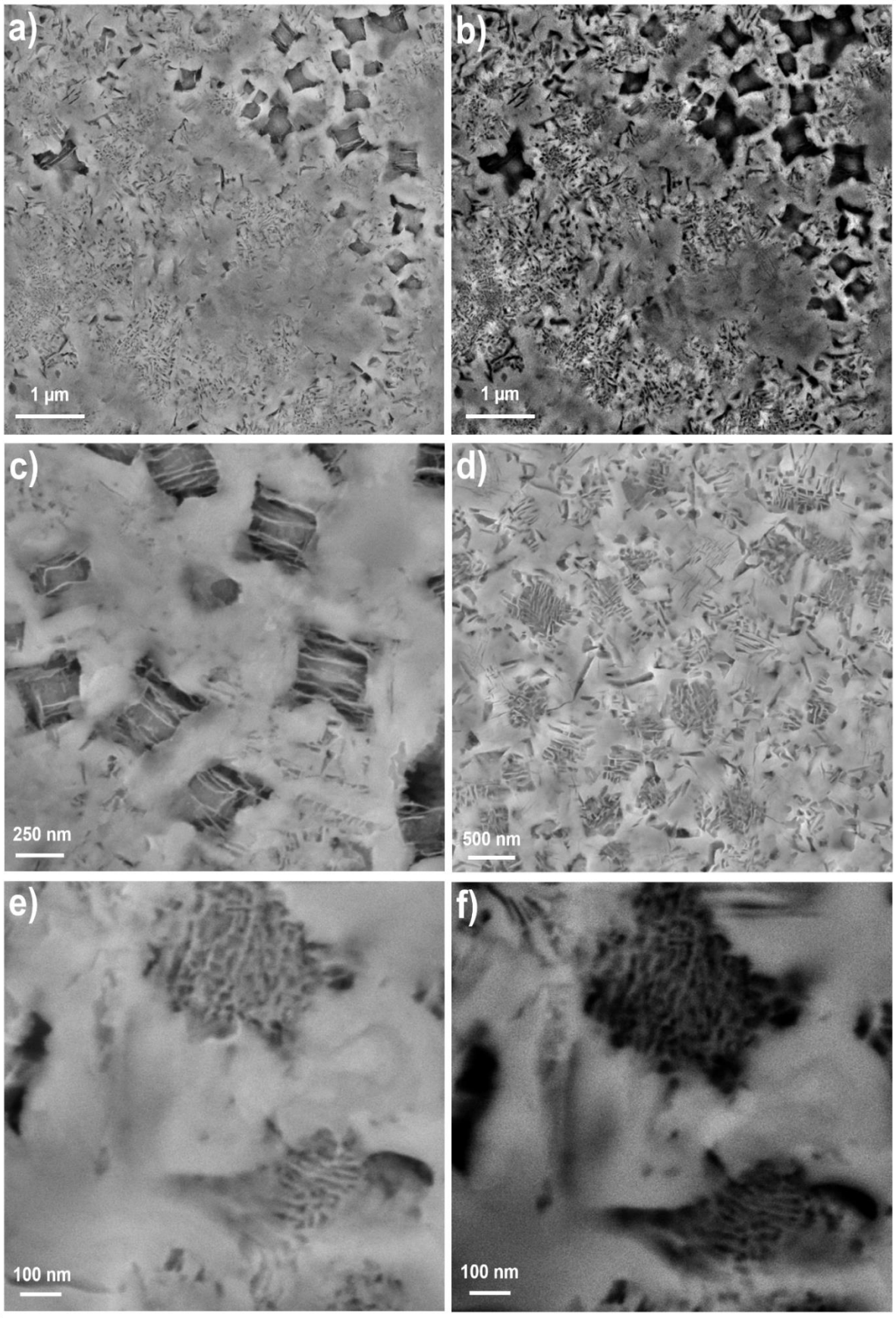

Fig. 4. SEM-SE images of NPG_1min (a, c, d, e) and SEM-BSE images of NPG_1min (b, f).

same pattern, is still remaining underneath not yet dealloyed. The intensity of the peaks of the new phase is much smaller compared to that of the pristine phase which relates to the small volume of precursor that is undergoing the dealloying process at this stage with the formation of a limited number of ligaments, given the short duration of dealloying. Similar observation is made for NPG_10min and NPG_30min where the intensity of the pure Au phase gradually enhances with the dealloying time at the expense of the pristine fcc (Au) phase, implying the increase in the number of ligaments being formed, evidenced by Fig. 3 (d) and (e) respectively. When it comes to NPG_1h with 1 h of dealloying, the intensity of the pure Au peaks overcome that of the pristine phase, visible in Fig. 3 (f), although the pristine phase is still present meaning that the sample has not been fully dealloyed. A rough estimation of the lattice parameter gave the value of 0.396 nm confirming the presence of the Au-rich fcc (Au) pristine phase, for which a similar a_0 was determined. This result is related to the limited change in the amount of Fe in the fcc (Au) phase, that remains almost unaffected in the core of the ligaments underneath the Au-rich layer produced by Au ad-atoms surface diffusion. For NPG_8h, the XRD pattern in Fig. 3 (g) shows that the amount of fcc (Au) solid solution is decreased with respect to the previous samples while the amount of almost pure Au phase has increased depicted by the reduced intensity of the fcc (Au) solid solution peaks and conversely, the increased intensity of the pure Au peaks. This, obviously, means that more Au-rich ligaments have formed as a result of longer duration of the dealloying treatment. Interestingly, the fcc (Au) phase is present even after 8 hours of the treatment revealing that a certain amount of Fe still exists in this phase which is not dealloyed.

The SEM-SE images of NPG_1h, NPG_2h, NPG_4h, NPG_6h and NPG_8h samples are presented in Fig. 5. The sample NPG_1h (Fig. 5 (a)) exhibits a bimodal bicontinuous nanoporous morphology extended throughout the surface. There are small regions comprised of fine ligaments (approximately 29 nm) and surrounded by regions with comparatively bigger ligaments (approximately 52 nm). This bimodal morphology seems to be a result of variation in the distribution of Au and Fe content in the as-quenched ribbon. The finer morphology must have originated from the dark dendritic grains of bcc α(Fe) phase as already shown in Fig. 1 (c), while the coarser one from the surrounding area rich in fcc (Au) phase. During dealloying, Fe was removed from both the phases but the presence of relatively higher Au content in the surrounding region resulted in slower rate of dealloying and faster surface diffusion of the Au atoms leading to formation of thicker and bigger ligaments. In addition, due to higher Fe content in the dark dendritic grains the dealloying rate is high leading to formation of finer ligaments. As the duration of the dealloying treatment is increased, e.g., in NPG_2h, this morphological distinction tends to fade out slightly. This effect augments on increasing the dealloying time further as it allows the ligaments to diffuse into neighbouring regions colleting and homogenizing the overall morphology.

Eventually, the surface becomes more homogeneous and ligament sizes are in unison, i.e., 43 nm (Fig. 5 (e)). Moreover, coarsening is also observed at the same time during the process because of increased dealloying time as a consequence of which slight coverage of the nanopores can be noticed. Cross-sectional SEM images of NPG_1h, NPG_2h, NPG_4h and NPG_6h have been provided in Fig. 6. The EDS analysis gives the Au and Fe composition of

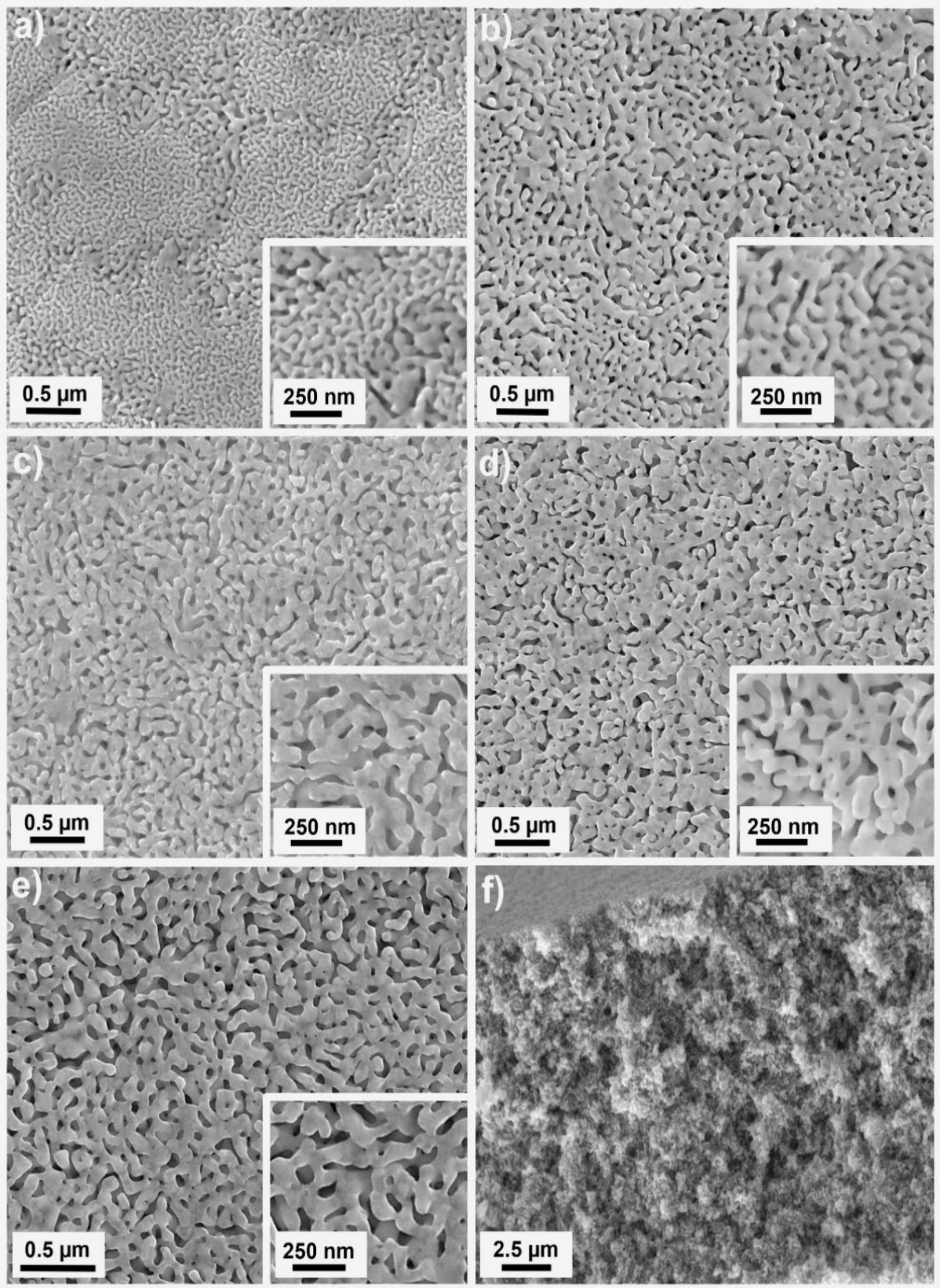

Fig. 5. SEM-SE images of (a) NPG_1h; (b) NPG_2h; (c) NPG_4h; and (d) NPG_6h; (e) NPG_8h; and (f) cross-section of NPG_8h. The insets show magnified view of respective samples.

each sample as follows: 65 at. % Au and 35 at. % Fe for NPG_1h; 71 at. % Au and 29 at. % Fe for NPG_2h; 81 at. % Au and 19 at. % Fe for NPG_4h; 88 at. % Au and 12 at. % Fe for NPG_6h; and 92 at. % Au and 8 at. % Fe for NPG_8h. To summarize, with the increase in the dealloying time an increase is noticed in - (i) the atomic percentage of Au; (ii) the ligament size; (iii) the homogeneity of the surface morphology.

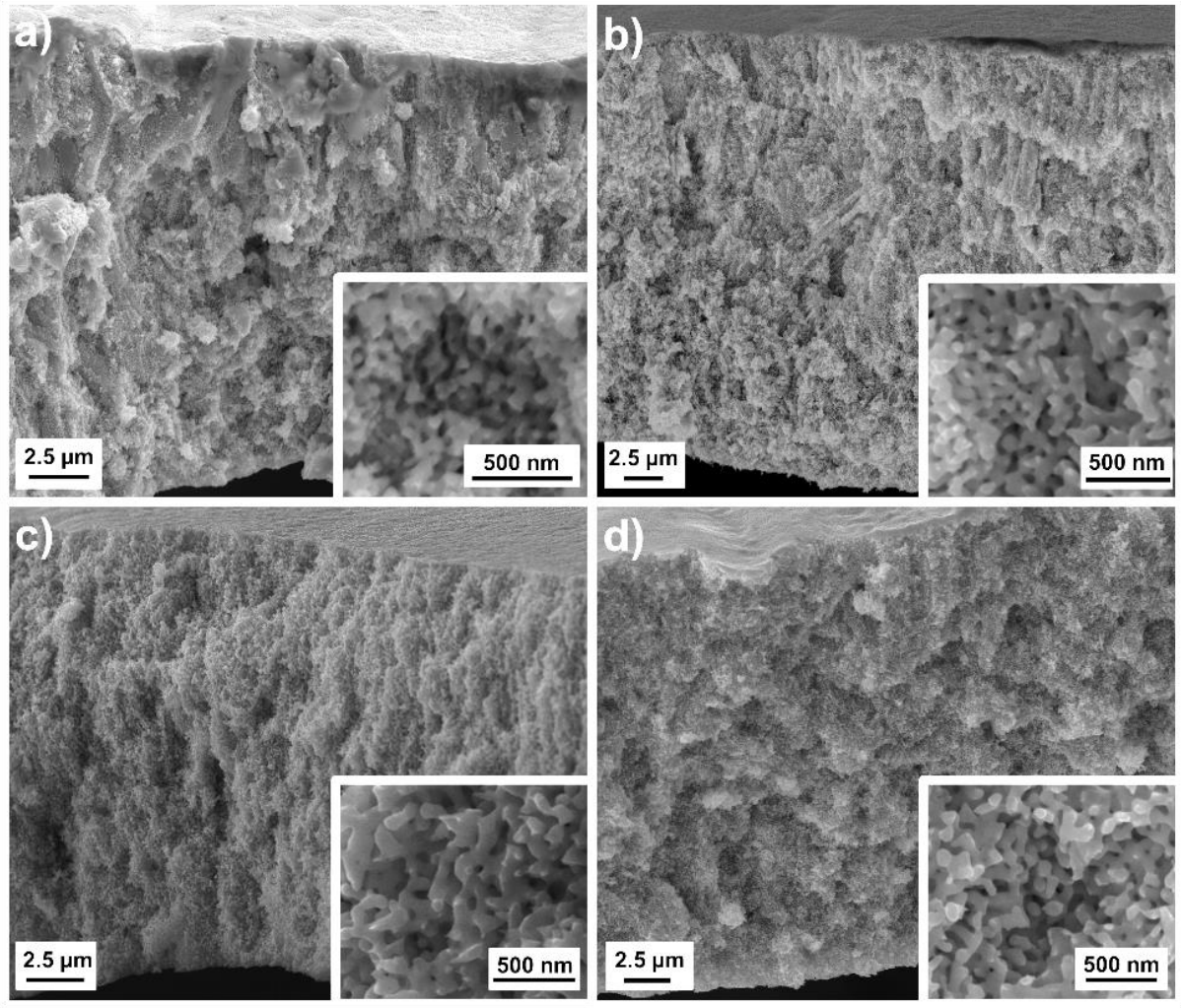

Fig. 6. SEM-SE cross-sectional images of (a) NPG_1h; (b) NPG_2h; (c) NPG_4h; and (d) NPG_6h with the insets showing magnified view of respective samples.

- **Electrochemical dealloying**

Electrochemical dealloying of the as-quenched ribbon was also conducted in 1 M HNO_3 at 70 ºC for different durations of time in a bid to compare with the samples prepared from chemical dealloying. The electrochemical cell setup comsisted of the standard three-electrode configuration, i.e., saturated Ag/AgCl double-bridge reference electrode, Pt-grid counter-electrode and the as-quenched ribbon as the working electrode. Polarization curves of the as-quenched ribbon were obtained and dealloying potential was determined to be 0.6 V vs

Ag/AgCl. Fig. 7 displays the SEM-SE images of one of the as-prepared NPG samples which was dealloyed for 90 minutes (NPG_ED_90min). It is evident that the sample has nanoporous and coarsened morphology with several ligaments joining together and covering the pores. EDS determined the Au content to be 84 at. %. When compared with the chemically dealloyed samples in terms of homogeneous morphology, Au-rich composition and EASA the latter proved to be better. Thus, further study on the electrochemially dealloyed samples was discontinued with the aim of focussing on the chemically dealloyed samples which seemed to pose more promise.

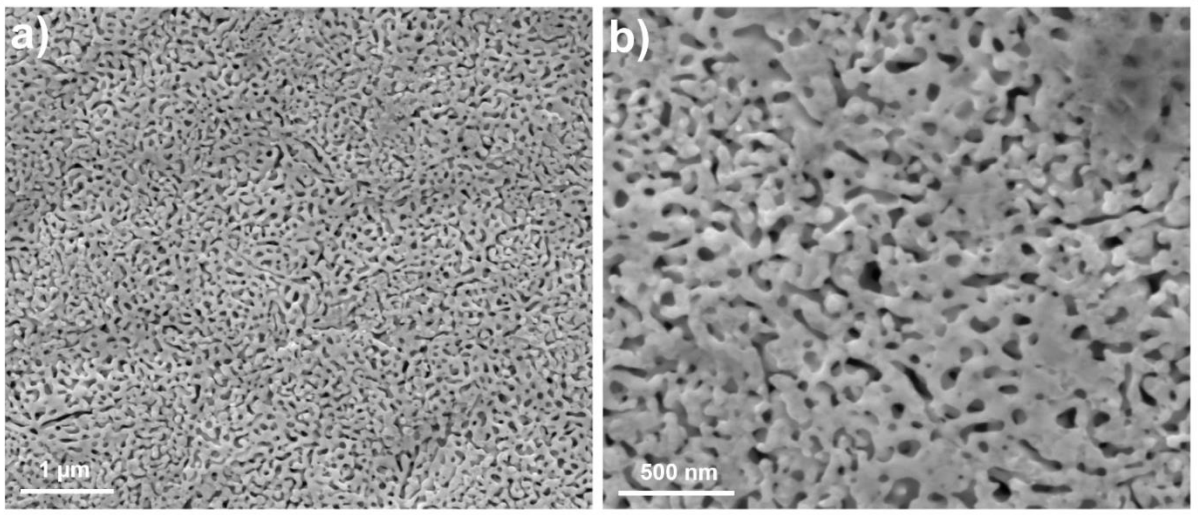

Fig. 7. SEM-SE images of NPG_ED_90min.

3.2.1.1. Hydrogen Evolution Reaction studies

The sample used for HER experiments was NPG_8h as, when compared to the other samples, it has the largest surface area evidenced by the CV measurements provided in Fig. 9. Since the active sites on the surface of a catalyst usually increase in number with increasing surface area, NPG_8h has the greatest number of active sites potentially generating the highest catalytic activity [53]. In addition, it possesses a homogeneous nanoporous morphology with the highest Au content, i.e., 92 at. %. The unique and highly curved morphology permeating the NPG sample exhibits a high density of low coordination sites such as steps, holes and kinks which interact more strongly with the target molecules [53].

Fig. 10 (a) depicts the obtained HER polarization curves. The sample shows a current density of -5 mA cm^{-2} at an overpotential of -0.38 V. As evident from Fig. 10 (b) below, the obtained onset potential is -4 mV which is better than that for a bare Pt sheet, i.e., -13 mV. On comparison it is clear that the obtained onset potential is superior to numerous already reported electrocatalysts: -48 mV for nanostructured porous gold film (NPGF) [54]; -53.8 mV for self-supported Ni_3S_2 film on a nanoporous copper (Ni_3S_2@NPC) electrode [55]; 59 mV for Co, N-co-doped nanotube/graphene 1D/2D heterostructure (Co/NCNT/NG) [56]; -85

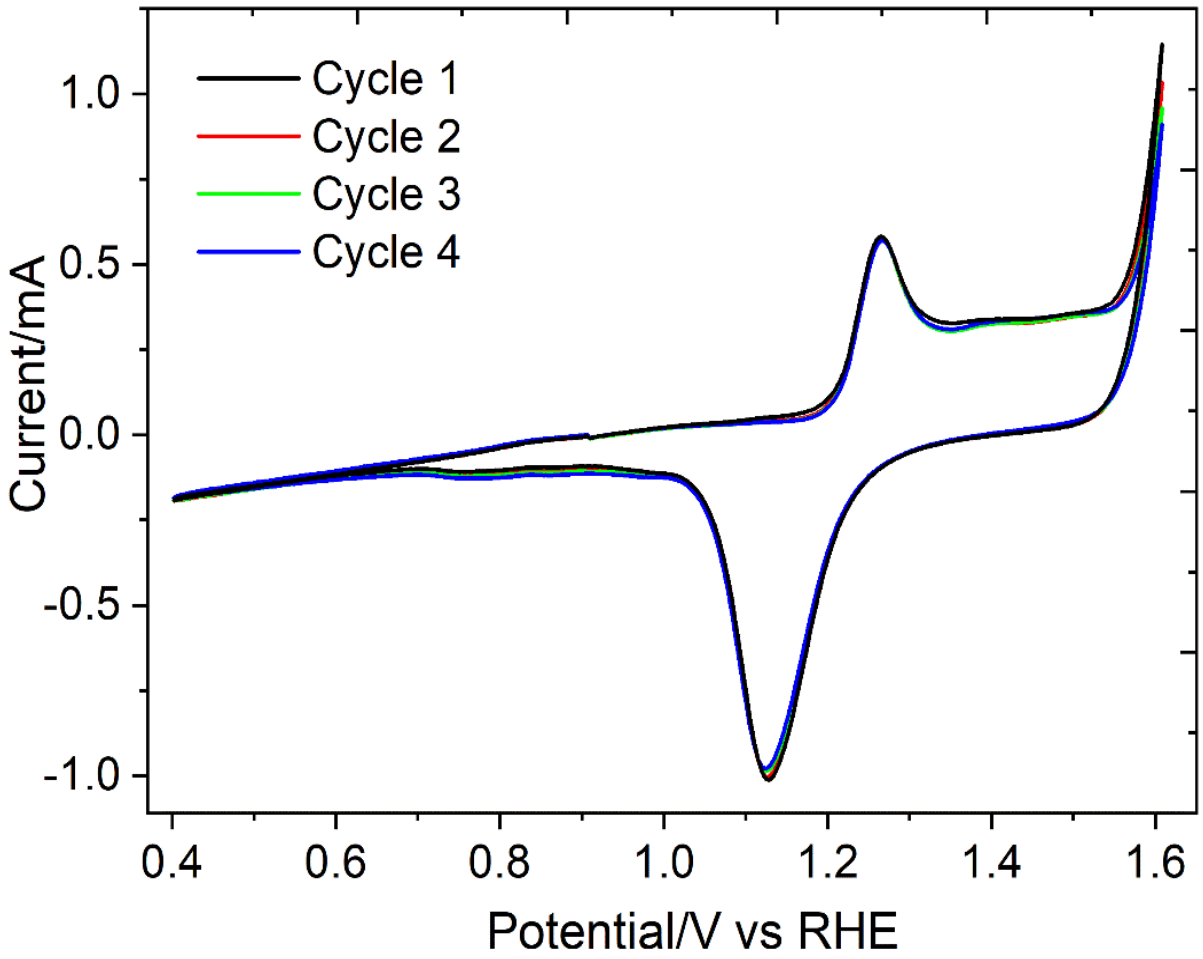

Fig. 8. CV curves for EASA determination of NPG_8h in 0.5 M KOH at a scan rate of 20 mV s^{-1}.

mV for bio-derived nanoporous activated carbon sheets [57]; 142 mV for MoS_2 nanosheets on 3D conductive MoO_2 (3D MoS_2/MoO_2) [58]; and -164 mV for electrodeposited tungsten disulfide/poly(3,4-ethylenedioxythiophene) (WS_2/PEDOT) composites onto nanoporous gold [59].

As mentioned in the previous chapter on Nanostructured Molybdenum Oxides, the Tafel plot is an important parameter that needs to be considered while examining the electrocatalytic potential of an electrocatalyst for HER. In this study, from the plot of the overpotential vs log of current density Tafel plot was estimated by linearly fitting the region after the onset potential of the curve according to the following equation,

$$\eta = b \log j + a$$

where η is the overpotential, j is the current density and b is the Tafel slope. Based on the value of the Tafel slope the rate-determining step (r.d.s.) of the HER can be predicted: if the slope is 120 mV dec^{-1} or higher, the r.d.s. is the Volmer reaction; slopes of 40 mV dec^{-1}

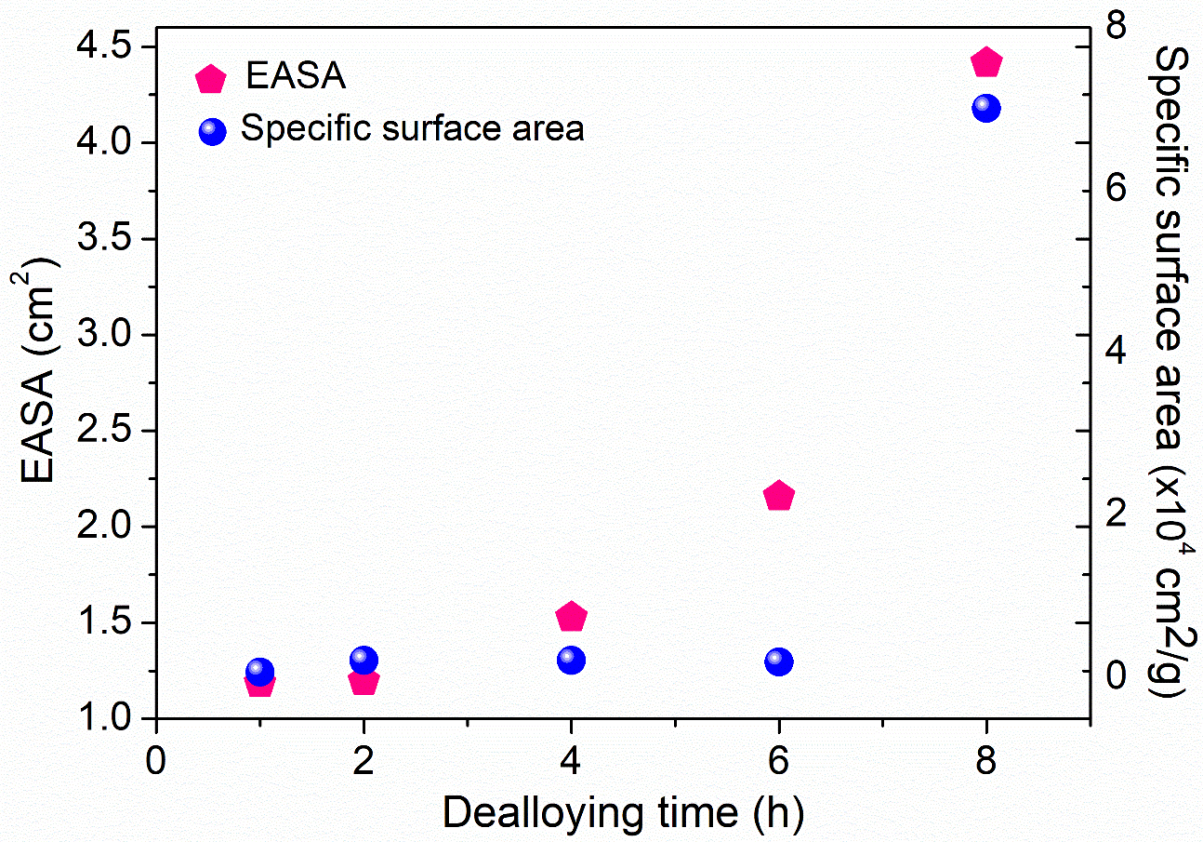

Fig. 9. Dependence of as-determined EASA (y-axis on the left) and specific surface area (y-axis on the right) on the dealloying time.

indicate that the r.d.s is the Heyrovsky reaction while Tafel step is the r.d.s. if the slope decreases to a value of 30 mV dec^{-1} [60]. From Fig. 10 (c), the Tafel slope for NPG_8h is determined to be 47 mV dec^{-1} which is much lower than that for Pt, i.e., 50 mV dec^{-1}. This signifies that a huge increment in the current density is achieved with a small increase in the overpotential. The rate-determining step in this case should be the Heyrovsky reaction. The obtained Tafel slope value of 47 mV dec^{-1} proves to be better than quite a number of electrocatalysts such as 51 mV dec^{-1} for nanoporous ruthenium (np-Ru) [61]; 53 mV dec^{-1} for WS_2/PEDOT [59]; 54 mV dec^{-1} for MoP nanoparticle supported on N,P- codoped reduced graphene oxide (MoP/N,P-rGO) [62]; 63.5 mV dec^{-1} for Ni3S2@NPC [55]; 67 mV dec^{-1} for Co/NCNT/NG [56]; 74 mV dec^{-1} for nanoporous gold/tungsten sulfide composite film [63]; and 85 mV dec^{-1} for NACS [57]. From the intercept of the Tafel plot a high value of exchange current density is determined as 0.12 mA cm^{-2} indicating high current generation at a given overpotential [64]. This indicates high activity of the electrode surface which is accredited to a lower energy barrier for the charge to overcome so as to move from the electrolyte to the catalyst surface, and vice versa, resulting in faster electrochemical reactions [64]. The obtained exchange current density, i.e., 0.12 mA cm^{-2}, is comparable to 0.126 mA cm^{-2} achieved in case of NPGF [54] while exceeding the value of 8.32×10^{-9} mA cm^{-2} for Au-Pd alloy nanoparticles electrodeposited on microwave assisted sol-gel-derived carbon

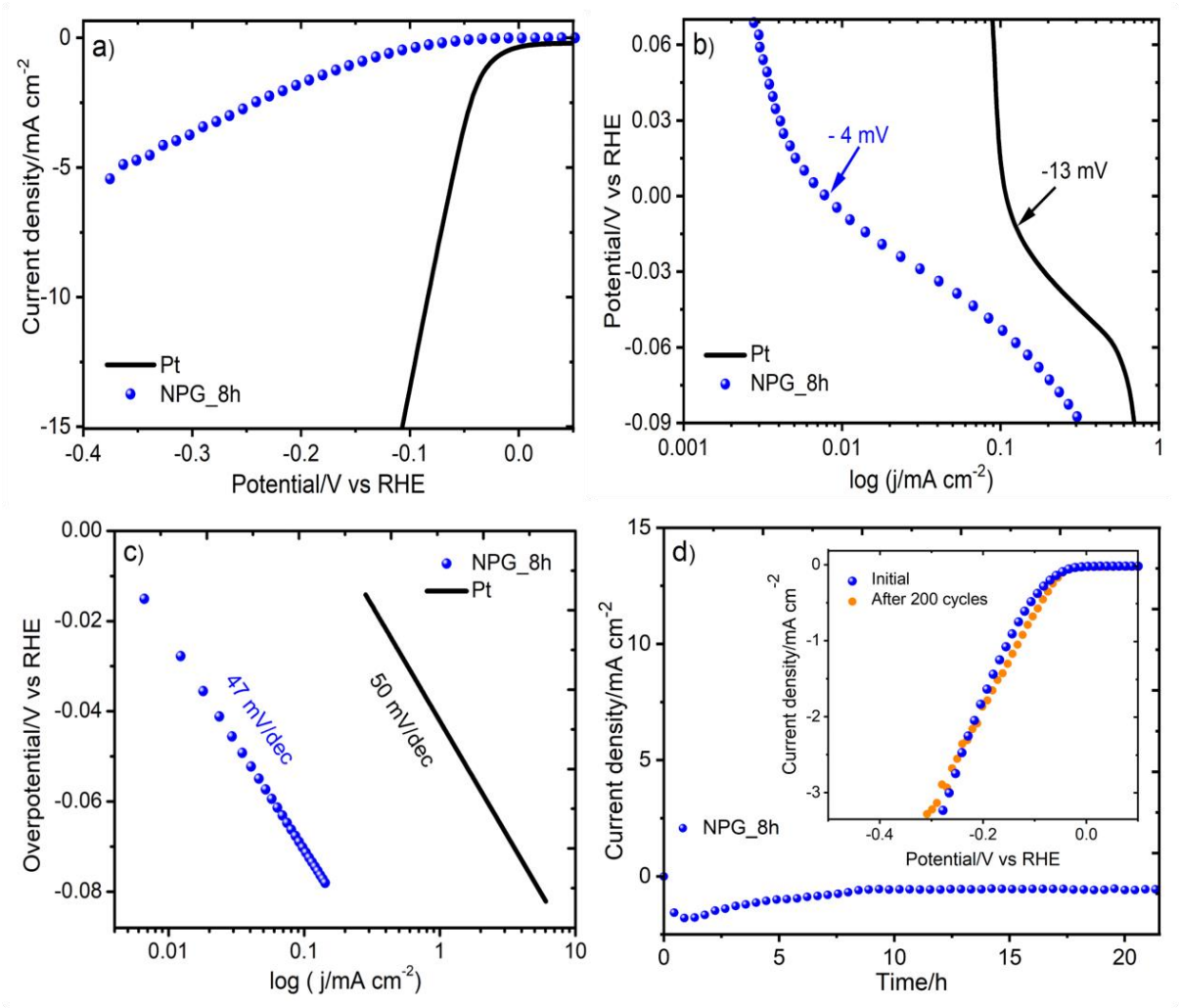

Fig. 10. (a) LSV polarisation curves, (b) Onset potentials and (c) Tafel slopes for pure Pt (black solid line) and NPG_8h (blue spheres) (d) Chronoamperometric measurement for NPG_8h and inset shows the LSV polarization curves after 200 cycles of potential scans for NPG_8h.

ceramic electrodes, namely Au-MWCCE [65]; $5.9x10^{-5}$ mA cm^{-2} for $CoTe_2$ nanoparticles [66]; and 9.0×10^{-4} mA cm^{-2} for 3D MoS_2/MoO_2 [58]; 0.04 mA cm^{-2} for WS_2/PEDOT [59]; $9.2x10^{-4}$ mA cm^{-2} for cocoon-like molybdenum sulfide nanostructures (MoS_2-Mo-1h) [67]; $1.92x10^{-3}$ mA cm^2 for N-doped carbon coated Co–Ni alloy with reduced graphene oxide decoration (CoNi@N-C/rGO) [68]; 0.017 mA cm^{-2} for hierarchical β-Mo_2C nanotubes [69]; and 0.017 mA cm^{-2} reported for Pd-modified carbon fibre electrode [70,71]. To evaluate the stability of the electrocatalyst, chronoamperometric measurement was performed in 0.5 M H_2SO_4 applying a potential of -0.18 V vs RHE as shown in Fig. 10 (d). The current demonstrates remarkable stability for more than 20 h. In addition, LSV polarization curves were obtained for NPG_8h at a scan rate of 2 mV/s for 200 cycles of potential scans as depicted in the inset of Fig. 10 (d). No visible change of the electrolyte colour nor of the

electrode surface morphology was observed during the course or at the end of the measurements.

The brilliant catalytic performance of the NPG sample is ascribed to the innumerable active sites present in the sample by virtue of its nanoporous morphology, structure and composition. Low-coordinated Au sites, such as step, edge or kink sites along with the structural defects act as active sites within the porous scaffold of the NPG sample [53]. During the reaction, the reactant species get trapped within the nanoporous geometry of the sample displaying a nano-confinement phenomenon [72]. The trapped species then experience numerous collisions with the active sites enhancing the overall reaction efficiency [72]. Besides, the residual atoms of Fe, being a catalytically active metal itself, present in the NPG sample, also contribute to the defect sites thereby elevating the sample's total electrocatalytic proficiency [72,73].

Overall, based on these outstanding findings NPG_8h exhibits quite promising potential to be an electrocatalyst for HER. Since a simple, fast and cost-effective dealloying procedure has been used to obtain NPG_8h from a low-cost precursor, it can serve as a favourable alternative to Pt.

3.2.1.2. SERS studies

Noble metal based nanomaterials have been known to display strong SERS enhancement originated from their unique surface plasmon resonance properties. [74] In the same thread, we tested NPG_8h for its performance as a SERS-active substrate owing to its homogeneous nanoporous morphology, highest Au-rich composition as well as the largest EASA. The 4,4′-bipyridine (bipy) was selected as the probe molecule. The sample was immersed for 20 minutes in ethanol solution of bipyridine with different concentrations, i.e., in the range 10^{-9} M, 10^{-12} M and 10^{-15} M bipyridine, after which the SERS effect was tested. Notably, the main objective of this SERS investigation was to estimate the low detection limit (LOD) of the NPG sample. Before and after the treatment, the sample was free-standing, bendable and easily handled with tweezers showing favorable characteristics for a substrate in SERS application.

After 20 minutes of immersion in 10^{-15} M bipyridine solution SERS spectra on both surfaces of the sample were obtained after exciting by a 785 nm laser at five arbitrarily selected sites on each side as shown in Fig. 11 (a). At 1614, 1297, 1233, 1077 and 1026 cm^{-1} the characteristic peaks can be detected, fairly agreeing with the literature [27]. A variation in the spectra is observed in terms of the band width and relative intensity at different sites which is caused by the adsorption kinetics and orientation of molecules along with the electromagnetic field disparity at each ‘‘hotspot” [32]. Figs. 12 (a) and (b) show the SERS spectra obtained for 10^{-9} M and 10^{-12} M bipyridine solution using a 785 nm laser at five arbitrarily selected sites. The main reason for the observed enhancement of SERS effect on NPG is the well-established electromagnetic mechanism related to efficient excitation and trapping of surface

plasmons [75], with an additional effect of electromagnetic field localization in the pore regions [76]. The unique bi-continuous pore-ligament framework of the NPG sample with highly curved morphology possesses a high density of low coordination sites such as steps, holes and kinks which interact strongly with the target molecules [53]. This allows for a conducive generation of local Raman ‘‘hot spots” where the resonant excitation of localized surface plasmons enables intense enhancements of local electromagnetic fields [77]. Also, the adjacent gold ligaments experience electromagnetic coupling which further leads to improvement in the localized field intensity adding to the overall SERS enhancement [78]. A graph depicting the spectrum with the most intense Raman signals for each bipy concentration can be found in Fig. 13. Fig. 11 (b) below displays the average Raman signal for 10 accumulations per bipy concentration after excluding the extraordinarily high signal arising from a possible hotspot encounter (visible in the case of 10^{-15} M bipy concentration in Fig. 13). In Fig. 11 (c) the relationship between the average SERS intensity at 1614 cm^{-1} and

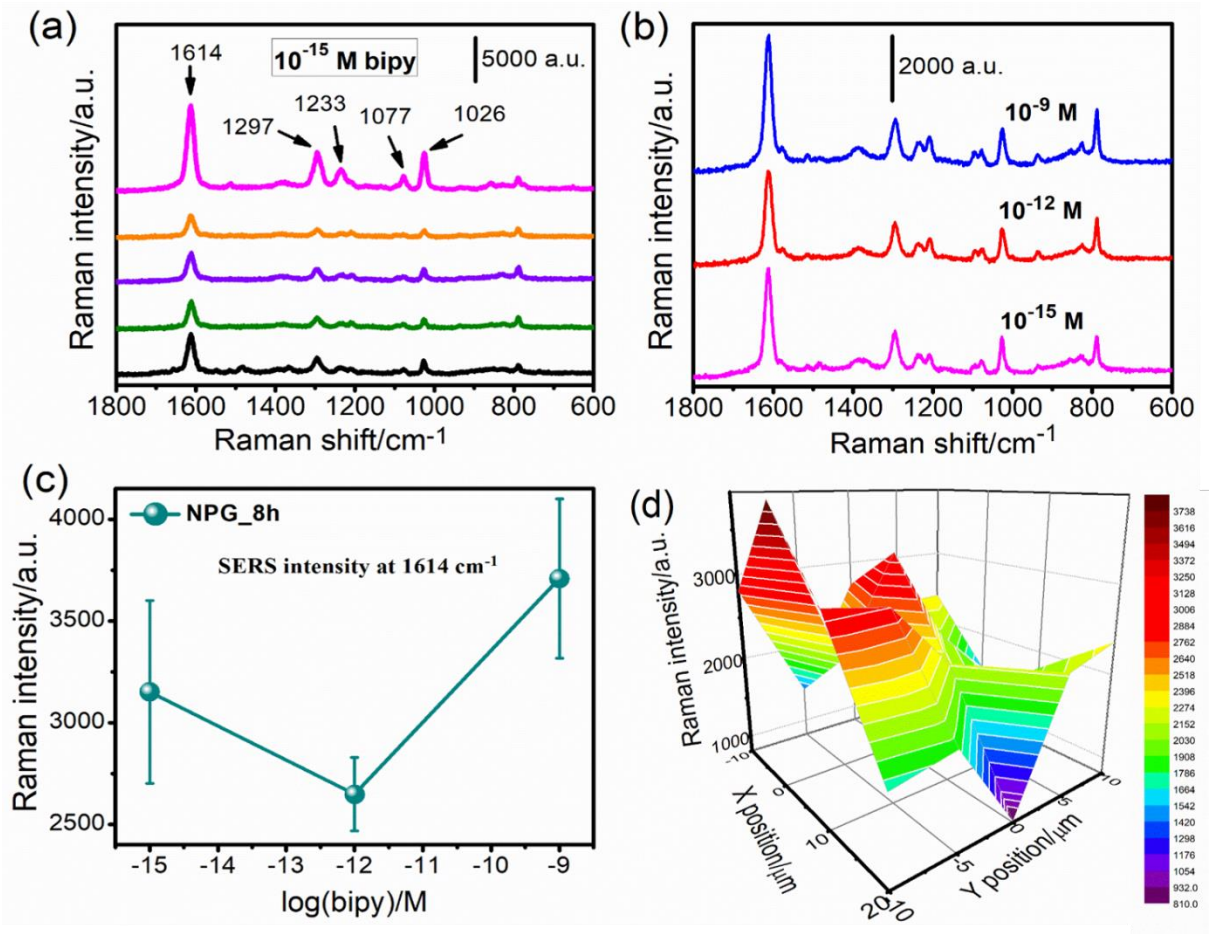

Fig. 11. (a) SERS spectra of 4,40-bipyridine at 10^{-15} M concentration at different sites on NPG_8h. (b) SERS spectra of 4,4′-bipyridine on NPG_8h with 10 accumulations at different concentrations. (c) Relationship between the logarithm of bipyridine concentration and the average SERS intensity at 1614 cm^{-1} and the related error bars. (d) SERS intensity mapping image of 20x30 at 1614 cm^{-1} with bipyridine concentration of 10^{-12} M.

bipyridine concentration is demonstrated; the error bars represent the variation of degree of intensity at each concentration. Considering this average signal intensity and the related errors per bipy concentration there exists a decreasing trend of SERS intensity as a function of the decreasing concentration of the analyte considering the error bars which is in agreement with the literature. The detection limit is as low as 10^{-15} M which is an impressive achievement of this NPG sample. When compared to previously reported NPG samples acting as SERS substrates, the detection limit of 10^{-15} M for bypridine exhibited by our sample is lower than that for a number of samples such as $5x10^{-10}$ M for NPG of ligament size 5 nm [35]; 10^{-11} M for NPG obtained by dealloying $Au_{30}Cu_{38}Ag_7Pd_5Si_{20}$ metallic glass precursor electrochemically [34]; 10^{-12} M for lamellar nanoporous gold thin film [79]; 10^{-14} M for NPGs obtained by chemically dealloying $Au_{30}Cu_{38}Ag_7Pd_5Si_{20}$ amorphous alloy [22] and $Au_{20}Cu_{48}Ag_7Pd_5Si_{20}$ metallic glass precursor [27] respectively. Fig. 11 (d) shows SERS intensity mapping image at 1614 cm^{-1} with bipyridine concentration of 10^{-12} M under the same condition of single measurement. This mapping image evidently depicts the presence of ‘‘hotspots”.

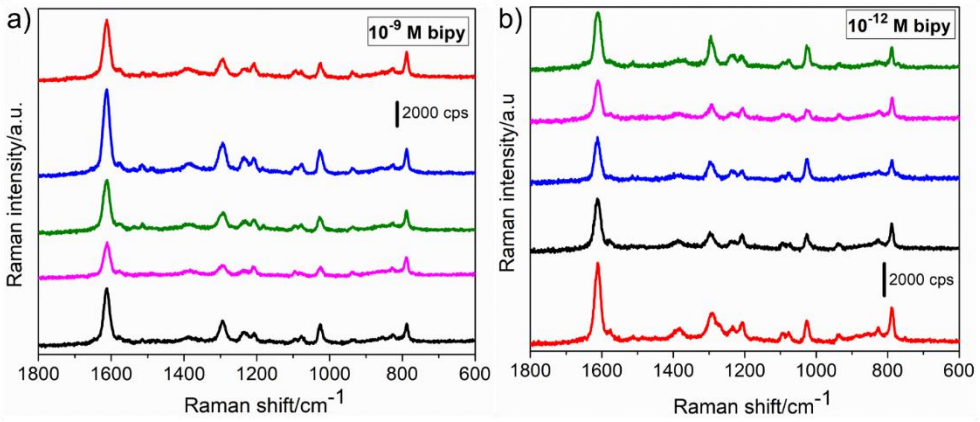

Fig. 12. SERS spectra of all five measurements of 4,4′-bipyridine on NPG_8h with 10 accumulations at concentration of (a) 10^{-9} M (b) 10^{-12} M.

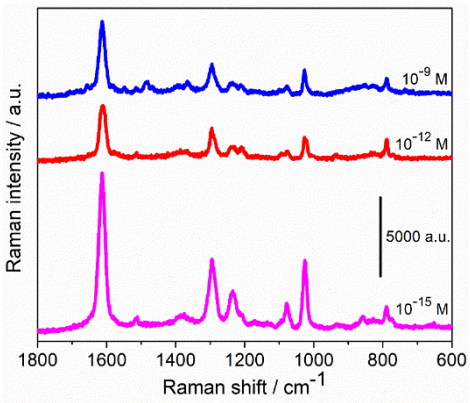

Fig. 13. SERS spectra of 4,4′-bipyridine on NPG_8h with 10 accumulations each at concentrations of 10^{-9} M, 10^{-12} M and 10^{-15} M. Out of the five measurements the most intense Raman spectrum has been showed here for each concentration.

3.2.2. NPG from HCl

Another batch of NPG samples was prepared by employing a different etching electrolyte, i.e., 1 M HCl which is also an effective electrolyte to selectively dissolve Fe while being resistant to Au. Various experimental conditions were applied for the fabrication of high quality, free-standing, homogeneous NPG samples. Out of the different trials, the batch of NPG samples fabricated at 70 ºC for varied duration of dealloying time has been discussed below in detail. To point out, the as-quenched $Au_{33}Fe_{67}$ ribbon used in the previous paragraph was maintained to be used as a precursor for this batch of NPG samples as well. The following part reveals the details about the NPG samples, their characterization and application.

Chemical dealloying of the as-quenched ribbon was performed in 1 M HCl at 70 °C for 8 h (NPG_HCl_8h), 12 h (NPG_HCl_12h), 14 h (NPG_HCl_14h) and 16 h (NPG_HCl_16h). Fig. 14 below shows the XRD pattern of the as-quenched ribbon in (a) where the phases in the microstructure of the ribbons described earlier are established, and the XRD pattern for NPG_HCl_16h as a representative in (b). The emergence of a new fcc phase is detected in the pattern for NPG_HCl_16h denoted by the cyan triangles.

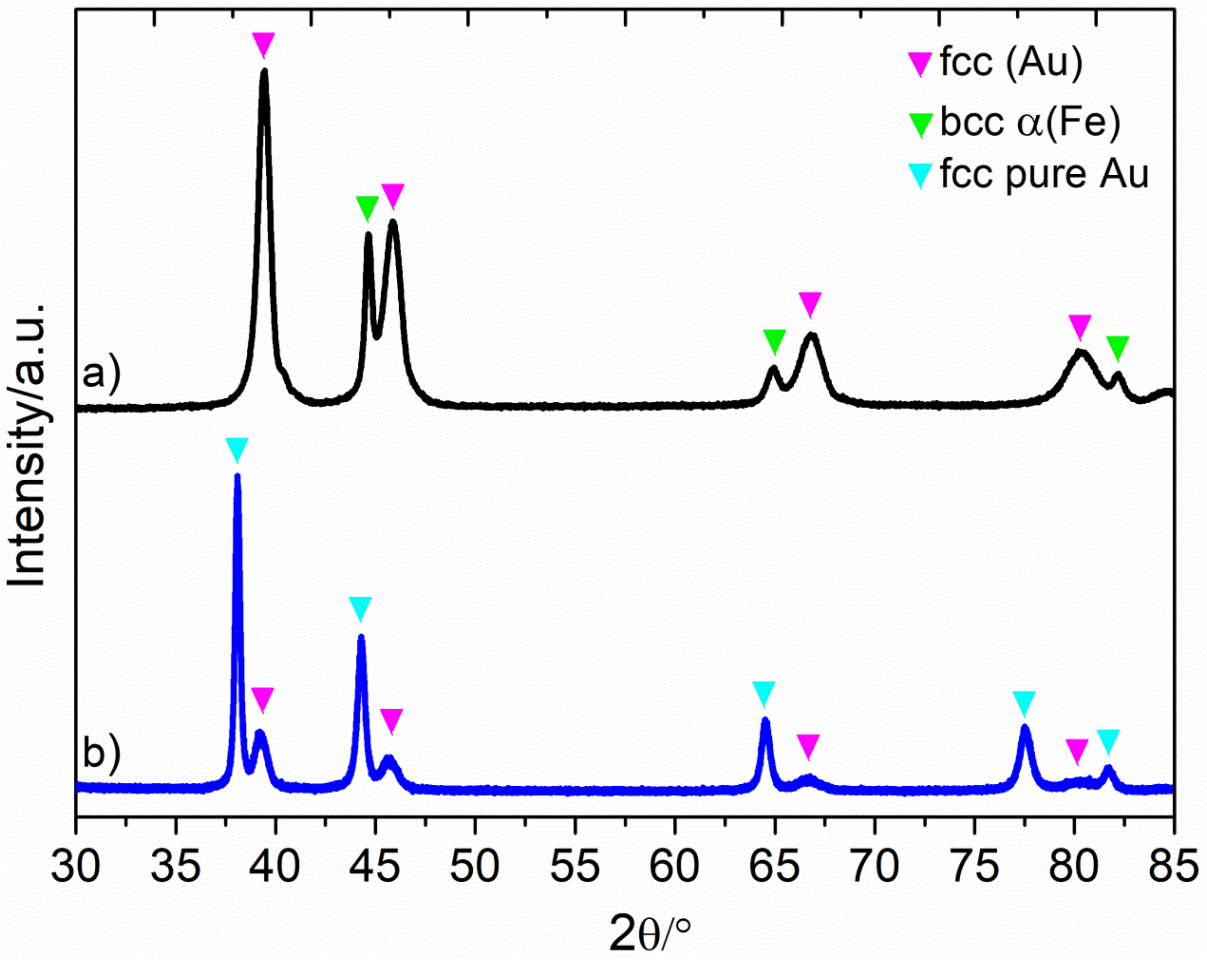

Fig. 14. XRD patterns of **(a)** the as-quenched ribbon and **(b)** NPG_HCl_16h.

The lattice parameter of this fcc phase approaches that of pure Au which signals towards the formation of Au-rich ligaments as expected. The creation of the pore-ligamentous framework takes place simultaneously with the Fe removal, as a result of surface diffusion of the Au ad-atoms on the surface of the pristine phase. Small amount of this pristine phase still appears after 16 hours of dealloying in the form of less intense yet visible peaks, revealing the presence of a certain amount of non-dealloyed Fe content still existing in this phase. This observation is in accordance with the EDS analysis presented in the coming paragraph that shows the presence of approximately 9 at. % Fe in the sample.

In Fig. 15, the SEM secondary electron (SEM-SE) images for all the as-dealloyed samples are presented. The EDS analysis in terms of the Au composition gives the value 75 at. % for NPG_HCl_8h; 85 at. % for NPG_HCl_12h; 88 at. % for NPG_HCl_14h and 91 at. % for NPG_HCl_16h. The sample NPG_HCl_8h (Fig. 15 (a)) exhibits a widespread bicontinuous homogeneous nanoporous morphology. NPG_HCl_12h shows similar morphology. When the duration of the dealloying treatment is further increased, as in the case of NPG_HCl_14h, the

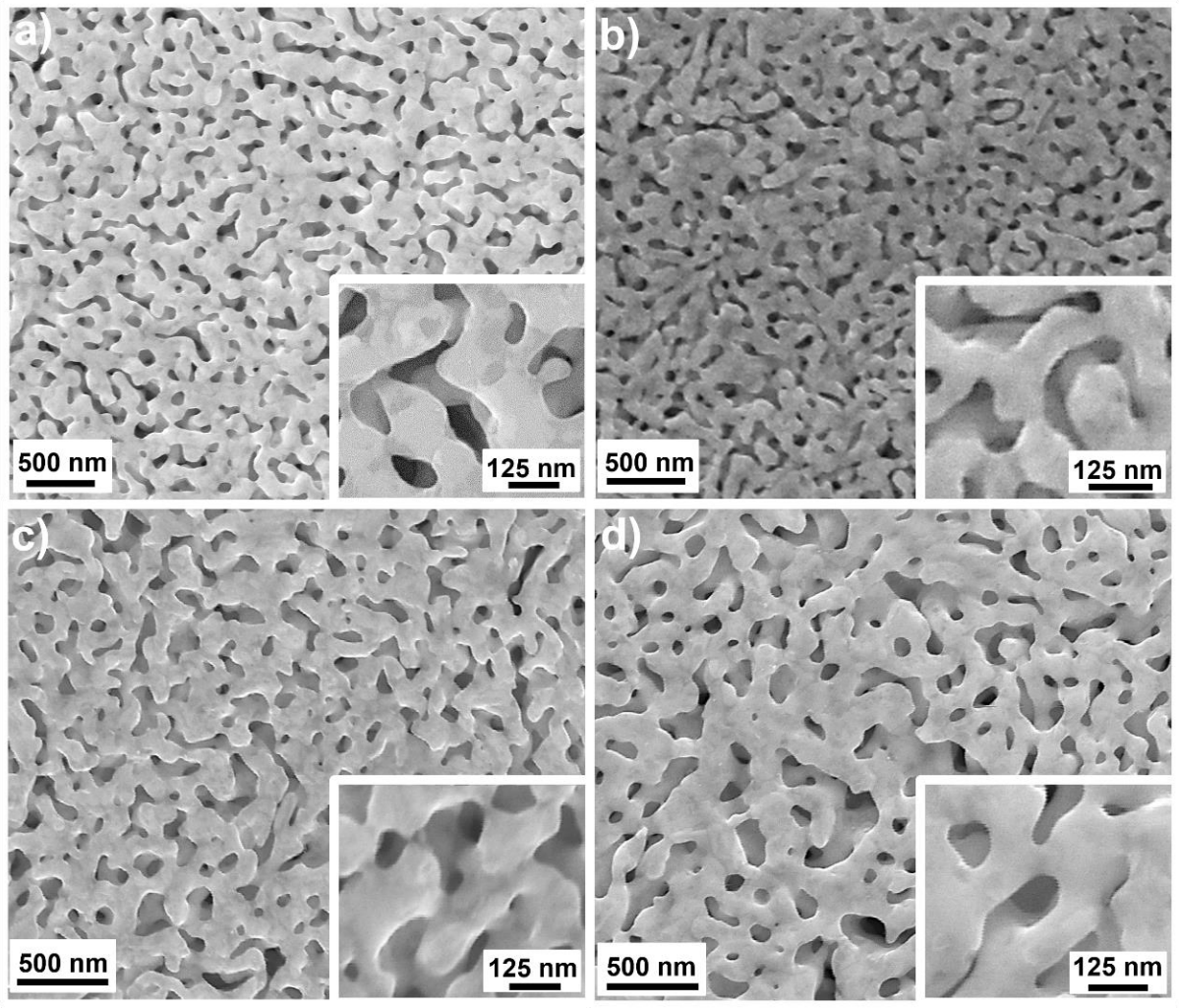

Fig. 15. SEM-SE images of surface view of **(a)** NPG_HCl_8h, **(b)** NPG_HCl_12h, **(c)** NPG_HCl_14h and **(d)** NPG_HCl_16h.

appearance of a more coarsened morphology is noticeable. This coarsening effect is amplified with NPG_HCl_16h ligaments diffuse into neighbouring regions, coalesce and form thicker and bigger ligaments resulting in overall coarsened yet homogeneous nanoporous morphology, visible in the case of NPG_HCl_16h. Cross-sectional SEM images of NPG_HCl_8h, NPG_HCl_12h, NPG_HCl_14h and NPG_HCl_16h have been provided in Fig. 16. It can be inferred that dealloying has been achieved only partially in the cross-section for NPG_HCl_8h shown by the nanoplates/nanosheets observed in the SEM image. A possible reason could be that the dealloying time is not enough to facilitate complete dealloying. So, when the dealloying time is increased, the samples become more Au-rich in composition and ultimately, NPG_HCl_16h reaches the maximum degree of dealloying giving 91 at. % of Au as determined by EDS.

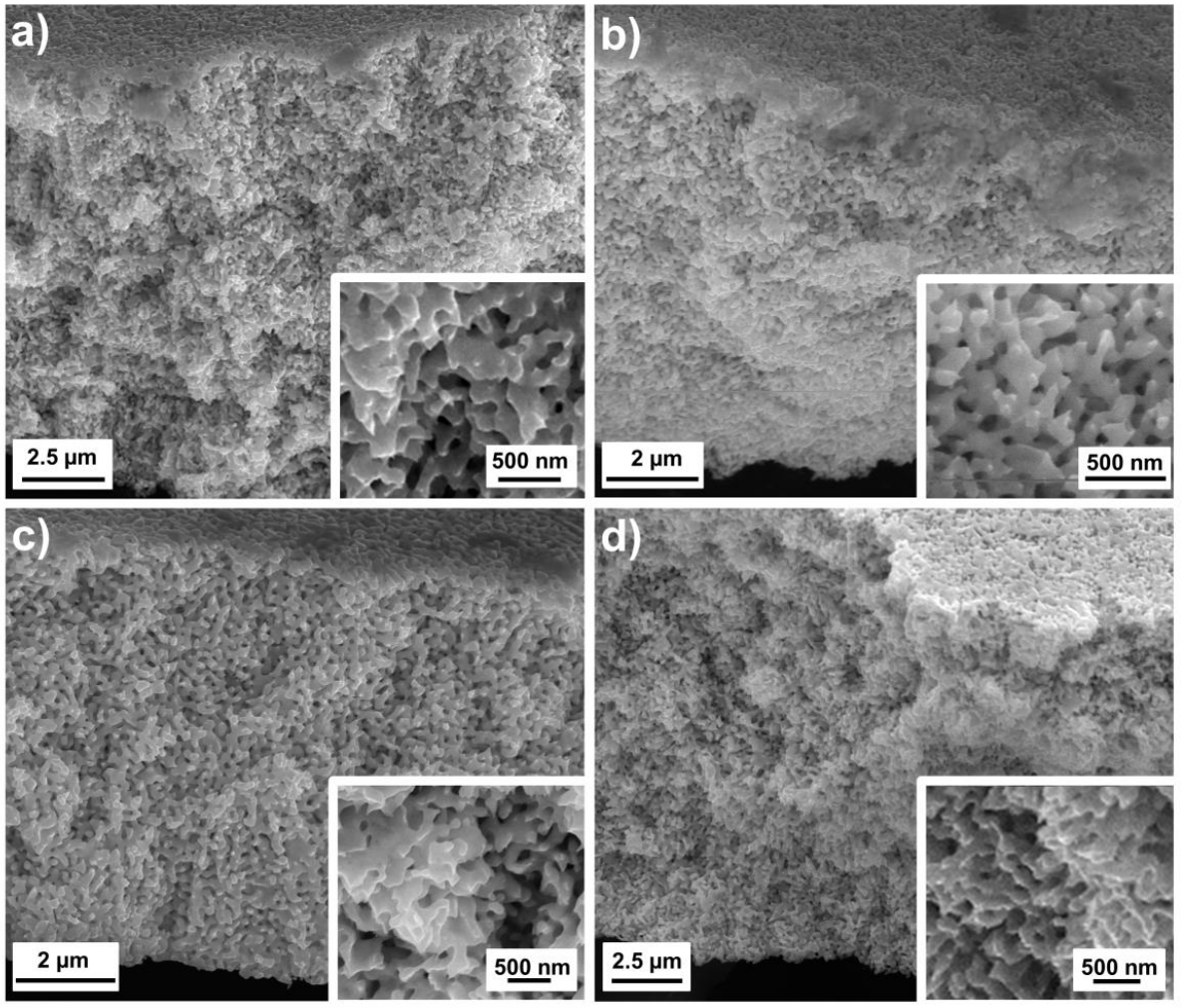

Fig. 16. SEM-SE cross-sectional images of (a) NPG_HCl_8h, (b) NPG_HCl_12h, (c) NPG_HCl_14h and (d) NPG_HCl_16h with the insets showing magnified view of respective samples.

3.2.2.1. Electrochemical behaviour in basic solution

The as-dealloyed NPG_HCl_16 h was subjected to Cyclic voltammetry (CV) scans in 0.5 M KOH as provided in Fig. 17 (a). The obtained curve reflects the occurrence of various processes on the surface of the sample on account of their composition and microstructure. While forward scan is underway, OH^- ions are chemisorbed on the sample surface, in the non-faradaic potential range, resulting in the creation of a layer of hydroxy intermediate, Au-$OH(1-\lambda)^-$ where λ stands for the charge transfer coefficient._This intermediate layer is then utilized in the formation of Au oxides [5,7], marked by the current peak at around 0.29 V. The backward scans show the peak at 0.1 V obtained as a result of reduction of Au oxides. The position of this reduction peak in hardly changed in the second cycle and depends on surface composition and the ligament size as known. [5] The EASA of the three samples was measured using the procedure mentioned in the 'Experimental' section previously. Fig. 17 (b) depicts the calculated EASA for each of the three samples. In addition to having the highest EASA, NPG_HCl_16h has the highest dealloyed volume attributed to 16 h of dealloying as reported in previous works. [80] Thus, it must show the highest current density of methanol electrooxidation weighed up to the other samples. [80] For these reasons, NPG_HCl_16h was the sample of choice for the methanol electrooxidation studies.

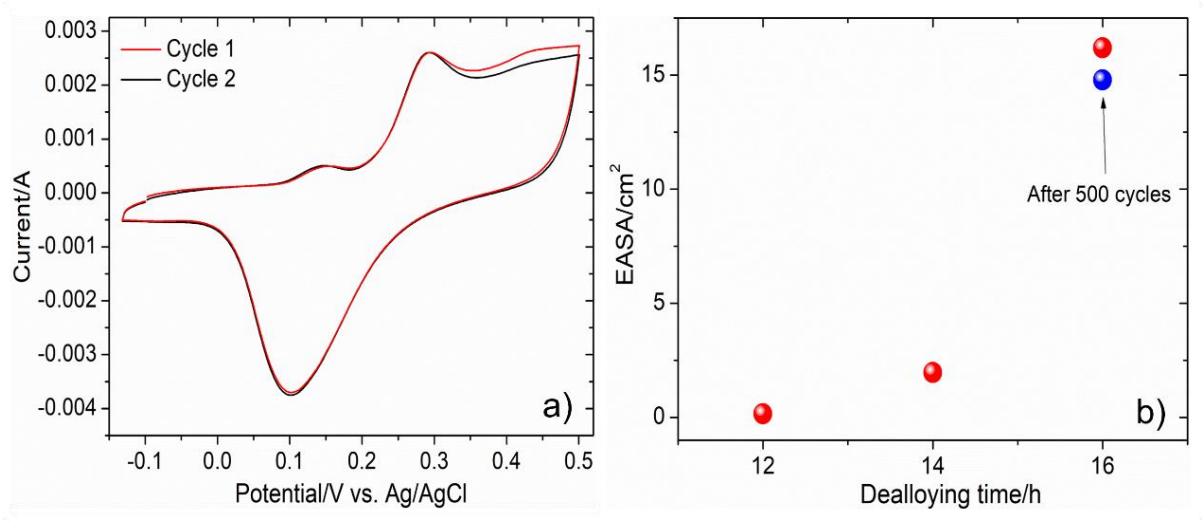

Fig. 17. (a) CV scans of NPG_HCl_16h in the potential range from -0.13 to 0.5 vs Ag/AgCl in 0.5 M KOH solution. **(b)** EASA of NPG_HCl_12h, NPG_HCl_14h and NPG_HCl_16h denoted by red dots befroe methanol electrooxidation and EASA of NPG_HCl_16h denoted by the blue dot after 500 CV scan cycles of methanol electrooxidation.

3.2.2.2. Methanol electrooxidation behaviour

The nanoporous structure of the sample allows for facile electrooxidation of methanol by virtue of its high number of active sites in the form of low-coordinated Au sites, such as step, edge or kink sites along with the structural defects. [72] As shown in the above section

NPG_HCl_16h is electrocatalytically active for methanol oxidation in basic solutions. 500 cycles of CV scan for NPG_HCl_16h have been presented in Fig. 18.

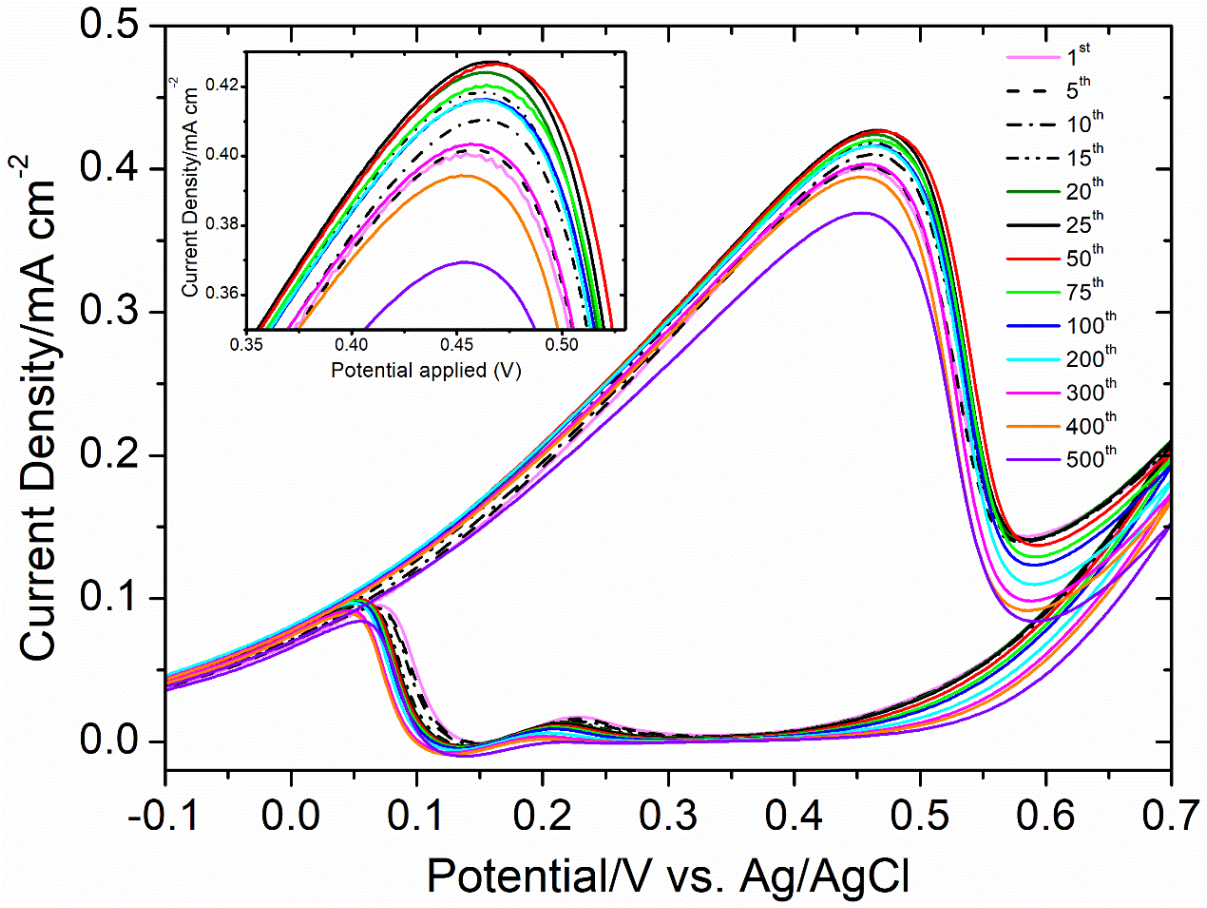

Fig. 18. CV curves of NPG_HCl_16h for 500 scan cycles in a solution of 5 M CH_3OH in 0.5 M KOH at a scan rate of 20 mV/s. The inset gives a magnified look at the potential range, peak potential and peak current density of methanol electrooxidation.

As mentioned previously, during the positive scan and at the onset of the current peak, formation of layer of pre-oxidized species such as Au-OH(1-λ)$^-$ takes place owing to chemisorption of OH^- ions on the sample surface. This intermediate layer of Au-OH(1-λ)$^-$ reacts with methanol present in the solution and oxidises it to formate ions with the exchange of 4 electrons according to the reaction below [5,10,16]:

$$CH_3OH + 5OH^- \rightarrow HCOO^- + 4H_2O + 4e^- \quad (1)$$

The current density at the peak maximum increases cycle by cycle upto the 25th of forward scan. This trend is an indicator of gradual increment in the electrochemical activity of the sample. [41] With respect to the 25th cycle that shows the highest current density, methanol electrooxidation occurs in the potential range of 0.35 V to 0.55 V vs Ag/AgCl. Neat peaks of anodic current corresponding to reaction (1) can be observed in the inset of Fig. 18 with

maxima at the potential of 0.47 V vs Ag/AgCl. After the 25th cycle a decline in current density ensues until the last cycle. This pattern can be linked to the progressive consumption of Au-OH(1-λ)$^{-}$ species in the formation of Au-oxides. [5,16,17] This affects the number of exposed active Au sites sufficiently enough so as to negatively impact the current density after the 25th cycle.[81] But at the same time this drop in current density from 0.43 mA/cm^2 to 0.37 mA/cm^2 is only by 0.06 mA/cm^2 which is not drastic. It indicates that the sample is exceedingly stable retaining its electrochemical activity even after 500 CV cycles with a minute drop in current density.

When the potential is swept in the backward scan direction, the oxidation of methanol is resumed according to reaction (1) in the same potential range where Au oxides are reduced (from 0.25 V to -0.05 V) represented by the reappearance of current peak. The current density demonstrated by this peak augments from the 1st cycle upto the 25th and then faces a steady decay upto the last cycle, i.e., 500th cycle. This trend can also be associated to the same reason as for the forward scan. Greater the methanol electrooxidation, higher the current density.

The poisoning tolerance of electrocatalysts in DMFCs can be evaluated by finding the peak current ratio of the forward to reverse scans (I_f/I_r).[40,82] Generally, higher the If/Ir ratio better is the resistance to electrode poisoning from carbonaceous species.[40] Commercial Pt/C electrocatalyst has a poisoning tolerance of 2.3 while NPG_HCl_16h in this case has a tolerance of 4.35, Table 2 illustrates further comparison with literature.[40] This adds to the overall favourable properties of NPG_HCl_16h sample as a superb alternative for methanol electrooxidation.

Fig. 19 (a) provides a look at the electrochemical stability of the sample where the current density (on the right axis) and peak potential (on the left axis) at the maximum of the CV scan vs the number of cycles is presented. The current density has been normalized with respect to the maximum value recorded in the first cycle. [7] The sample shows remarkable stability after 500 cycles with efficiency of current density down to only 86%. The peak potential also remains quite steady in the potential range of 0.47 V to 0.45 V for all the 500 cycles. Fig. 19 (b) contains the graph of current density normalized with respect to the 25th cycle vs the number of CV cycles. The maximum of the current density of the 25th cycle has been considered as the standard 100% here as it is the highest current density observed and the rest have been normalized accordingly. The electrochemical performance of the sample seems to be decreasing gradually because of coverage of active sites by oxides and other chemical species.

After 500 cycles, the sample was reactivated by immersing in concentrated HNO_3 for 15 min. The EASA of NPG_HCl_16h was measured again after the 500 cycles of CV scan following the same procedure as reported earlier in the 'Experimental' section. The comparison of the EASAs of NPG_HCl_16h before and after the 500 cycles of CV scan is displayed in Fig. 17 (b) in the form of red and blue dot respectively. It is clear that there is only a minor decrement in the EASA which denotes remarkable electrocatalytic capacity, stability and longevity of

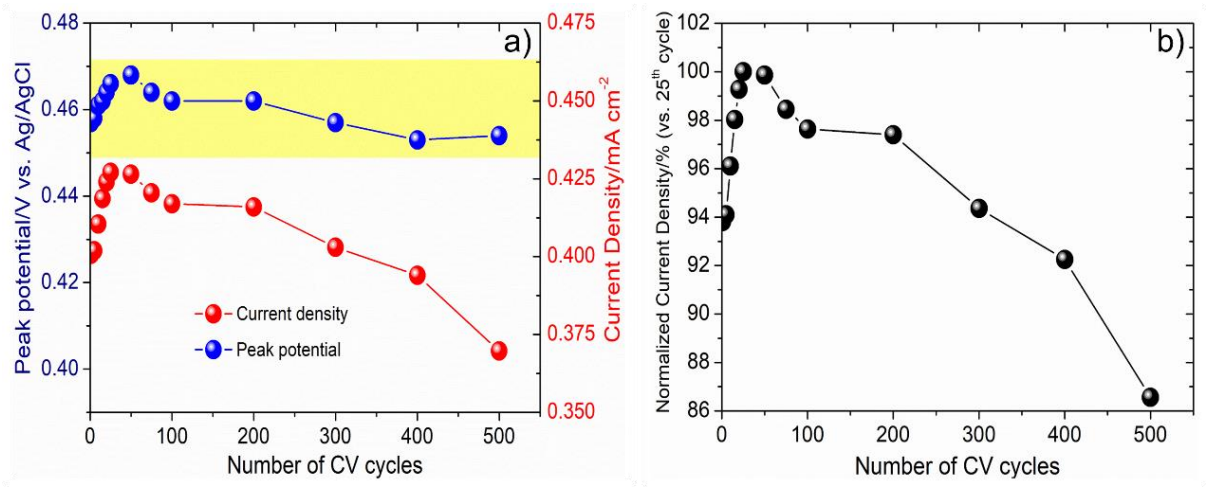

Fig. 19. Graph depicting the stability of NPG_HCl_16h upto 500 CV cycles in terms of **(a)** the peak potential (y-axis on the left) and current density at the peak potential (y-axis on the right) and **(b)** peak current density of methanol electrooxidation normalized with respect to the 25th cycle.

the tested sample. The performance of NPG_HCl_16h from this work has been compared against several contemporary samples reported in literature in terms of peak potentials of methanol oxidation and corresponding current density in Table 1.

Sample	***Electrolyte***	***Scan rate (mV/s)***	***Peak Oxidation voltage***	***Peak oxidation current/ current density***	***Reference***
NPG_HCl_16h	5 M CH_3OH in 0.5 M KOH	20	0.47 V Ag/AgCl	0.43 mA/cm^2	This work
Rh-NSs/RGO hybrids	1 M CH_3OH in 1 M KOH	50	0.61 V Ag/AgCl	0.52 mA/cm^2	[40]
EC/rGO/NiOOH	0.01 M CH_3OH in 0.1 M NaOH	50	0.66 V vs Ag/AgCl	0.75 Ma	[83]
EC/rGO/NiOOH-FeOOH	0.01 M CH_3OH in 0.1 M	50	0.57 V vs Ag/AgCl	0.8 mA	[83]

	NaOH				
Ni–Pt/carbon paper electrode	1 M CH_3OH in 0.5 M KOH	20	-0.2 V vs Ag/AgCl	1.8 mA	[84]
Pt_3Ni nanoparticles	1 M CH_3OH in 0.1 M $HClO_4$	50	1.04 V vs RHE	0.5 mA/cm^2	[85]
Pt/CNTs-80	0.5 M CH_3OH in 0.5 M H_2SO_4	50	0.69 V vs Ag/AgCl	1.83 mA/cm^2	[86]
Pd-Ir-O/NGS	1 M CH_3OH in 1 M KOH	50	0.81 V vs RHE	3.26 $mA\ cm^{-2}$	[87]
$MnCo_2O_4$	0.5 M CH_3OH in 1 M KOH	10	0.7 V vs Ag/AgCl	95 A/g	[88]
$Mn_{0.6}Zn_{0.4}Co_2O_4$/rGO	0.5 M CH_3OH in 1 M KOH	50	0.8 V vs Ag/AgCl	142.3 mA/cm^2	[89]
Pt/MnO2/Rgo	0.5 M CH_3OH in 0.5 M H_2SO_4	50	0.9 V vs RHE	23 mA/cm^2	[82]
Pt/RuO_2/CNT	1 M CH_3OH in 1 M $HClO_4$	-	0.74 V vs Ag/AgCl	609 A/g Pt	[43]
Pt/RuO_2/TiO_2-NTs	0.5 M CH_3OH in 1 M H_2SO_4	0.5	0.8 V	100 mA/cm^2	[90]

C/CoAg	1 M CH_3OH in 0.1 M KOH	50	0.48 V	2.30 A/g C	[91]
C/Co	1 M CH_3OH in 0.1 M KOH	50	0.58 V	0.35 A/g C	[91]
$RuO_2/MnCo_2O_4$/rGO	0.5 M CH_3OH in 1 M KOH	20	0.5 V vs Ag/AgCl	20.44 mA/cm^2	[92]
Pt/p-MDAB/CF	1 M CH_3OH in 0.5 M H_2SO_4	50	0.71 V vs Ag/AgCl	405 mA $mg^{-1}Pt$	[93]
Ni/ZMCPE	0.1 M CH_3OH in 0.1 M NaOH	20	0.68 V vs Ag/AgCl	0.85 mA peak oxidation current	[94]
13XPtRu	0.5 M CH_3OH in 0.5 M NaOH	20	-0.23 V vs Ag/AgCl	0.56 mA	[95]
RGO/bimetallic Pt-Pd alloy/CeO_2	1 M CH_3OH in 0.5 M H_2SO_4	50	0.8 V vs Ag/AgCl	69.82 mA cm^2	[96]
Pt/BNC NTs	1 M CH_3OH in 0.5 M H_2SO_4	50	0.73 V vs Ag/AgCl	0.73 A mg^{-1} Pt	[97]

.

Table 1. Comparison of our work with literature in terms of peak potentials of methanol oxidation and peak current/current density.

Sample name	*Poisoning tolerance*	*Reference*
NPG_HCl_16h	4.35	This work
PtPd-NFs/Cu_2O-NSs/rGO	1.47	[98]
$Pt_3Fe/CeO_2/C$	1.27	[99]
Pt-MnO_2/rGO-L	1.02	[82]
Pt-MoO_3/RGO (16.5% MoO_3)	1.2	[100]
Pt-SiO_2/G-2	1.04	[101]
Pt/MnO_2–RGO	1.12	[102]
RGO/bimetallic Pt-Pd alloy/CeO_2	2.29	[96]
RGO/monometallic Pt/CeO_2	1.52	
RGO/monometallic Pd/CeO_2	1.85	

Table 2. Poisoning tolerance obtained in our work compared with literature.

4. Economic and sustainability factors

An important objective of this work has been to synthesize high quality NPG in a cost-effective and sustainable manner. Discussed below are some reasons which make for a convincing case in favour of this NPG sample as a better alternative for HER, MeOH-EOx and SERS among contemporary candidates:

(i) Considering the current commodity prices in London Metal Exchange, i.e., the world centre for the trading of industrial metals, it is evident that Fe can be procured quite cheaply [103]. The actual price of Fe falls around 450 $/ton while that of some other common metals used in the production of the precursors for NPG fabrication is as follows: Al about 3000 $/ton (for Al-Au alloy), Cu about 9000 $/ton (for Cu-Au alloy) and Ag is 800 $/kg for Ag-Au alloys (which is about 2000 times higher than Fe). Hence, it serves as a better option in terms of inexpensiveness and availability.

(ii) We have utilized the lowest possible concentration of Au for the precursor, i.e., 33 at. %, in accordance with the parting limit. Since it is rather common to use Au-rich precursors as reported in literature our approach is quite contrary which allows us to cut down the total cost

right from the start.

(iii) The usage of multi-metallic crystalline as well as amorphous precursors has been commonly seen in many previously reported articles. Procuring a number of metals for a single precursor (some of them being critical raw materials) only adds to the overall cost. Additionally, this can complicate the synthetic procedures requiring usually more than one dealloying process to remove the multiple less-noble metals. On the other hand, we have employed a bimetallic precursor pairing Fe with Au, knowing well that Fe is a low-cost, hugely abundant and active metal. Such approach has greatly reduced the cost and simplified our synthesis procedure while advocating the issue of sustainability at the same time.

(iv) We have not employed any critical raw material to combine with Au for the precursor alloy. Ag, a critical raw material, is a commonly used Au-pairing metal [104]. Fe, being an active, abundant and cheap metal, has been used to replace Ag giving similar or better outputs in terms of the quality and properties of the resultant NPG.

Based on all the above points the NPG samples reported in this work are outstanding, cost-effective and sustainable alternatives as an electrocatalyst for HER, MeOH-EOx as well as a SERS-active substrate.

5. Conclusion

Nanoporous Gold has been successfully obtained using a cheap and efficient $Au_{33}Fe_{67}$ precursor which was formed into ribbons by arc melting and melt-spinning techniques subsequently. It was then subjected to chemical dealloying in 1 M HNO_3 and 1 M HCl at 70 °C for different durations. The obtained NPG samples display well-defined nanoporous morphology. Few trends are noticeable, i.e., with the increase in the dealloying time, there is an increase in - (i) the atomic percentage of Au; (ii) the size of the ligaments, and; (iii) the homogeneity of the surface morphology. Among all the NPG samples obtained from 1 M HNO_3, NPG_8h was selected to be tested for its catalytic activity in HER in 0.5 M H_2SO_4 as it possessed the largest electrochemically active surface area and thus, the greatest number of active sites. The sample shows a current density of 5 mA cm^{-2} at an overpotential of -0.38 V. The obtained small Tafel slope, low onset potential and high exchange current density, i.e., 47 mV dec^{-1}, -4 mV and 0.12 mA cm^{-2} respectively, and the sample's impressive stability for more than 20 h, evidently indicate that this sample makes for an excellent candidate for HER. Besides, NPG_8h also exhibited strong SERS activity possessing a detection limit of 10^{-15} M for bipyridine. The mapping image for SERS intensity with bipyridine concentration of 10^{-12} M confirms the presence of hot spots. The electromagnetic coupling between ligaments, the localized electromagnetic fields enhanced within and around nano-sized pores and ligaments, and the confined SERS sensitive atoms can all be attributed for the strong SERS enhancement. Thus, the NPG sample also possesses excellent potential in applications related to life science and ultrasensitive instrumentation being an inexpensive and highly sensitive

SERS-active substrate. Among the NPG samples obtained from 1 M HCl, NPG_HCl_16h , with the highest active surface area, was put to test as an electrocatalyst for methanol electro-oxidation. The sample performs excellently in a basic solution of methanol and KOH demonstrating a low peak potential of -0.47 V vs Ag/AgCl along with high current density of 0.43 mA/cm^2 at the oxidation peak potential. The same sample also displays impressive stability with a minor drop in the current density and high poisoning tolerance. Overall, an easy and rapid dealloying procedure was employed using cheap, active and abundant Fe-rich precursor and avoiding the use of critical raw materials to fabricate high quality NPG samples that serve as efficient, durable, low-cost and sustainable alternative electrocatalysts for HER, MeOH-EOx as well as SERS-active substrate.

6. References:

[1] I. McCue, E. Benn, B. Gaskey, J. Erlebacher, Dealloying and Dealloyed Materials, Annu. Rev. Mater. Res. 46 (2016) 263–286. https://doi.org/10.1146/annurev-matsci-070115-031739.

[2] S. Xiao, S. Wang, X. Wang, P. Xu, Nanoporous gold: A review and potentials in biotechnological and biomedical applications, Nano Sel. 2 (2021) 1437–1458. https://doi.org/10.1002/nano.202000291.

[3] K. Mohan, N. Shahane, R. Liu, V. Smet, A. Antoniou, A Review of Nanoporous Metals in Interconnects, JOM. 70 (2018) 2192–2204. https://doi.org/10.1007/s11837-018-3081-z.

[4] F. Scaglione, P. Rizzi, F. Celegato, L. Battezzati, Synthesis of nanoporous gold by free corrosion of an amorphous precursor, J. Alloys Compd. 615 (2014) S142–S147. https://doi.org/10.1016/j.jallcom.2014.01.239.

[5] Y. Xue, F. Scaglione, P. Rizzi, L. Battezzati, High performance SERS on nanoporous gold substrates synthesized by chemical de-alloying a Au-based metallic glass, Appl. Surf. Sci. 426 (2017) 1113–1120. https://doi.org/10.1016/j.apsusc.2017.07.302.

[6] F. Scaglione, P. Rizzi, L. Battezzati, De-alloying kinetics of an Au-based amorphous alloys, J. Alloys Compd. 536 (2012) S60–S64. https://doi.org/https://doi.org/10.1016/j.jallcom.2011.11.087.

[7] P. Rizzi, F. Scaglione, L. Battezzati, Nanoporous gold by dealloying of an amorphous precursor, J. Alloys Compd. 586 (2014) S117–S120. https://doi.org/https://doi.org/10.1016/j.jallcom.2012.11.029.

[8] H.-J. Qiu, Y. Ito, M.W. Chen, Hierarchical nanoporous nickel alloy as three-dimensional electrodes for high-efficiency energy storage, Scr. Mater. 89 (2014) 69–72. https://doi.org/10.1016/j.scriptamat.2014.06.031.

[9] S. Van Petegem, S. Brandstetter, R. Maass, A.M. Hodge, B.S. El-Dasher, J. Biener, B. Schmitt, C. Borca, H. Van Swygenhoven, On the Microstructure of Nanoporous Gold:

An X-ray Diffraction Study, Nano Lett. 9 (2009) 1158–1163. https://doi.org/10.1021/nl803799q.

[10] Z. He, Y. Huang, F. He, Preparation of nanoporous molybdenum film by dealloying an immiscible Mo–Zn system for hydrogen evolution reaction, RSC Adv. 6 (2016) 15390–15393. https://doi.org/10.1039/C5RA24426A.

[11] X. Li, Q. Chen, I. McCue, J. Snyder, P. Crozier, J. Erlebacher, K. Sieradzki, Dealloying of Noble-Metal Alloy Nanoparticles, Nano Lett. 14 (2014) 2569–2577. https://doi.org/10.1021/nl500377g.

[12] F. Scaglione, Y. Xue, F. Celegato, P. Rizzi, L. Battezzati, Amorphous molybdenum sulphide @ nanoporous gold as catalyst for hydrogen evolution reaction in acidic environment, J. Mater. Sci. 53 (2018) 12388–12398. https://doi.org/10.1007/s10853-018-2490-2.

[13] S.H. Kim, Nanoporous gold: Preparation and applications to catalysis and sensors, Curr. Appl. Phys. 18 (2018) 810–818. https://doi.org/10.1016/j.cap.2018.03.021.

[14] Y. Xue, F. Scaglione, F. Celegato, P. Denis, H.-J. Fecht, P. Rizzi, L. Battezzati, Shape controlled gold nanostructures on de-alloyed nanoporous gold with excellent SERS performance, Chem. Phys. Lett. 709 (2018) 46–51. https://doi.org/https://doi.org/10.1016/j.cplett.2018.08.044.

[15] F. Scaglione, Y. Xue, F. Celegato, P. Rizzi, L. Battezzati, Amorphous molybdenum sulphide @ nanoporous gold as catalyst for hydrogen evolution reaction in acidic environment, J. Mater. Sci. 53 (2018) 12388–12398. https://doi.org/10.1007/s10853-018-2490-2.

[16] S.H. Kim, Nanoporous Gold for Energy Applications, Chem. Rec. 21 (2021) 1199–1215. https://doi.org/10.1002/tcr.202100015.

[17] The Materials Information Society, ASM Handbook Volume 3 - Alloy Phase Diagrams, ASM Handb. (1992). https://doi.org/10.1007/BF02869318.

[18] D.T.L. Alexander, D. Forrer, E. Rossi, E. Lidorikis, S. Agnoli, G.D. Bernasconi, J. Butet, O.J.F. Martin, V. Amendola, Electronic Structure-Dependent Surface Plasmon Resonance in Single Au–Fe Nanoalloys, Nano Lett. 19 (2019) 5754–5761. https://doi.org/10.1021/acs.nanolett.9b02396.

[19] E. Bosco, P. Rizzi, M. Baricco, Rapid solidification of immiscible alloys, J. Magn. Magn. Mater. 262 (2003) 64–68. https://doi.org/10.1016/S0304-8853(03)00020-9.

[20] E. Bosco, P. Rizzi, M. Baricco, Phase transformations in Au-Fe melt spun alloys, Mater. Sci. Eng. A. 375–377 (2004) 468–472. https://doi.org/10.1016/j.msea.2003.10.048.

[21] F. Scaglione, A. Gebert, L. Battezzati, Dealloying of an Au-based amorphous alloy, Intermetallics. 18 (2010) 2338–2342. https://doi.org/10.1016/j.intermet.2010.08.005.

[22] Y. Xue, F. Scaglione, P. Rizzi, L. Battezzati, Improving the chemical de-alloying of amorphous Au alloys, Corros. Sci. 127 (2017) 141–146. https://doi.org/10.1016/j.corsci.2017.08.026.

[23] F. Scaglione, Y. Xue, F. Celegato, P. Rizzi, L. Battezzati, Amorphous molybdenum sulphide @ nanoporous gold as catalyst for hydrogen evolution reaction in acidic environment, J. Mater. Sci. 53 (2018) 12388–12398. https://doi.org/10.1007/s10853-018-2490-2.

[24] F. Scaglione, F. Celegato, P. Rizzi, L. Battezzati, A comparison of de-alloying crystalline and amorphous multicomponent Au alloys, Intermetallics. 66 (2015) 82–87. https://doi.org/https://doi.org/10.1016/j.intermet.2015.06.022.

[25] F. Scaglione, P. Rizzi, F. Celegato, L. Battezzati, Synthesis of nanoporous gold by free corrosion of an amorphous precursor, J. Alloys Compd. 615 (2014) S142–S147. https://doi.org/10.1016/j.jallcom.2014.01.239.

[26] Y. Xue, F. Scaglione, P. Rizzi, L. Battezzati, P. Denis, H.-J. Fecht, Electrodeposited platinum on de-alloyed nanoporous gold with enhanced electro-catalytic performance, Appl. Surf. Sci. 476 (2019) 412–417. https://doi.org/10.1016/j.apsusc.2019.01.099.

[27] Y. Xue, F. Scaglione, E.M. Paschalidou, P. Rizzi, L. Battezzati, Excellent surface enhanced Raman scattering obtained with nanoporous gold fabricated by chemical de-alloying, Chem. Phys. Lett. 665 (2016) 6–9. https://doi.org/10.1016/j.cplett.2016.10.046.

[28] A. Otto, The ‘chemical’ (electronic) contribution to surface-enhanced Raman scattering, J. Raman Spectrosc. 36 (2005) 497–509. https://doi.org/10.1002/jrs.1355.

[29] S.-Y. Ding, E.-M. You, Z.-Q. Tian, M. Moskovits, Electromagnetic theories of surface-enhanced Raman spectroscopy, Chem. Soc. Rev. 46 (2017) 4042–4076. https://doi.org/10.1039/C7CS00238F.

[30] E. Massarini, P. Wästerby, L. Landström, C. Lejon, O. Beck, P.O. Andersson, Methodologies for assessment of limit of detection and limit of identification using surface-enhanced Raman spectroscopy, Sensors Actuators, B Chem. 207 (2015) 437–446. https://doi.org/10.1016/j.snb.2014.09.116.

[31] N.P.W. Pieczonka, R.F. Aroca, Single molecule analysis by surfaced-enhanced Raman scattering, Chem. Soc. Rev. 37 (2008) 946. https://doi.org/10.1039/b709739p.

[32] L. Zhang, H. Liu, L. Chen, P. Guan, B. Chen, T. Fujita, Y. Yamaguchi, H. Iwasaki, Q.-K. Xue, M. Chen, Large-scale growth of sharp gold nano-cones for single-molecule SERS detection, RSC Adv. 6 (2016) 2882–2887. https://doi.org/10.1039/C5RA22321K.

[33] Y. Jiao, J.D. Ryckman, P.N. Ciesielski, C.A. Escobar, G.K. Jennings, S.M. Weiss, Patterned nanoporous gold as an effective SERS template, Nanotechnology. 22 (2011) 295302. https://doi.org/10.1088/0957-4484/22/29/295302.

[34] F. Scaglione, E.M. Paschalidou, P. Rizzi, S. Bordiga, L. Battezzati, Nanoporous gold obtained from a metallic glass precursor used as substrate for surface-enhanced Raman scattering, Philos. Mag. Lett. 95 (2015) 474–482. https://doi.org/10.1080/09500839.2015.1093665.

[35] L.H. Qian, X.Q. Yan, T. Fujita, A. Inoue, M.W. Chen, Surface enhanced Raman scattering of nanoporous gold: Smaller pore sizes stronger enhancements, Appl. Phys.

Lett. 90 (2007) 153120. https://doi.org/10.1063/1.2722199.

[36] P.A. Alaba, C.S. Lee, F. Abnisa, M.K. Aroua, P. Cognet, Y. Pérès, W.M.A. Wan Daud, A review of recent progress on electrocatalysts toward efficient glycerol electrooxidation, Rev. Chem. Eng. 36 (2020) 1–34. https://doi.org/10.1515/revce-2019-0013.

[37] M.S.E. Houache, E. Cossar, S. Ntais, E.A. Baranova, Electrochemical modification of nickel surfaces for efficient glycerol electrooxidation, J. Power Sources. (2018). https://doi.org/10.1016/j.jpowsour.2017.08.089.

[38] J.A. Cruz-Navarro, L.H. Mendoza-Huizar, V. Salazar-Pereda, J.Á. Cobos-Murcia, R. Colorado-Peralta, G.A. Álvarez-Romero, Progress in the use of electrodes modified with coordination compounds for methanol electro-oxidation, Inorganica Chim. Acta. 520 (2021) 120293. https://doi.org/10.1016/j.ica.2021.120293.

[39] M. Valter, B. Wickman, A. Hellman, Solvent Effects for Methanol Electrooxidation on Gold, J. Phys. Chem. C. 125 (2021) 1355–1360. https://doi.org/10.1021/acs.jpcc.0c08923.

[40] Y. Kang, Q. Xue, P. Jin, J. Jiang, J. Zeng, Y. Chen, Rhodium Nanosheets–Reduced Graphene Oxide Hybrids: A Highly Active Platinum-Alternative Electrocatalyst for the Methanol Oxidation Reaction in Alkaline Media, ACS Sustain. Chem. Eng. 5 (2017) 10156–10162. https://doi.org/10.1021/acssuschemeng.7b02163.

[41] P. Krawczyk, T. Rozmanowski, M. Frankowski, Methanol Electrooxidation at Electrodes Made of Exfoliated Graphite/Nickel/Palladium Composite, Catal. Letters. 149 (2019) 2307–2316. https://doi.org/10.1007/s10562-019-02785-9.

[42] G.A. Tritsaris, J. Rossmeisl, Methanol oxidation on model elemental and bimetallic transition metal surfaces, J. Phys. Chem. C. (2012). https://doi.org/10.1021/jp209506d.

[43] F. Peng, C. Zhou, H. Wang, H. Yu, J. Liang, J. Yang, The role of RuO2 in the electrocatalytic oxidation of methanol for direct methanol fuel cell, Catal. Commun. 10 (2009) 533–537. https://doi.org/https://doi.org/10.1016/j.catcom.2008.10.037.

[44] S.A.S. Machado, L.A. Avaca, The hydrogen evolution reaction on nickel surfaces stabilized by H-absorption, Electrochim. Acta. 39 (1994) 1385–1391. https://doi.org/10.1016/0013-4686(94)E0003-I.

[45] S.H. Ahn, S.J. Hwang, S.J. Yoo, I. Choi, H.-J. Kim, J.H. Jang, S.W. Nam, T.-H. Lim, T. Lim, S.-K. Kim, J.J. Kim, Electrodeposited Ni dendrites with high activity and durability for hydrogen evolution reaction in alkaline water electrolysis, J. Mater. Chem. 22 (2012) 15153–15159. https://doi.org/10.1039/C2JM31439H.

[46] H. Ogihara, M. Fujii, T. Saji, Hydrogen evolution reaction (HER) over electroless-deposited nickel nanospike arrays, RSC Adv. 4 (2014) 58660–58663. https://doi.org/10.1039/C4RA11646A.

[47] H. Lukas, S.G. Fries, B. Sundman, Computational Thermodynamics, Cambridge University Press, Cambridge, 2007. https://doi.org/10.1017/CBO9780511804137.

[48] Thermo-Calc Software, (n.d.). https://thermocalc.com/ (accessed June 14, 2021).

[49] P.A. Beck, H. Okamoto, T.B. Massalski, L.J. Swartzendruber, Phase Diagrams of Binary Iron Alloys, in: American Society for Metals, Metals Park, OH, 1993.

[50] D. Favez, J.D. Wagnière, M. Rappaz, Au-Fe alloy solidification and solid-state transformations, Acta Mater. 58 (2010) 1016–1025. https://doi.org/10.1016/j.actamat.2009.10.017.

[51] M. Palumbo, L. Battezzati, Thermodynamics and kinetics of metallic amorphous phases in the framework of the CALPHAD approach, Calphad. 32 (2008) 295–314. https://doi.org/10.1016/j.calphad.2007.12.002.

[52] P.S.M. Kumar, T. Sivakumar, T. Fujita, R. Jayavel, H. Abe, Synthesis of metastable Au-Fe alloy using ordered nanoporous silica as a hard template, Metals (Basel). 8 (2018) 1–7. https://doi.org/10.3390/met8010017.

[53] J. van der Zalm, S. Chen, W. Huang, A. Chen, Review—Recent Advances in the Development of Nanoporous Au for Sensing Applications, J. Electrochem. Soc. 167 (2020) 037532. https://doi.org/10.1149/1945-7111/ab64c0.

[54] A. Sukeri, M. Bertotti, Nanoporous gold surface: An efficient platform for hydrogen evolution reaction at very low overpotential, J. Braz. Chem. Soc. 29 (2018) 226–231. https://doi.org/10.21577/0103-5053.20170132.

[55] C. Yang, M.Y. Gao, Q.B. Zhang, J.R. Zeng, X.T. Li, A.P. Abbott, In-situ activation of self-supported 3D hierarchically porous Ni3S2 films grown on nanoporous copper as excellent pH-universal electrocatalysts for hydrogen evolution reaction, Nano Energy. 36 (2017) 85–94. https://doi.org/10.1016/j.nanoen.2017.04.032.

[56] L. Yang, Y. Lv, D. Cao, Co,N-codoped nanotube/graphene 1D/2D heterostructure for efficient oxygen reduction and hydrogen evolution reactions, J. Mater. Chem. A. 6 (2018) 3926–3932. https://doi.org/10.1039/C7TA11140A.

[57] N. Prabu, T. Kesavan, G. Maduraiveeran, M. Sasidharan, Bio-derived nanoporous activated carbon sheets as electrocatalyst for enhanced electrochemical water splitting, Int. J. Hydrogen Energy. 44 (2019) 19995–20006. https://doi.org/10.1016/j.ijhydene.2019.06.016.

[58] R.D. Nikam, A.-Y. Lu, P.A. Sonawane, U.R. Kumar, K. Yadav, L.-J. Li, Y.-T. Chen, Three-Dimensional Heterostructures of MoS 2 Nanosheets on Conducting MoO 2 as an Efficient Electrocatalyst To Enhance Hydrogen Evolution Reaction, ACS Appl. Mater. Interfaces. 7 (2015) 23328–23335. https://doi.org/10.1021/acsami.5b07960.

[59] X. Xiao, C. Engelbrekt, M. Zhang, Z. Li, J. Ulstrup, J. Zhang, P. Si, A straight forward approach to electrodeposit tungsten disulfide/poly(3,4-ethylenedioxythiophene) composites onto nanoporous gold for the hydrogen evolution reaction, Appl. Surf. Sci. 410 (2017) 308–314. https://doi.org/https://doi.org/10.1016/j.apsusc.2017.03.130.

[60] Q. Tang, D. Jiang, Mechanism of Hydrogen Evolution Reaction on 1T-MoS2 from First Principles, ACS Catal. 6 (2016) 4953–4961. https://doi.org/10.1021/acscatal.6b01211.

[61] A.S. Bin Mohd Najib, M. Iqbal, M.B. Zakaria, S. Shoji, Y. Cho, X. Peng, S. Ueda, A. Hashimoto, T. Fujita, M. Miyauchi, Y. Yamauchi, H. Abe, Active faceted nanoporous

ruthenium for electrocatalytic hydrogen evolution, J. Mater. Chem. A. 8 (2020) 19788–19792. https://doi.org/10.1039/D0TA04223D.

[62] J. Zhang, X. Wang, Y. Xue, Z. Xu, J. Pei, Z. Zhuang, Self-Assembly Precursor-Derived MoP Supported on N,P-Codoped Reduced Graphene Oxides as Efficient Catalysts for Hydrogen Evolution Reaction, Inorg. Chem. 57 (2018) 13859–13865. https://doi.org/10.1021/acs.inorgchem.8b02359.

[63] X. Xiao, C. Engelbrekt, Z. Li, P. Si, Hydrogen evolution at nanoporous gold/tungsten sulfide composite film and its optimization, Electrochim. Acta. 173 (2015) 393–398. https://doi.org/10.1016/j.electacta.2015.05.048.

[64] F. Barbir, Fuel Cell Electrochemistry, in: F.B.T.-P.E.M.F.C. (Second E. Barbir (Ed.), PEM Fuel Cells, Elsevier, Boston, 2013: pp. 33–72. https://doi.org/10.1016/B978-0-12-387710-9.00003-5.

[65] A. Abbaspour, F. Norouz-Sarvestani, High electrocatalytic effect of Au-Pd alloy nanoparticles electrodeposited on microwave assisted sol-gel-derived carbon ceramic electrode for hydrogen evolution reaction, Int. J. Hydrogen Energy. 38 (2013) 1883–1891. https://doi.org/10.1016/j.ijhydene.2012.11.096.

[66] T.-H. Lu, C.-J. Chen, M. Basu, C.-G. Ma, R.-S. Liu, The CoTe 2 nanostructure: an efficient and robust catalyst for hydrogen evolution, Chem. Commun. 51 (2015) 17012–17015. https://doi.org/10.1039/C5CC06806A.

[67] W. Li, X. Wang, D. Xiong, L. Liu, Efficient and durable electrochemical hydrogen evolution using cocoon-like MoS2 with preferentially exposed edges, Int. J. Hydrogen Energy. 41 (2016) 9344–9354. https://doi.org/10.1016/j.ijhydene.2016.03.209.

[68] L. Chen, S. Yang, K. Qian, W. Wei, C. Sun, J. Xie, In situ growth of N-doped carbon coated CoNi alloy with graphene decoration for enhanced HER performance, J. Energy Chem. 29 (2019) 129–135. https://doi.org/10.1016/j.jechem.2018.03.005.

[69] F.-X. Ma, H. Bin Wu, B.Y. Xia, C.-Y. Xu, X.W.D. Lou, Hierarchical β-Mo 2 C Nanotubes Organized by Ultrathin Nanosheets as a Highly Efficient Electrocatalyst for Hydrogen Production, Angew. Chemie Int. Ed. 54 (2015) 15395–15399. https://doi.org/10.1002/anie.201508715.

[70] B. Pierozynski, Hydrogen evolution reaction at Pd-modified carbon fibre and nickel-coated carbon fibre materials, Int. J. Hydrogen Energy. 38 (2013) 7733–7740. https://doi.org/10.1016/j.ijhydene.2013.04.092.

[71] B. Pierozynski, T. Mikolajczyk, M. Turemko, E. Czerwosz, M. Kozlowski, Hydrogen evolution reaction at Pd-modified carbon fibre in 0.1 M NaOH, Int. J. Hydrogen Energy. 40 (2015) 1795–1799. https://doi.org/10.1016/j.ijhydene.2014.12.029.

[72] J.M. Gonçalves, A. Kumar, M.I. da Silva, H.E. Toma, P.R. Martins, K. Araki, M. Bertotti, L. Angnes, Nanoporous Gold-Based Materials for Electrochemical Energy Storage and Conversion, Energy Technol. 9 (2021) 2000927. https://doi.org/10.1002/ente.202000927.

[73] A. Wittstock, A. Wichmann, J. Biener, M. Bäumer, Nanoporous gold: a new gold catalyst with tunable properties, Faraday Discuss. 152 (2011) 87.

https://doi.org/10.1039/c1fd00022e.

[74] Y. Cao, J. Zhang, Y. Yang, Z. Huang, N.V. Long, C. Fu, Engineering of SERS Substrates Based on Noble Metal Nanomaterials for Chemical and Biomedical Applications, Appl. Spectrosc. Rev. 50 (2015) 499–525. https://doi.org/10.1080/05704928.2014.923901.

[75] M. Moskovits, Surface-enhanced spectroscopy, Rev. Mod. Phys. 57 (1985) 783–826. https://doi.org/10.1103/RevModPhys.57.783.

[76] S.O. Kucheyev, J.R. Hayes, J. Biener, T. Huser, C.E. Talley, A. V. Hamza, Surface-enhanced Raman scattering on nanoporous Au, Appl. Phys. Lett. 89 (2006) 053102. https://doi.org/10.1063/1.2260828.

[77] V. Amendola, S. Scaramuzza, L. Litti, M. Meneghetti, G. Zuccolotto, A. Rosato, E. Nicolato, P. Marzola, G. Fracasso, C. Anselmi, M. Pinto, M. Colombatti, Magneto-plasmonic Au-Fe alloy nanoparticles designed for multimodal SERS-MRI-CT imaging, Small. 10 (2014) 2476–2486. https://doi.org/10.1002/smll.201303372.

[78] X.Y. Lang, P.F. Guan, L. Zhang, T. Fujita, M.W. Chen, Characteristic Length and Temperature Dependence of Surface Enhanced Raman Scattering of Nanoporous Gold, J. Phys. Chem. C. 113 (2009) 10956–10961. https://doi.org/10.1021/jp903137n.

[79] A. Chauvin, M. Lafuente, J.Y. Mevellec, R. Mallada, B. Humbert, M.P. Pina, P.-Y. Tessier, A. El Mel, Lamellar nanoporous gold thin films with tunable porosity for ultrasensitive SERS detection in liquid and gas phase, Nanoscale. 12 (2020) 12602–12612. https://doi.org/10.1039/D0NR01721C.

[80] E.M. Paschalidou, F. Scaglione, A. Gebert, S. Oswald, P. Rizzi, L. Battezzati, Partially and fully de-alloyed glassy ribbons based on Au: Application in methanol electro-oxidation studies, J. Alloys Compd. 667 (2016) 302–309. https://doi.org/10.1016/j.jallcom.2016.01.181.

[81] E.M. Paschalidou, F. Scaglione, A. Gebert, S. Oswald, P. Rizzi, L. Battezzati, Partially and fully de-alloyed glassy ribbons based on Au: Application in methanol electro-oxidation studies, J. Alloys Compd. 667 (2016) 302–309. https://doi.org/10.1016/j.jallcom.2016.01.181.

[82] W. Yuan, Y. Zhang, N. Zhang, C. Yin, X. Zhang, X. Liu, Carbon riveted Pt-MnO2/reduced graphene oxide anode catalyst for DMFC, Catal. Commun. 100 (2017) 66–70. https://doi.org/https://doi.org/10.1016/j.catcom.2017.06.030.

[83] J.P.J. de Oliveira, A.C. de Sá, L.L. Paim, Electrocatalysis of Ethanol and Methanol Electrooxidation by Composite Electrodes with NiOOH/FeOOH Supported on Reduced Graphene Oxide onto Composite Electrodes, Chem. Proc. . 2 (2020). https://doi.org/10.3390/ECCS2020-07523.

[84] R. Abdullah Mirzaie, A. Eshghi, Study of methanol electro-oxidation on Ni and Ni–Pt/carbon paper electrodes for direct methanol fuel cell applications, Surf. Eng. 30 (2014) 263–267. https://doi.org/10.1179/1743294414Y.0000000248.

[85] S. Chen, H. Wu, J. Tao, H. Xin, Y. Zhu, J. Chen, Pt–Ni Seed-Core-Frame Hierarchical Nanostructures and Their Conversion to Nanoframes for Enhanced Methanol Electro-

Oxidation, Catal. . 9 (2019). https://doi.org/10.3390/catal9010039.

[86] P. Yang, Z. Zhou, T. Zheng, C. Gu, X. Gong, Y. Zhang, Y. Xie, N. Yang, J. Fei, A novel strategy to synthesize Pt/CNTs nanocatalyst with highly improved activity for methanol electrooxidation, J. Electroanal. Chem. 897 (2021) 115557. https://doi.org/https://doi.org/10.1016/j.jelechem.2021.115557.

[87] J. Shu, R. Li, Z. Lian, W. Zhang, R. Jin, H. Yang, S. Li, In-situ oxidation of Palladium–Iridium nanoalloy anchored on Nitrogen-doped graphene as an efficient catalyst for methanol electrooxidation, J. Colloid Interface Sci. 605 (2022) 44–53. https://doi.org/https://doi.org/10.1016/j.jcis.2021.07.056.

[88] G.M. Thorat, H.S. Jadhav, J.G. Seo, Bi-functionality of mesostructured MnCo2O4 microspheres for supercapacitor and methanol electro-oxidation, Ceram. Int. 43 (2017) 2670–2679. https://doi.org/https://doi.org/10.1016/j.ceramint.2016.11.081.

[89] A. Rebekah, S. Anantharaj, C. Viswanthan, N. Ponpandian, Zn-substituted MnCo2O4 nanostructure anchored over rGO for boosting the electrocatalytic performance towards methanol oxidation and oxygen evolution reaction (OER), Int. J. Hydrogen Energy. 45 (2020) 14713–14727. https://doi.org/https://doi.org/10.1016/j.ijhydene.2020.03.231.

[90] J. Zheng, K. Huang, G. Hou, H. Zhang, H. Cao, A highly active Pt nanocatalysts supported on RuO2 modified TiO2-NTs for methanol electrooxidation with excellent CO tolerance, Int. J. Hydrogen Energy. 44 (2019) 31506–31514. https://doi.org/https://doi.org/10.1016/j.ijhydene.2019.10.048.

[91] E.A. Şahin, R. Solmaz, Methanol electrooxidation activity of binary CoAg electrocatalyst, Int. J. Hydrogen Energy. 45 (2020) 35013–35022. https://doi.org/https://doi.org/10.1016/j.ijhydene.2020.08.125.

[92] M.B. Askari, S.M. Rozati, P. Salarizadeh, H. Saeidfirozeh, A. Di Bartolomeo, A remarkable three-component RuO2-MnCo2O4/rGO nanocatalyst towards methanol electrooxidation, Int. J. Hydrogen Energy. (2021). https://doi.org/https://doi.org/10.1016/j.ijhydene.2021.08.207.

[93] M.A. Kamyabi, K. Ebrahimi Qaratapeh, S. Jadali, M. Moharramnezhad, Decorating the carbon felt electrode with polymeric platinize nanocomposite: characterization and electrocatalytic activity towards methanol oxidation reaction, J. Chem. Sci. 131 (2019) 61. https://doi.org/10.1007/s12039-019-1640-7.

[94] J.B. Raoof, N. Azizi, R. Ojani, S. Ghodrati, M. Abrishamkar, F. Chekin, Synthesis of ZSM-5 zeolite: Electrochemical behavior of carbon paste electrode modified with Ni (II)-zeolite and its application for electrocatalytic oxidation of methanol, Int. J. Hydrogen Energy. 36 (2011) 13295–13300. https://doi.org/10.1016/j.ijhydene.2010.06.055.

[95] Z. Mojović, T. Mudrinić, A. Rabi-Stankovic, A. Ivanovic-Sasic, S. Marinovic, M. Žunić, D. Jovanović, Methanol Electrooxidation on PtRu Modified Zeolite X, Sci. Sinter. 45 (2013) 89–96. https://doi.org/10.2298/SOS1301089M.

[96] M.F.R. Hanifah, J. Jaafar, M.H.D. Othman, A.F. Ismail, M.A. Rahman, N. Yusof, W.N.W. Salleh, F. Aziz, A.Z. Abdul Ajid, Advanced ternary RGO/bimetallic Pt-Pd

alloy/CeO2 nanocomposite electrocatalyst by one-step hydrothermal-assisted formic acid reduction reaction for methanol electrooxidation, J. Environ. Chem. Eng. 9 (2021) 104991. https://doi.org/https://doi.org/10.1016/j.jece.2020.104991.

[97] Q. Zhou, J. Wu, Z. Pan, X. Kong, Z. Cui, D. Wu, G. Hu, Pt supported on boron, nitrogen co-doped carbon nanotubes (BNC NTs) for effective methanol electrooxidation, Int. J. Hydrogen Energy. 45 (2020) 33634–33640. https://doi.org/10.1016/j.ijhydene.2020.09.056.

[98] S. Shahrokhian, S. Rezaee, Vertically standing Cu2O nanosheets promoted flower-like PtPd nanostructures supported on reduced graphene oxide for methanol electro-oxidation, Electrochim. Acta. (2018). https://doi.org/10.1016/j.electacta.2017.10.141.

[99] Z. Chai, C. Zhang, H. Wang, X. Bi, P. Bai, X. Wang, Increased interface effects of Pt–Fe alloy/CeO2/C with Pt–Fe selective loading on CeO2 for superior performance in direct methanol fuel cell, Int. J. Hydrogen Energy. (2019). https://doi.org/10.1016/j.ijhydene.2019.01.016.

[100] Y. Hao, X. Wang, Y. Zheng, J. Shen, J. Yuan, A.J. Wang, L. Niu, S. Huang, Uniform Pt Nanoparticles Incorporated into Reduced Graphene Oxides with MoO3 as Advanced Anode Catalysts for Methanol Electro-oxidation, Electrochim. Acta. (2016). https://doi.org/10.1016/j.electacta.2016.03.054.

[101] T.H.T. Vu, T.T.T. Tran, H.N.T. Le, L.T. Tran, P.H.T. Nguyen, H.T. Nguyen, N.Q. Bui, Solvothermal synthesis of Pt -SiO2/graphene nanocomposites as efficient electrocatalyst for methanol oxidation, Electrochim. Acta. (2015). https://doi.org/10.1016/j.electacta.2015.02.100.

[102] Q. Sun, S.J. Park, S. Kim, Preparation and electrocatalytic oxidation performance of Pt/MnO2-graphene oxide nanocomposites, J. Ind. Eng. Chem. (2015). https://doi.org/10.1016/j.jiec.2014.12.002.

[103] The LONDON METAL EXCHANGE The world centre for industrial metals trading, (n.d.). https://www.lme.com/.

[104] G.A. Blengini, C.E.L. Latunussa, U. Eynard, C. Torres de Matos, D. Wittmer, K. Georgitzikis, C. Pavel, S. Carrara, L. Mancini, M. Unguru, D. Blagoeva, F. Mathieux, D. Pennington, Study on the EU's list of Critical Raw Materials (2020) Final Report, 2020. https://doi.org/10.2873/904613.

Chapter V

FePd NANOWIRES

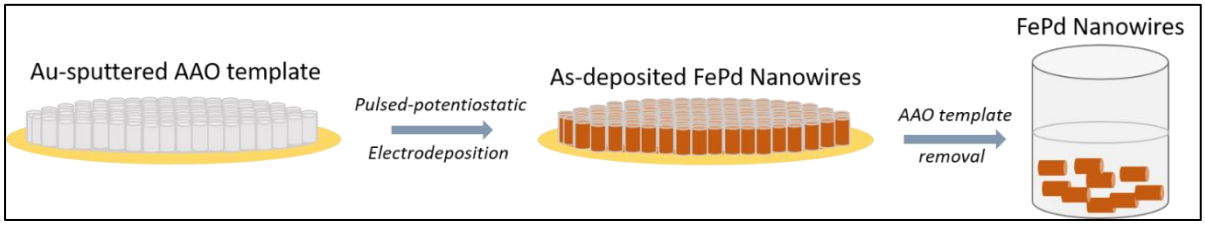

1. Introduction

Metallic nanostructures hold promising potential for applications in different fields such as microactuators, magnetic materials, catalysis etc.[1] Besides, mesoporous metallic nanostructures have been increasingly showcasing their capability in abundance of applications including information technologies, energy conversion, sensing, etc. owing to their porous architecture (pore sizes in the range of 2 nm to 50 nm), high thermal and electrical conductance and other interesting properties.[2] In the same thread, dense and mesoporous nanowires possess an array of applications credited to their elongated shape and anisotropic physical and magnetic properties such as in biomedicine,[3] biotechnology, ultrahigh-density magnetic storage, storage media applications and microelectromechanical system (MEMS).[4] Specifically, bimetallic alloys with a magnetic transition element (Fe, Co, Ni) have garnered immense attention for their multifaceted nature. [5,6] FePd, being one such bimetallic alloy, holds excellent promise where properties of the transition metal (Fe) merge with that of the noble metal (Pd).[7–9] The intrinsic magnetic properties of Fe can be easily exploited in an FePd alloy. This alloy also possesses enhanced catalytic efficiency among other applicatory capabilities. [10] There have been numerous applications displayed by FePd alloys, e.g. hydrogen separation, environmental remediation, membrane hydrogenation reactions, sensors and actuators,[11] magnetic drug delivery,[3] and catalysis.[12,13] They have also garnered extensive attention attributed to their extraordinary magnetostrictive and shape memory effects.[14] Besides, FePd alloy can be dealloyed by readily dissolving Fe leading to formation of a nanostructured Pd-rich material with its own unique properties (such as large surface area to volume ratio).[6,15]

For fabrication of nanowires electrodeposition within nanoporous templates is an impressively proficient method.[11] Not only it is a cost-effective and high throughput synthesis technique, but it also allows for fine-tuning of the attributes of the target sample such as chemical composition, physical and mechanical properties, by simply and conveniently altering the deposition parameters.[16,17] For co-depositing two metals their

respective reduction potentials should be (nearly) the same.[1] But that is not the case for co-depositing Fe and Pd as both have a large difference in their reduction potentials which makes it challenging. Thus, the FePd electrodeposition essentially requires a suitable complexing agent that would shift the reduction potential of Pd towards the less-noble Fe while keeping the electrolyte chemically stable.[1,18,19] Also, hydrogen evolution takes place during the process as a side reaction.[11] The generated gas bubbles might block the pores and thus interrupt the metal deposition.[11] So, to avoid this from happening pulse technique is employed which has been shown to minimize the blockage of pores.[11] Furthermore, the formation of a high number of OH^- ions within the pores as a result of hydrogen evolution leads to facile precipitation of hydroxides, in particular $Fe(OH)_3$.[11] To prevent this 5-sulfosalicylic acid is added which forms a stable Fe^{3+} complex precluding hydroxide formation.[11] The pulse plating technique also decreases the occurrence of concentration gradients and keeps the pH constant. During the off-time no metal deposition takes place. This allows for balancing of concentration gradients of metal ions as well as the rise of hydrogen bubbles. [20]

When it comes to the synthesis of mesoporous metallic nanostructures typical processes include soft-templating, hard-templating and solution-phase approaches.[2] Specifically, soft templates such as micelle assemblies have come to forefront in the last years. Micelle assemblies were first brought to light by Yamauchi and co-workers for the electrodeposition of Pt metal from diluted (1.0 wt. %) non-ionic surfactant solutions. [2] This procedure has been extended to bimetallic systems as well. [2] Among all soft-templating methods, electrochemical deposition is the most suitable and straight-forward technique to reduce the metal ions in a solution.[2] So far, commercial P-123 and F-127 Pluronics have been used as common non-ionic surfactant assemblies above their critical micelle concentration (cmc). [2] P-123 forms micelles in water above its cmc, with the core made of poly(propylene oxide) (PPO) block and the shell of poly(ethylene oxide) (PEO) units. During the electrodeposition process P-123 micelle assemblies gather spontaneously at the solid–liquid interface, Pd(II) species coordinate to the shell of these micelle self-assemblies. [11] In this way, porosity can be generated in the electrodeposited NWs which is critically dependent on the extent and strength of this coordination. [11]

In the present paper we have reported successful fabrication of a series of dense and mesoporous FePd nanowires with different composition and diameters. The structural evolution and magnetic properties of the obtained nanowires have been investigated.

2. Experimental

The FePd NWs with varying compositions and diameters, both dense and mesoporous, were fabricated by pulsed potentiostatic template-assisted electrodeposition. Commercial Anodisc 25 (Whatman) were used as the Anodised Aluminium Oxide (AAO) template discs with a diameter of 25 mm, membrane thickness of 60 μm and average pore sizes of 20 nm, 100 nm

and 200 nm. Additionally, commercially available Polycarbonate (PC) templates of pore size 30, 50 and 100 nm were used. These membranes act as hard templates with a hexagonal assortment of pores. A 30 nm thick Au layer was sputter-deposited onto the backside of the membranes using an AJA international sputtering system under argon atmosphere to provide electrical contact and serve as working electrodes for electrodeposition.

In order to synthesize the FePd NWs, an aqueous electrolyte containing 0.01 M Tetraamminepalladium(II) chloride $Pd(NH_3)_4Cl_2$, 0.05 M Iron*(III) sulfate* hydrate $Fe_2(SO_4)_3xH_2O$, 0.06 M 5-Sulfosalicylic acid dihydrate (SSA) $C_7H_6O_6S.2H_2O$, and 0.3 M Ammonium sulfate $(NH_4)_2SO_4$ was used. This electrolyte will be referred to as the FePd electrolyte in the future mentions.

For preparation of mesoporous NWs, a micelle-forming surfactant was added to the aqueous FePd electrolyte, i.e., P123 triblock co-polymer which induces porosity by its micellar action. First, it was dissolved in the $Pd(NH_3)_4Cl_2$ (1:1 ratio, e.g. 15 mg P123 in 15 mL $Pd(NH_3)_4Cl_2$) and stirred at room temperature for two days. Afterwards, when P123 was completely dissolved, 0.05 M $Fe_2(SO_4)_3xH_2O$, 0.06 M SSA and 0.3 M $(NH_4)_2SO_4$ were added to this ($Pd(NH_3)_4Cl_2$ + P123) aqueous solution. This electrolyte will be referred to as FePd+P123 in the following mentions. The pH of both the aqueous electrolytes was adjusted to 5 for all experiments using ammonium hydroxide. All the solutions were prepared from reagents grade chemicals and de-ionized water.

All the electrodeposition experiments were carried out at room temperature without stirring the solution. A typical three-electrode setup was used - a Pt spiral as counter electrode and a saturated Ag/AgCl reference electrode. All electrode potentials are in reference to the potential of the Ag/AgCl electrode. Electrodeposition was carried out in pulsed potential mode using PGSTAT302N Autolab potentiostat/galvanostat (Metrohm-Autolab). Two alternating potential steps were applied - the deposition potential E_{on} and the resting potential E_{off}. The duration for which E_{on} was applied is termed here as t_{on} which was set at 30 s while that for E_{off} is t_{off} at 90 s. The whole electrodeposition was repeated 60 times for 2 h. Here, E_{on} was varied from -1.05 V to -1.3 V to obtain NWs with different compositions while E_{off} was kept constant at -0.46 V vs Ag/AgCl. All the NW samples were prepared following the above-mentioned deposition parameters. A representative schematic diagram of pulsed potentiostatic electrodeposition is given in Figure 1. All electrodeposited samples were repeatedly rinsed with de-ionized water immediately after being removed from the electrolyte. To obtain NWs, AAO template was dissolved in 10 % w/w NaOH solution at 80 °C for 10 minutes while PC template was dissolved in $CHCl_3$ at room temperature for a few minutes. The supernatant was then removed and the freed nanowires were kept dispersed in ethanol and sonicated for few minutes.

The evolution of the morphology and the stoichiometry was studied via a Zeiss Merlin field-emission scanning electron microscopy (FESEM) equipped with an energy dispersive X-ray spectrometer (EDS) and a JEOL JEM-2011 High resolution transmission electron microscope (HRTEM). The structure of the samples was examined with a Panalytical X-pert X-ray

Diffractometer in Bragg–Brentano geometry with monochromatic Cu K radiation. Room-temperature magnetic measurements were performed using a vibrating sample magnetometer (VSM) operating with an applied magnetic field (H) in the range ±15 kOe. The hysteresis curves were obtained by applying H along the direction parallel (PA) and perpendicular (PE) to the major axis of the nanowires.

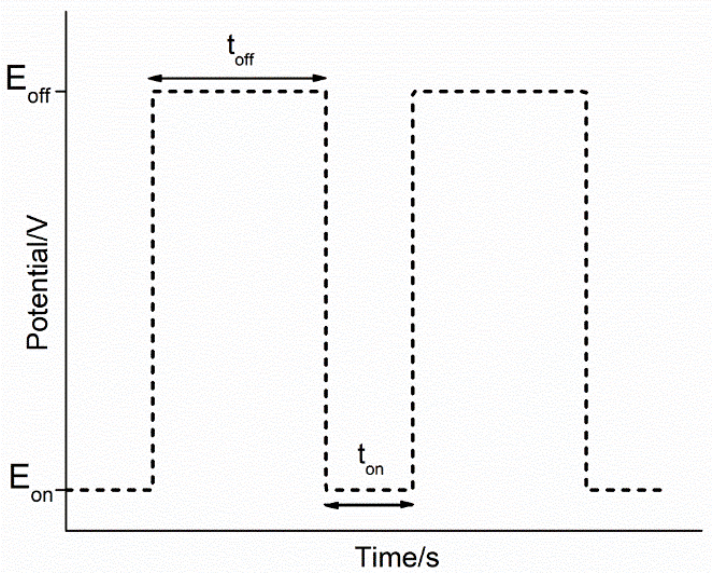

Figure 1. Pulsed potentiostatic electrodeposition scheme: during t_{on}, the potential E_{on} is applied at the selected deposition sites; during t_{off}, the electrodes are brought back to the initial open-circuit potential E_{off}.

3. Results and Discussion

3.1. Dense nanowires

Dense and long NWs of different diameters and compositions have been prepared using the FePd electrolyte with varying deposition potentials. The samples have been named throughout the section following this syntax: 'type of membrane_pore size_deposition potential'. The morphology of the NWs was observed by FESEM. First, the templates were dissolved using aqueous solution of NaOH, then washed several times in distilled water. After washing the NWs were dispersed in ethanol and sonicated for few minutes. To observe them under FESEM, a small blob of ethanol containing the dispersed NWs was dropped onto the carbon tape covering a FESEM stub. Figure 2 exhibits the FESEM images of dense NWs obtained from electrodepositing at -1.2 V vs Ag/AgCl over Au sputtered-AAO membranes of pore sizes 20 and 100 nm. In Figure 2 (a) an array of NWs of AAO_20_-1.2 V attached to the Au layer can be observed. They are continuous with slightly different lengths, longest being 4.7 µm. The mean diameter is calculated to be 157 nm with standard deviation of 22 nm. As evidenced in Figure 2 (b), a magnified look at a single NW proves that these NWs are clearly

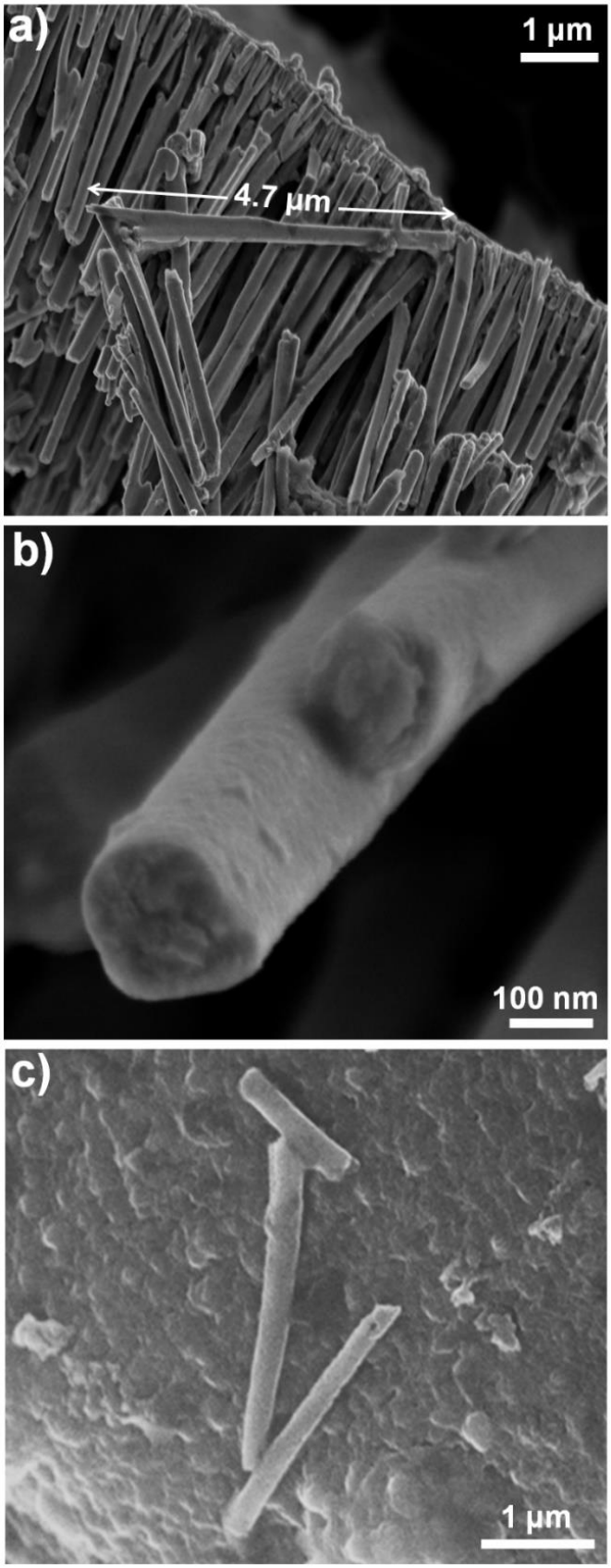

Figure 2. FESEM images of (a) AAO_20_-1.2V; (b) AAO_20_-1.2V at higher magnification; and (c) AAO_100_-1.2V

dense and Pd-rich with a composition of $Fe_{30}Pd_{70}$, as determined by EDS analysis. Figure 2 (c) shows another collection of dense NWs named AAO_100_-1.2V of composition $Fe_{56}Pd_{44}$ where the longest NW is 2.8 µm. The flat surface on which these NWs lay is the carbon tape used to observe them under the FESEM. Table 1 shows the two samples' characteristics for comparison. For the same pore size, more negative electrodeposition potential brings more Pd-rich content and reduced NW length. For the same electrodeposition potential, increased pore size leads to more Fe-rich content in the NWs and an overall reduction in the NW length. Therefore, a change in the template pore size promotes different deposition rates of the two elements with a consequent large change in the final NW composition. It is inferable that increased negative electrodeposition potential and bigger pore size cancel out each other's effect on the composition.

Sample name	*Template, pore size*	$E_{electrodeposition}$	*Composition*	*Mean diameter*	*Maximum Length*	*Shape*
AAO_20_-1.15V	AAO, 20 nm	-1.15 V	$Fe_{47}Pd_{53}$	174 nm	5.7 µm	Cylindrical shape with branched bottom
AAO_20_-1.2V	AAO, 20 nm	-1.2 V	$Fe_{30}Pd_{70}$	157 nm	4.7 µm	
AAO_100_-1.2V	AAO, 100 nm	-1.2 V	$Fe_{56}Pd_{44}$	197 nm	3.5 µm	
AAO_200_-1.3V	AAO, 200 nm	-1.3 V	$Fe_{29}Pd_{71}$	225 nm	4.7 µm	
PC_30_-1.2V	PC, 30 nm	-1.2 V	$Fe_{52}Pd_{48}$	65 nm	3.1 µm	Cylindrical shape
PC_50_ 1.05V	PC, 50 nm	-1.05 V	$Fe_{55}Pd_{45}$	135 nm	4.6 µm	
PC_50_-1.15V	PC, 50 nm	-1.15 V	$Fe_{51}Pd_{49}$	113 nm	4.7 µm	
PC_100_-1.2V	PC, 100 nm	-1.2 V	$Fe_{55}Pd_{45}$	222 nm	5.2 µm	
PC_100_-1.3V	PC, 100 nm	-1.3 V	$Fe_{60}Pd_{40}$	156 nm	7.1 µm	

Table 1. Comparison of different parameters and characteristics of dense NWs obtained from AAO and PC templates.

Another set of dense NWs was obtained using the PC membrane for electrodeposition. The electrodepositing electrolyte was the same, i.e., FePd. Membranes of two different pore sizes were used, i.e., 50 and 100 nm. Prior to observing under FESEM, the templates were dissolved using $CHCl_3$, washed in distilled water for several times and then kept dispersed in ethanol after sonicating for few minutes. For viewing under FESEM the samples were prepared in the same manner as described earlier. Figure 3 assembles all the dense NWs obtained from electrodepositing over PC membranes at different deposition potentials. Figure 3 (a) shows FESEM image of dense PC_50_-1.05V NWs attached to the Au layer. The

composition, as determined by EDS, is $Fe_{55}Pd_{45}$. The NWs are cylindrical in shape, with a rough texture on the outer surface as shown in the inset of Figure 3 (a). The NW in the same inset has a small diameter of 59 nm that becomes larger gradually throughout the length going up to 161 nm. Figure 3 (b) shows FESEM image of PC_50_-1.15V where the NWs are attached to the Au layer, after dissolving the template. Applying slightly more negative potential, i.e., -1.15 V, decreased the Fe content of the NWs marginally, as compared to PC_50_-1.05V, which was found to be $Fe_{51}Pd_{49}$. The longest NW holds a length of 4.6 µm. Similar to PC_50_-1.05V, these NWs too have cylindrical shape but a smoother surface texture visible in the inset of Figure 3 (b). The two nanowires displayed in this inset have, on average, a small diameter of 51 nm while a wider diameter of 149 nm as determined.

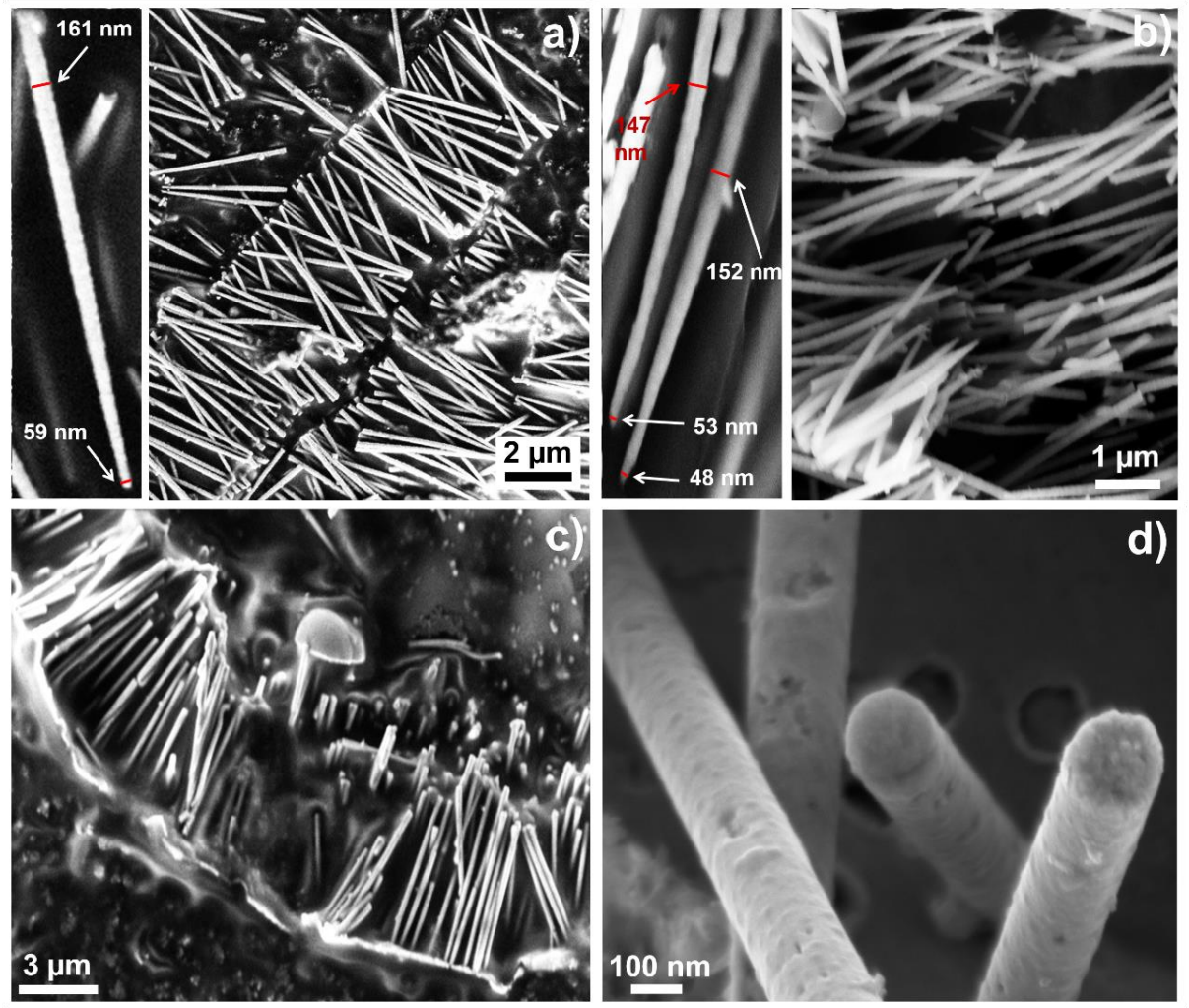

Figure 3. FESEM images of (a) PC_50_-1.05V; (b) PC_50_-1.15V; (c) PC_100_-1.2V; and (d) PC_100_-1.3V.

Next, PC template of 100 nm pore size was used to electrodeposit NWs at -1.2 V (sample PC_100_-1.2V). FESEM image of the same is presented in Figure 3 (c) after dissolving the template and keeping the obtained NWs dispersed in ethanol. The composition is found to be

$Fe_{55}Pd_{45}$. The longest NW is 5.2 µm in length. These NWs too have a cylindrical shape. Figure 3 (d) shows FESEM image of another sample of NWs named PC_100_-1.3V obtained after dissolving the template. The pore size of the template was kept the same, i.e., 100 nm, but a more negative potential was used for electrodeposition. The achieved composition is $Fe_{60}Pd_{40}$. Clearly, applying an increased negative electrodeposition potential resulted in a significant increase in the Fe content in the NWs. The longest NW is 7.1 µm in length. To summarize, Table 1 provides an organized look at the samples' features making it easier to comprehend the trends. For the 50 nm pore size of the template, the composition of the NWs becomes slightly richer in Pd content with a minor increase in the negative electrodeposition potential, as demonstrated by PC_50_-1.05V and PC_50_-1.15V although the overall composition remains Fe-rich. The NW length remains the same. For 100 nm template, the effect is reversed with more negative electrodeposition potential: Fe content increases, again resulting in a Fe-rich composition. If the electrodeposition potential is kept constant, the more the pore size, the higher is the Fe content and longer the NW length, as in the case of PC_30_-1.2V and PC_100_-1.2V. So, overall, it can be concluded that negative electrodeposition potentials and higher pore sizes lead to longer NWs having Fe-rich composition. The shape of all the NWs is cylindrical. It is noteworthy that the dense NWs obtained using PC templates are much longer and more continuous compared to their AAO-obtained counterparts.

3.2. Mesoporous nanowires

Along with the dense NWs, mesoporous NWs have also been produced by electrodepositing at -1.2 V vs Ag/AgCl over 20 and 100 nm Au-sputtered AAO templates, from here onwards the former will be addressed as Meso_20 while the latter as Meso_100. Figure 4 displays the pulsed potentiostatic electrodeposition for Meso_20 and Meso_100 where current density vs. time curves are recorded. The electrodeposition in both the cases appears to be homogeneous and consistent. Figure 5 (a) and (b) display the FESEM images of the first kind, i.e., Meso_20. In Figure 5 (a) collection of FePd NWs can be seen attached to the Au layer. In the inset a free NW can be viewed in a clearer way. It has the characteristic branched structure formed as a result of the AAO membrane. The surface is regular and smooth. No mesoporosity can be observed at this level. But as we increase the magnification further as showcased in Figure 5 (b) a clear mesoporosity is evidenced at the top of the NW. Interestingly enough, this mesoporosity is only present throughout the inside the NW while the outer part is dense. This essentially forms a core-shell structure. The inset of (b) gives an even better look at the top of the NW highlighting the mesoporosity. The composition is determined to be $Fe_{40}Pd_{60.}$ For Meso_100, similar observations have been made. In Figure 5 (c) the top view of the NW array is apparent which in (d) is visible at a higher magnification and in a better clarity. The inset of (d) further reveals the presence of mesoporosity throughout the inside of the NW. For this sample too, the core-shell structure is obvious. Figure 6 shows the EDS maps of a Meso_100 NW establishing the presence of Pd and Fe

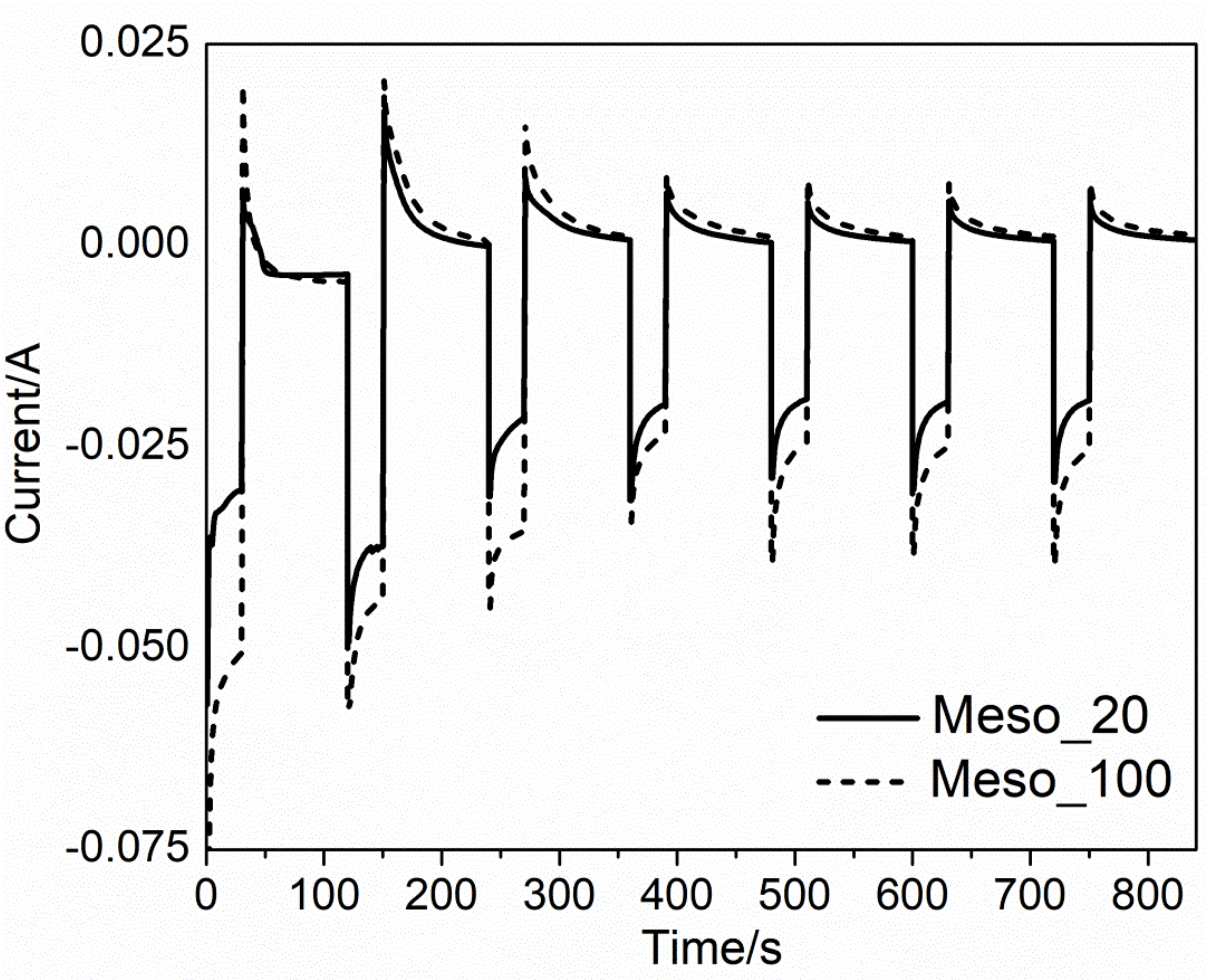

Figure 4. Pulsed potentiostatic electrodeposition curve for Meso_20 and Meso_100, both at -1.2 V vs Ag/AgCl.

homogeneously spread throughout the NW, so suggesting the presence of a single phase formed during the synthesis. No oxidation is observed and the overall composition of the NWs comes out to be $Fe_{40}Pd_{60}$. Table 2 summarizes the similarities and differences between Meso_20 and Meso_100.

From the phase diagram of Fe and Pd, it is apparent that the composition of $Fe_{40}Pd_{60}$ corresponds to a region in which two phases are stable, i.e., FePd and $FePd_3$. Nevertheless, metastable phases formation can be expected due to the synthesis technique used. As observed from EDS map in Figure 6, one phase is expected, so the presence of a metastable FePd can be inferred. XRD was performed to confirm the same by analyzing the structure of the as-deposited NWs, Meso_20. The NWs were kept embedded in their AAO template for obtaining the XRD pattern. Figure 7 displays the diffraction pattern of Meso_20 in blue. Characteristic peak of aluminium oxide is visible denoted by a green dot. Reflections of the fcc crystalline structure are detected labelled using red triangles. No secondary phases are

present confirming the EDS results. From a rough estimation of the lattice parameter for Meso_20, a_0 comes out to be 0.388 nm which is in accordance with the a_0 of 0.386 nm for FePd alloy.[21]

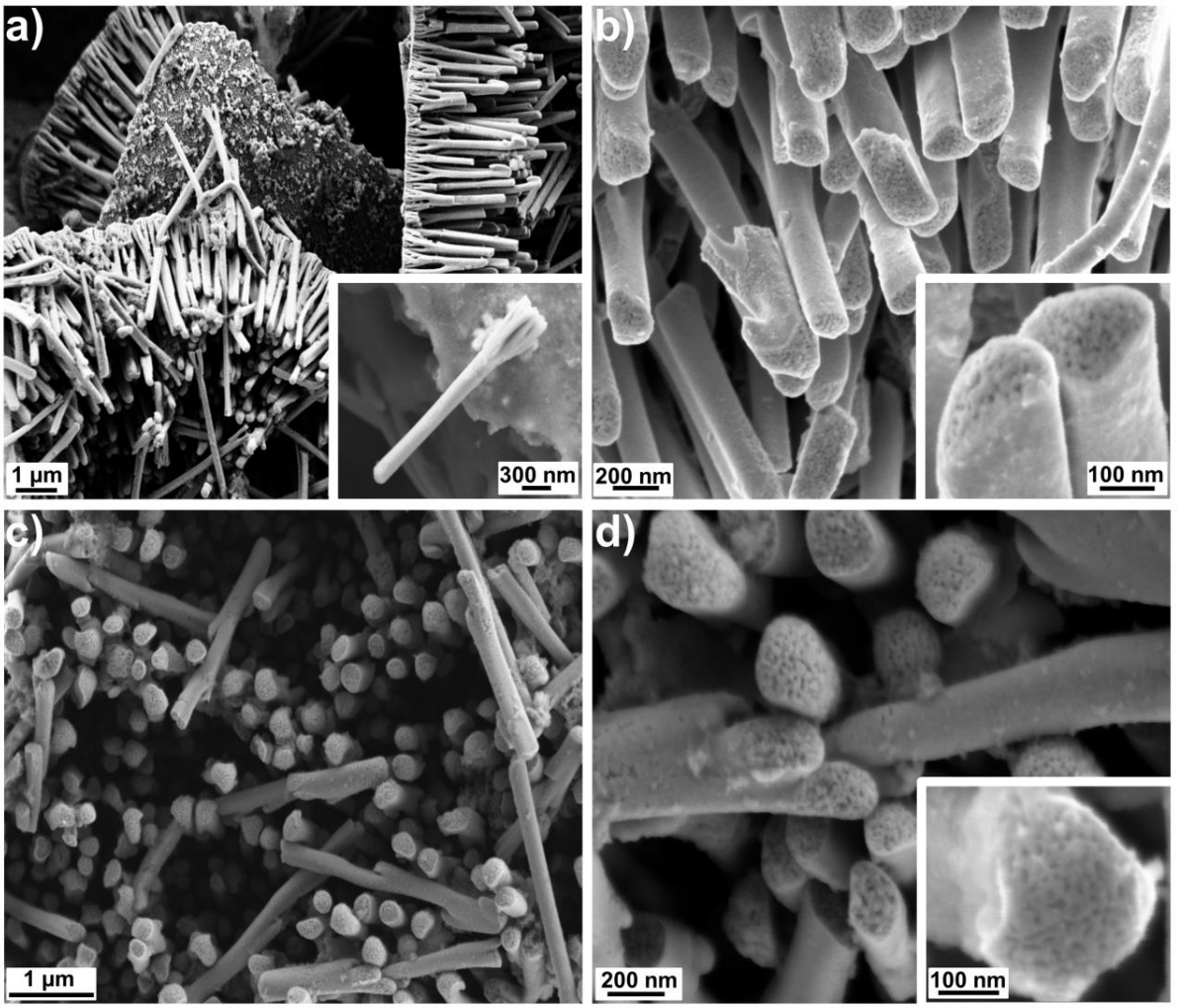

Figure 5. SEM images of $Fe_{40}Pd_{60}$ mesoporous NWs: (a) Meso_20, inset shows a single free NW at higher magnification; (b) magnified view of Meso_20; (c) Meso_100; (d) magnification of Meso_100; and insets of (b) and (d) give a closer look at the mesoporosity.

Sample name	*Template, pore size*	$E_{electrodeposition}$	*Composition*	*Mean diameter*	*Length*	*Shape*
Meso_20	AAO, 20 nm	-1.2 V	$Fe_{40}Pd_{60}$	168 nm	3.2 µm	Cylindrical shape with branched bottom
Meso_100	AAO, 100 nm			197 nm	2.6 µm	

Table 2. Comparison of different parameters and characteristics of Meso_20 and Meso_100.

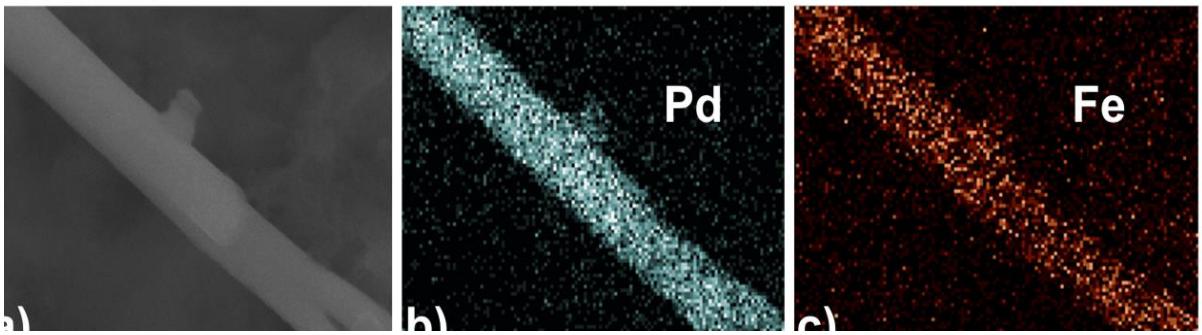

Figure 6. EDS maps of Meso_100 showing the presence and distribution of Pd and Fe throughout the length of the NW.

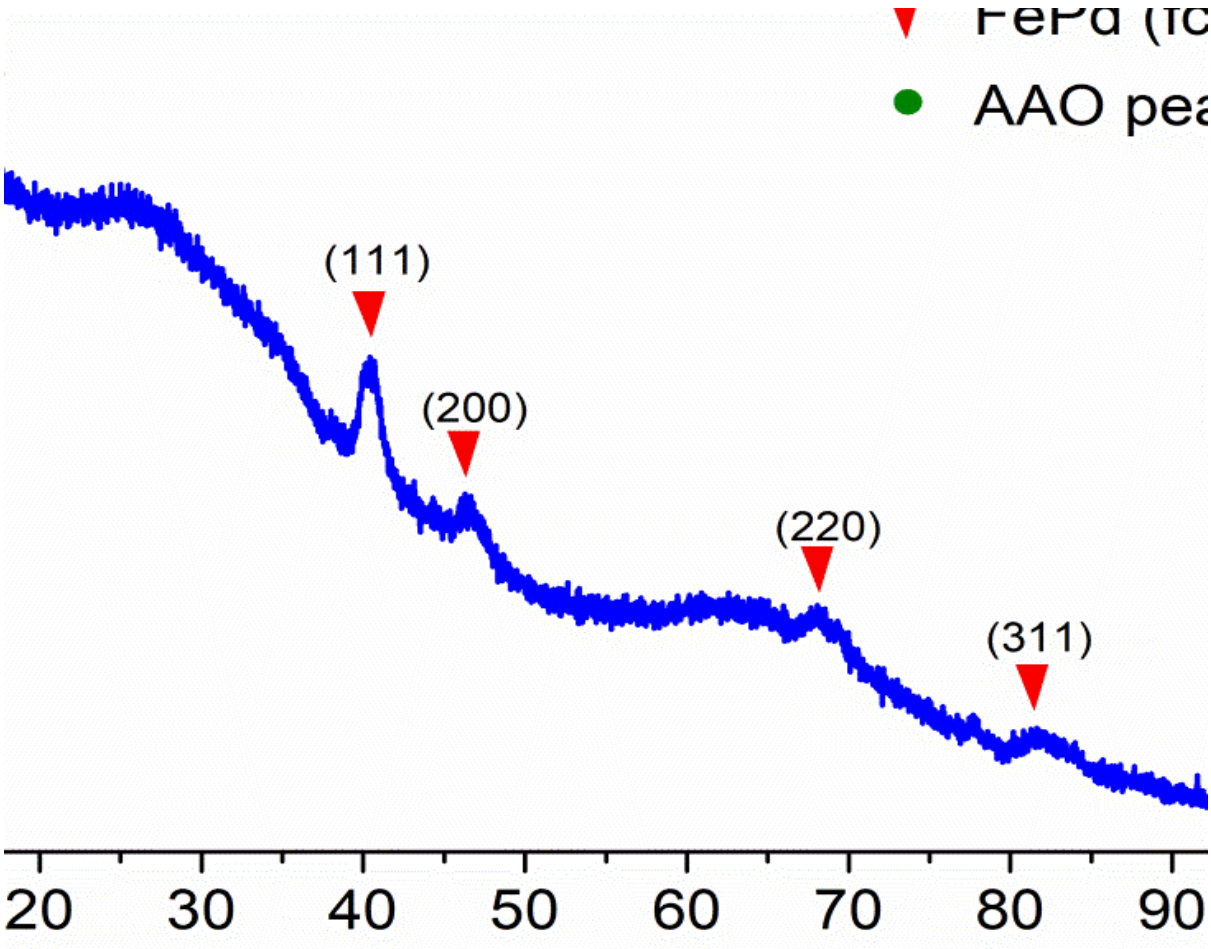

Figure 7. XRD pattern of the as-deposited Meso_20 embedded in the AAO template.

The morphology of the nanowires was also observed by TEM after completely dissolving the template as described previously in case of FESEM sample preparation. A very small amount of ethanol containing the dispersed NWs was dropped onto a Cu grid to observe under TEM. Figure 8 shows the bright-field TEM image of the as-deposited mesoporous FePd NWs,

Meso_20. From the high-resolution (HR) bright-field TEM image in Figure 8 (c), the sharply defined lattice planes with distances of 0.219 nm can be observed. This calculated lattice space is in accordance with that obtained from XRD measurement corresponding to the (111) plane of the FePd phase.

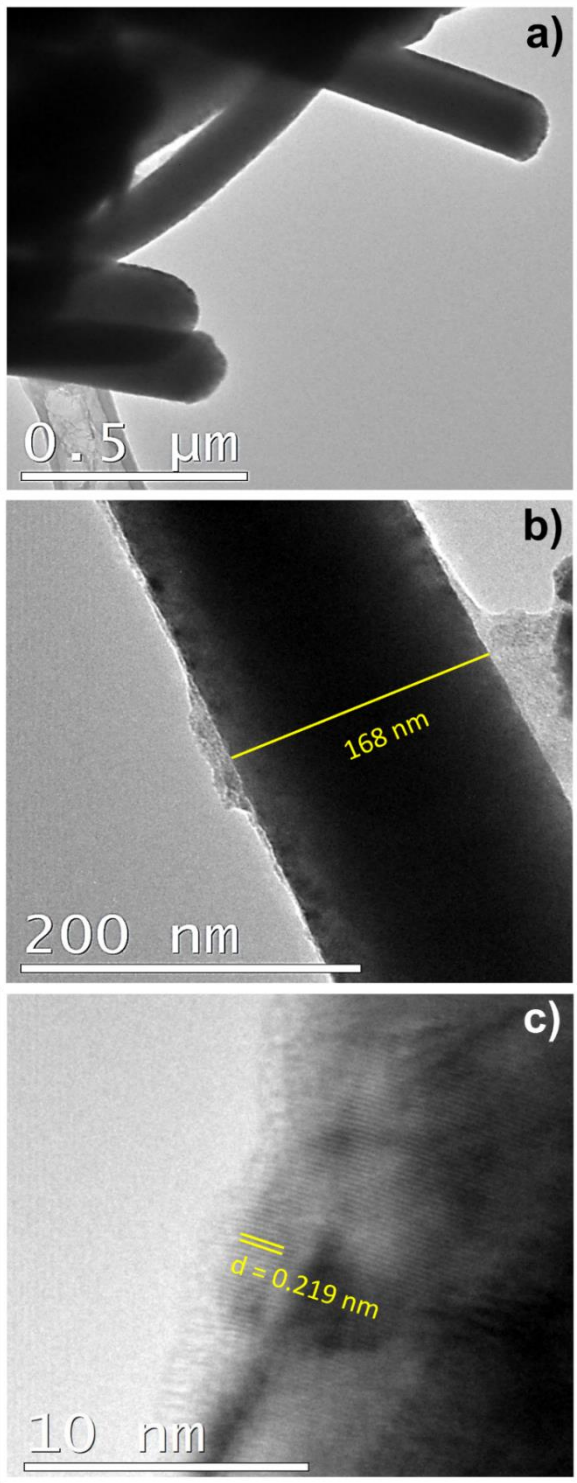

Figure 8. Bright-field TEM images of Meso_20 NWs.

3.3. Magnetic studies

Room-temperature hysteresis loops of the AAO_20_-1.2V and AAO_100_-1.2V samples are shown in Figure 9. The curves obtained by applying H along the direction parallel (PA) and perpendicular (PE) to the major axis of the nanowires are compared for both samples; all curves are normalized to the magnetization value at H = 15 kOe. The values of the magnetic properties such as saturating field (H_s), coercive field (H_c), magnetic susceptibility evaluated at the coercive field (χ_{Hc}), and the normalized magnetization remanence (M_r/M_s) are reported in Table 3.

Both samples are ferromagnetic with a well-defined hysteretic behavior. In AAO_20_-1.2V sample, the hysteresis loops measured along PA and PE direction appear different (see Figure 9 (a)) indicating an anisotropic behavior of this sample. In particular, the PA magnetization approaches the saturation at lower H_s with a reversal mechanism over a narrower field interval with respect to PE one. The coercive field slightly decreases from PA to PE direction. These results suggest that the PA direction, i.e., along the major axis of the NWs, is the easy axis of magnetization.

Conversely, the hysteresis loops of the AAO_100_-1.2V sample measured along the PA and PE directions appear almost superimposed suggesting an almost isotropic magnetic behavior (see Figure 9 (b)). A slight preference for the PA direction as an easy axis of magnetization can be inferred from the inset of Figure 9 (b) and the χ_{Hc} values (see Table 3). However, both curves display a reversal of magnetization characterized by a steep jump with a χ_{Hc} higher than the one of AAO_20_-1.2V sample. Moreover, after the magnetization jump, a slow approach to saturation ending at $H \approx 15$ kOe is observed. The coercive field values are coincident for both PA and PE direction in the AAO_100_-1.2V sample but result to be one order of magnitude lower than the one measured in the AAO_20_-1.2V sample.

Room-temperature hysteresis loops of the mesoporous nanowires are shown in Figure 10. The main magnetic anisotropic features observed in dense nanowires has been preserved: the Meso_20 sample displays isotropic behavior with a magnetic easy-direction along the major-axis of the NWs, whereas an almost anisotropic behavior is found in the Meso_100 sample.

However, the core-shell structure of the NWs, i.e., mesoporous core and dense shell, slightly affects the magnetic properties, see Table 1. Specifically, all curves of mesoporous NWs show an increase of the coercive field, especially for the Meso_100 sample, as well as more robustness of the magnetic disorder which hinders a deep magnetic saturation up to 15 kOe. The χ_{Hc} values are comparable in the AAO_20_-1.2V and Meso_20 samples whereas an evident decrease is found in Meso_100 sample with respect to the AAO_100_-1.2V one.

All these magnetic features suggest that the formation of the mesoporous structure arises local magnetic anisotropy that influences the overall magnetization process distributing the irreversible processes larger portion of the hysteresis loop and hindering the domain wall motion. This effect is mainly evident in the Meso_100 sample.

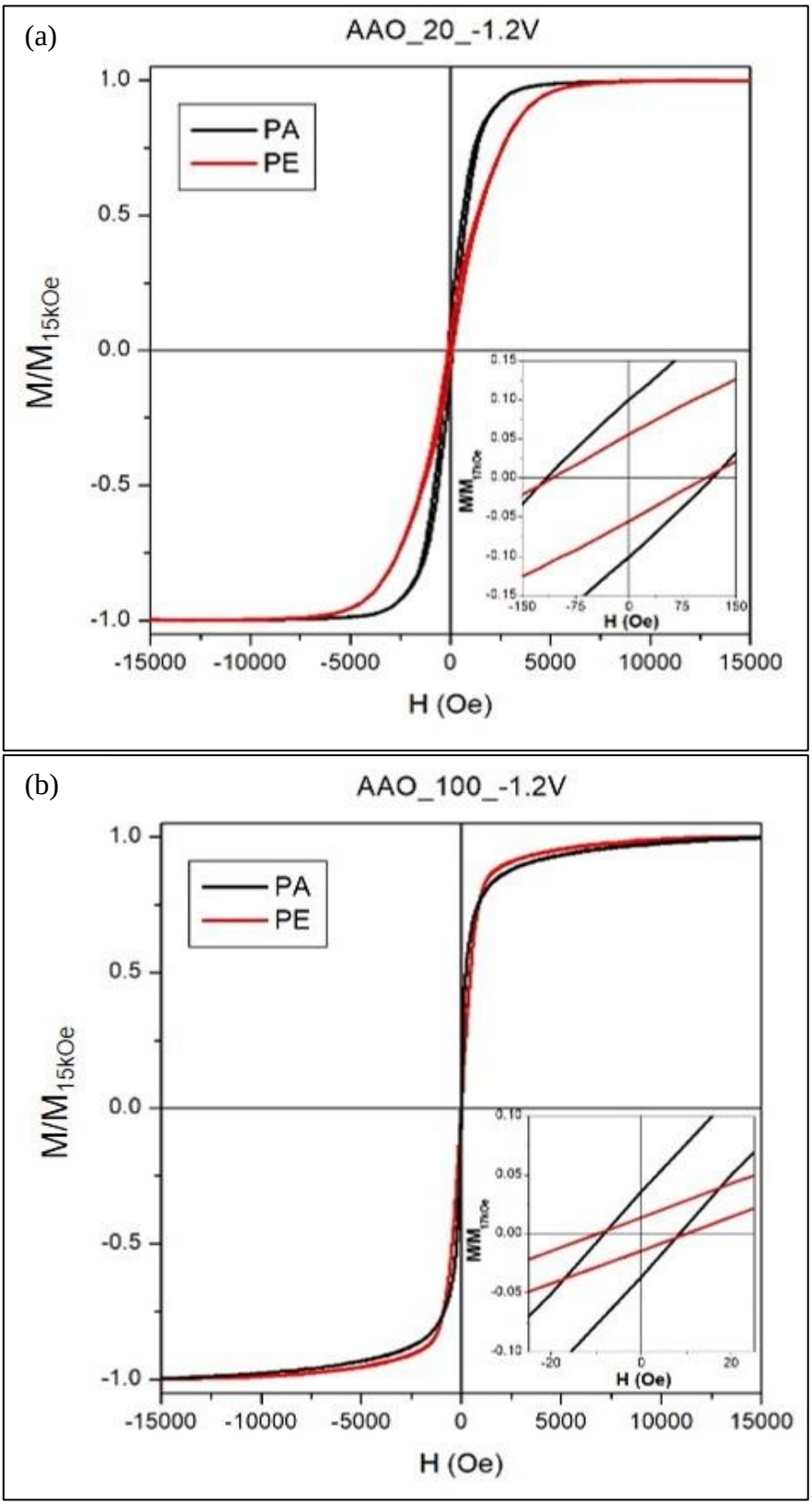

Figure 9: Room-temperature hysteresis loops of (a) AAO_20_-1.2V sample and (b) AAO_100_-1.2V sample by applying H along the direction parallel (PA) and perpendicular (PE) to the major axis of the nanowires. Inset: enlargement of hysteresis loops at low magnetic field.

Sample	*H direction*	H_s *(kOe)*	H_c *(Oe)*	χ_{Hc} *(Oe^{-1})*	M_r/M_s
AAO_20_-1.2V	PA	≈ 5	115	8.4×10^{-4}	1.0×10^{-1}
	PE	≈ 7.5	107	5.1×10^{-4}	5.6×10^{-2}
AAO_100_1.2V	PA	≈ 15	10	4.1×10^{-3}	3.6×10^{-2}
	PE	≈ 15	10	1.4×10^{-3}	1.4×10^{-2}
Meso_20	PA	> 15	128	9.7×10^{-4}	1.1×10^{-1}
	PE	>15	140	4.4×10^{-4}	8.5×10^{-2}
Meso_100	PA	> 15	61.5	3.9×10^{-4}	2.0×10^{-2}
	PE	>15	71	4.6×10^{-4}	3.9×10^{-2}

Table 3. Magnetic properties evaluated from hysteresis loops reported in Figure 9 and 10. Saturation field (H_s), coercive field (H_c), magnetic susceptibility evaluated at the coercive field χ_{Hc} and the normalized magnetization remanence (M_r/M_s)

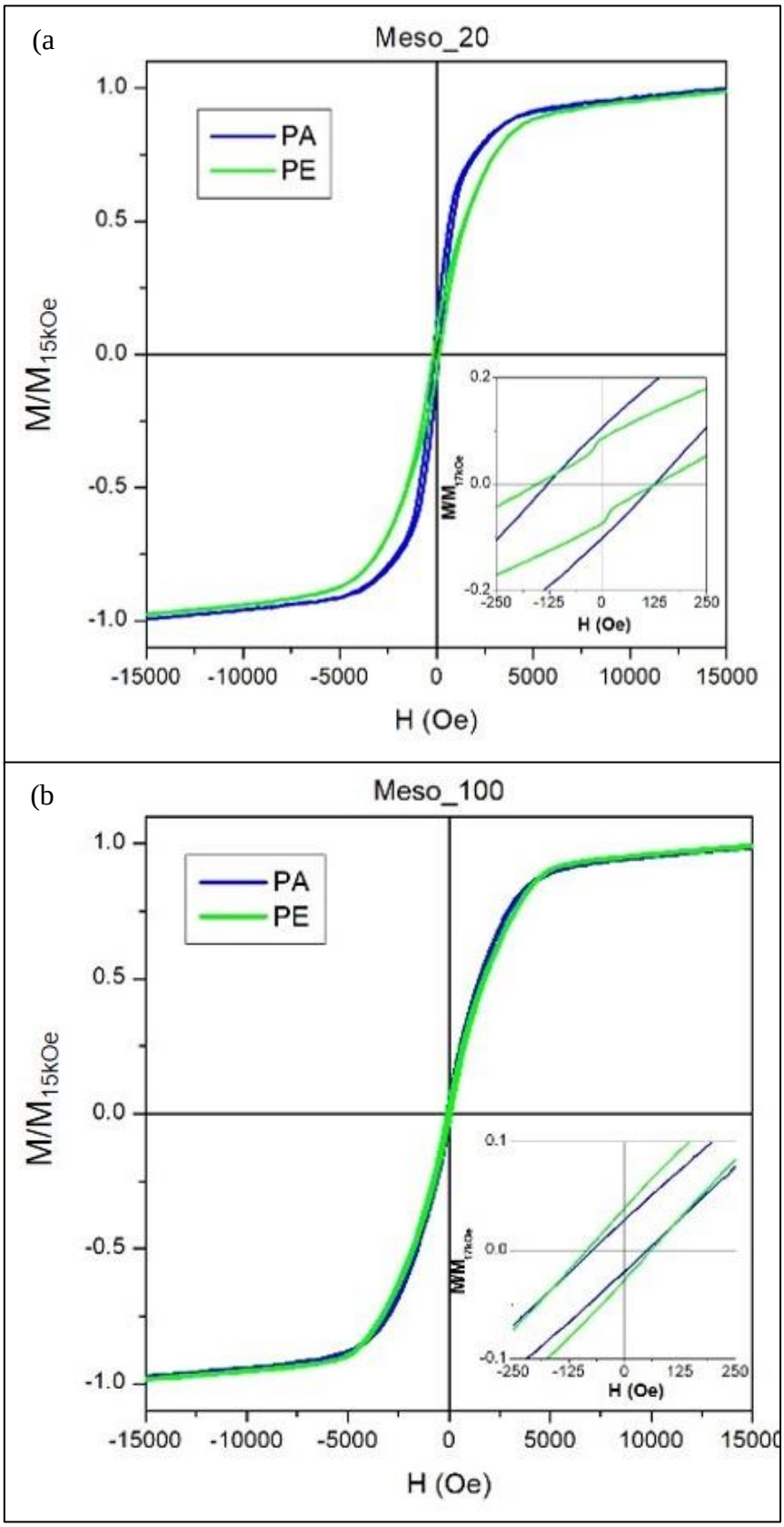

Figure 10: Room-temperature hysteresis loops of (a) Meso_20 sample and (b) Meso_100 sample by applying H along the direction parallel (PA) and perpendicular (PE) to the major axis of the nanowires. Inset: enlargement of hysteresis loops at low magnetic field.

4. Conclusion

In conclusion, dense and mesoporous FePd NWs have been successfully fabricated with different compositions. The method employed was template- and micelle- assisted pulsed-potentiostatic electrodeposition where the templates were nanoporous anodic alumina and polycarbonate discs. The as-deposited NWs are found to have the fcc structure and hold variety of shapes and sizes. Dense AAO-derived NWs exhibited a cancelling out effect where more negative electrodeposition potential and bigger pore size resulted in a stable composition. In case of PC-derived dense NWs, more negative electrodeposition potentials and larger pore sizes produced longer, Fe-rich NWs. Moreover, PC-derived dense NWs are much longer and more continuous compared to their AAO-derived counterparts. On the other hand, mesoporous NWs have a core-shell structure with a Pd-rich composition. Interesting magnetic properties have been also determined by obtaining room temperature hysteresis loops for two samples each of dense and mesoporous NWs, i.e., AAO_20_-1.2V, AAO_100_-1.2V, Meso_20 and Meso_100 respectively. Both dense NWs are ferromagnetic. AAO_20_-1.2V indicates an anisotropic magnetic behavior with the easy axis of magnetization being the PA direction, i.e., along the major axis of the NWs. In contrast, AAO_100_-1.2V shows an almost isotropic magnetic behaviour while maintaining the PA direction as the easy axis of magnetization. As for the mesoporous NWs, Meso_20 behaves similar to AAO_100_-1.2V and Meso_100 similar to AAO_20_-1.2V.

5. References

[1] P. Domenichini, A.M. Condó, N. Haberkorn, Structural characterization of Fe Pd nanowires grown by electrodeposition using an acid electrolyte, Mater. Chem. Phys. 177 (2016) 164–170. https://doi.org/10.1016/j.matchemphys.2016.04.013.

[2] C. Navarro-Senent, S. Pané, J. Sort, E. Pellicer, The order of addition and time matters: Impact of electrolyte processing on micelle-assisted electrosynthesis of mesoporous alloys, Electrochim. Acta. 358 (2020) 136940. https://doi.org/10.1016/j.electacta.2020.136940.

[3] K.M. Pondman, N.D. Bunt, A.W. Maijenburg, R.J.A. van Wezel, U. Kishore, L. Abelmann, J.E. ten Elshof, B. ten Haken, Magnetic drug delivery with FePd nanowires, J. Magn. Magn. Mater. 380 (2015) 299–306. https://doi.org/10.1016/j.jmmm.2014.10.101.

[4] B.Z. Cui, M. Marinescu, J.F. Liu, L10-FePd nanocluster wires by template-directed thermal decomposition and subsequent hydrogen reduction, J. Appl. Phys. 114 (2013) 0–5. https://doi.org/10.1063/1.4845455.

[5] L. Qin, Z. Zeng, G. Zeng, C. Lai, A. Duan, R. Xiao, D. Huang, Y. Fu, H. Yi, B. Li, X. Liu, S. Liu, M. Zhang, D. Jiang, Cooperative catalytic performance of bimetallic Ni-Au nanocatalyst for highly efficient hydrogenation of nitroaromatics and corresponding mechanism insight, Appl. Catal. B Environ. (2019). https://doi.org/10.1016/j.apcatb.2019.118035.

[6] G. Barrera, F. Celegato, M. Cialone, M. Coïsson, P. Rizzi, P. Tiberto, Structural, Wetting and Magnetic Properties of Sputtered Fe70Pd30 Thin Film with Nanostructured Surface Induced by Dealloying Process, Nanomaterials. 11 (2021) 282. https://doi.org/10.3390/nano11020282.

[7] A. Benhamoud, A. Kharmouche, Synthesis, Structural, and Magnetic Properties of Fe100-xPdx Thin Films, J. Supercond. Nov. Magn. (2020). https://doi.org/10.1007/s10948-019-05412-1.

[8] J.S. Riva, A. V. Juárez, S.E. Urreta, L.M. Yudi, Catalytic properties of Fe–Pd ferromagnetic nanowires at liquid/liquid interfaces, Electrochim. Acta. (2019). https://doi.org/10.1016/j.electacta.2018.12.069.

[9] S. Tamura, T. Mashimo, K. Yamamoto, Z. Kelgenbaeva, W. Ma, X. Kang, M. Koinuma, H. Isobe, A. Yoshiasa, Synthesis of Pd-Fe system alloy nanoparticles by pulsed plasma in liquid, Nanomaterials. (2018). https://doi.org/10.3390/NANO8121068.

[10] Q. Shi, C. Zhu, D. Du, Y. Lin, Robust noble metal-based electrocatalysts for oxygen evolution reaction, Chem. Soc. Rev. (2019). https://doi.org/10.1039/c8cs00671g.

[11] V. Haehnel, C. Mickel, S. Fähler, L. Schultz, H. Schlörb, Structure, Microstructure, and Magnetism of Electrodeposited Fe 70 Pd 30 Nanowires, J. Phys. Chem. C. 114 (2010) 19278–19283. https://doi.org/10.1021/jp1077455.

[12] M.S. Viqueira, S.E. Garcia, S.E. Urreta, G. Pozo Lopez, L.M. Fabietti, Hysteresis Properties of Hexagonal Arrays of FePd Nanowires, IEEE Trans. Magn. 49 (2013) 4498–4501. https://doi.org/10.1109/TMAG.2013.2258461.

[13] E. Herrera, M.S. Aprea, J.S. Riva, O.F. Silva, P.G. Bercoff, A. Granados, FePd nanowires modified with cyclodextrin. Characterization and catalytic properties evaluated by a model reduction reaction, Appl. Surf. Sci. 529 (2020) 1–14. https://doi.org/10.1016/j.apsusc.2020.147029.

[14] X.L. Fei, S.L. Tang, R.L. Wang, H.L. Su, Y.W. Du, Fabrication and magnetic properties of Fe-Pd nanowire arrays, Solid State Commun. 141 (2007) 25–28. https://doi.org/10.1016/j.ssc.2006.09.042.

[15] M. Gößler, M. Nachtnebel, H. Schröttner, H. Krenn, E.M. Steyskal, R. Würschum, Evolution of superparamagnetism in the electrochemical dealloying process, J. Appl. Phys. (2020). https://doi.org/10.1063/5.0015397.

[16] E. Herrera, M.S. Aprea, J.S. Riva, O.F. Silva, P.G. Bercoff, A. Granados, FePd nanowires modified with cyclodextrin. Characterization and catalytic properties evaluated by a model reduction reaction, Appl. Surf. Sci. 529 (2020) 147029. https://doi.org/10.1016/j.apsusc.2020.147029.

[17] B. Saida, L. Ali, G. Abderrahim, F. Abeslem, B. Mokhtar, Magnetic properties of bcc and bcc-fcc Fe-Pd alloys produce by thermal evaporation technique, Phys. Procedia. 54 (2014) 81–86. https://doi.org/10.1016/j.phpro.2014.10.040.

[18] G. Barrera, F. Scaglione, M. Cialone, F. Celegato, M. Coïsson, P. Rizzi, P. Tiberto, Structural and Magnetic Properties of FePd Thin Film Synthesized by

Electrodeposition Method, (2020) 1–15.

[19] E. Dislaki, M. Cialone, F. Celegato, P. Rizzi, P. Tiberto, S. Vadilonga, D. Többens, J. Sort, E. Pellicer, Unraveling the properties of sharply defined submicron scale FeCu and FePd magnetic structures fabricated by electrodeposition onto electron-beam-lithographed substrates, Mater. Des. 193 (2020). https://doi.org/10.1016/j.matdes.2020.108826.

[20] V. Haehnel, S. Fähler, L. Schultz, H. Schlörb, Electrodeposition of Fe70Pd30 nanowires from a complexed ammonium–sulfosalicylic electrolyte with high stability, Electrochem. Commun. 12 (2010) 1116–1119. https://doi.org/10.1016/j.elecom.2010.05.043.

[21] S.D. Willoughby, J.M. MacLaren, T. Ohkubo, S. Jeong, M. McHenry, D.E. Laughlin, S.-J. Choi, S.-J. Kwon, Electronic, magnetic, and structural properties of L1[sub 0]FePt[sub x]Pd[sub 1−x] alloys, J. Appl. Phys. 91 (2002) 8822. https://doi.org/10.1063/1.1450850.

Chapter VI

CONCLUSIONS

Given the immense potential of nanostructured materials in a wide array of applications, I dedicated the three years of my PhD to the fabrication of diverse types of nanostructured materials, i.e., nanostructured Mo oxide, nanoporous gold and FePd nanowires. I invested my time in working through several synthetic approaches, carefully characterizing the resultant materials and studying their unique chemical and physical properties in full detail. To fulfil the aim of exploiting these materials for different applications I conducted specific experiments related to HER, SERS and MeOH electrooxidation with the prepared nanostructured materials.

Some of the main achievements of this PhD thesis are pointed out below:

(i) Nanostructured Mo oxides have been successfully obtained by free corrosion using an intermetallic precursor, Mo_3Al_8. Single and double-step free corrosion were conducted in 1 M KOH, 1 M HF and 1.25 M $FeCl_3$ at room temperature for varying durations. HF worked better for Al removal in case of single-step free corrosion but overall, double-step free corrosion turned out to be a better alternative in terms of both morphology and composition of the as-treated sample. The resultant sample, DS_1h, exhibited nanostructural morphology with a 3 µm thick layer rich in MoO_3. The sample when tested as electrocatalyst for HER in 0.5 M H_2SO_4 gave low onset potential of -45 mV; small Tafel slope of 89 mV dec^{-1} indicating Volmer as the rate-determining step; low overpotential of -1.24 V for current density of -10 mA cm^{-2}; high exchange current density of 0.35 mA cm^{-2}; and stability of up to 15 h with no significant changes in its properties. Considering that the samples are obtainable via a fast, simple, low-cost and sustainable overall process these findings are certainly very promising.

(ii) The fabrication and characterization of nanoporous gold from a cost-active precursor, $Au_{33}Fe_{67}$, were targeted upon and studied in depth. With a huge miscibility gap at room temperature the Au-Fe system poses a challenge to obtain a solid solution at room temperature which was actively conquered by the technique of rapid solidification. This technique allowed for the formation of a metastable supersaturated biphasic $Au_{33}Fe_{67}$ solid solution at room temperature. The NPG samples were obtained by chemically dealloying the precursor. All the obtained samples displayed well-defined three-dimensional nanoporous morphology. As the dealloying time increased, Au atomic percentage, ligament size, and the homogeneity of the surface morphology increased. The samples possessing largest active surface areas and resultingly highest number of active sites were utilized in HER, SERS and MeOH-EOx applications. NPG_8h shows low overpotential of -0.38 V for a current density of 5 mA cm^{-2}, small Tafel slope of 47 mV dec^{-1}, very low onset potential of -4 mV and high exchange current density of 0.12

mA cm^{-2} as well as excellent durability of more than 20 h in 0.5 M H_2SO_4. NPG_8h also exhibited a detection limit of 10^{-15} M for bipyridine showcasing presence of hot spots and highly sensitive SERS activity. NPG_16h demonstrated a low peak potential of -0.47 V vs Ag/AgCl, high current density of 0.43 mA/cm^2 at the oxidation peak potential, impressive stability and high poisoning tolerance in a basic solution of methanol and KOH. Overall, the performance shown by the samples is remarkable. The combination of a straight-forward and fast synthesis method and a cheap Fe-rich precursor, without the use of critical raw materials, has resulted in high-quality NPG samples that serve as efficient, durable, and sustainable alternative electrocatalysts for HER, and MeOH electrooxidation as well as exceptional SERS-active substrate.

(iii) FePd nanowires, dense and mesoporous, have been fabricated with different compositions and diameters by template- and micelle-assisted electrodeposition via pulsed-potentiostatic electrodeposition method on nanoporous anodic alumina and polycarbonate membranes. The obtained NWs hold a fcc structure. Dense AAO-derived NWs exhibited a cancelling out effect where more negative electrodeposition potential and bigger pore size resulted in a stable composition. In case of PC-derived dense NWs, more negative electrodeposition potentials and larger pore sizes produced longer, Fe-rich NWs. Moreover, PC-derived dense NWs are much longer and more continuous compared to their AAO-derived counterparts. On the other hand, mesoporous NWs have a core-shell structure with a Pd-rich composition. Interesting magnetic properties have been also determined by obtaining room temperature hysteresis loops for two samples each of dense and mesoporous NWs, i.e., AAO_20_-1.2V, AAO_100_-1.2V, Meso_20 and Meso_100 respectively. Both dense NWs are ferromagnetic. AAO_20_-1.2V indicates an anisotropic magnetic behavior with the easy axis of magnetization being the PA direction, i.e., along the major axis of the NWs. In contrast, AAO_100_-1.2V shows an almost isotropic magnetic behaviour while maintaining the PA direction as the easy axis of magnetization. As for the mesoporous NWs, Meso_20 behaves similar to AAO_100_-1.2V and Meso_100 similar to AAO_20_-1.2V.

As a final note, it can be stated that the research work undertaken during the duration of this PhD fruitfully delivered some solid and effective results making a genuine and worthy contribution in the field of nanostructured materials and their application as electrocatalysts for hydrogen evolution reaction and methanol electrooxidation and as SERS-active substrates.

PhD Activities

Papers:

- M. Cialone, F. Celegato, F. Scaglione, G. Barrera, D. Raj, M. Coïsson, P. Tiberto, P. Rizzi, Nanoporous FePd alloy as multifunctional ferromagnetic SERS-active substrate. Applied Surface Science, 2020, 543, 148759, 10.1016/j.apsusc.2020.148759.

- D. Raj; F. Scaglione; G. Fiore; F. Celegato; P. Rizzi, Nanostructured Molybdenum Oxides from Aluminium-Based Intermetallic Compound: Synthesis and Application in Hydrogen Evolution Reaction, Nanomaterials, 2021, 11, 1313, https://doi.org/10.3390/nano11051313.

- Deepti Raj, Mauro Palumbo, Federico Scaglione, Gianluca Fiore, Federica Celegato, Paola Rizzi, "Low-cost Nanoporous Gold obtained by dealloying metastable precursor, $Au_{33}Fe_{67}$, reveals excellent HER and SERS performance", Journal of Materials Chemistry A, 2021. (Under Review)

- Deepti Raj, Federico Scaglione, Gianluca Fiore, Federica Celegato, Paola Rizzi, "Excellent performance by cost-effective Nanoporous Gold as an electrocatalyst for Methanol Electrooxidation". (In writing)

- Deepti Raj, Federico Scaglione, Gianluca Fiore, Federica Celegato, Paola Rizzi, "Mechanism of chemical dealloying of metastable $Au_{33}Fe_{67}$ precursor to obtain Nanoporous Gold". (In writing)

- Deepti Raj, Gabriele Barrera, Aliona Nicolenco, Federica Celegato, Federico Scaglione, Jordi Sort, Eva Pellicer, Paola Tiberto, Paola Rizzi, "FePd dense and mesoporous nanowires: Synthesis and Characterization" - (In writing)

- Deepti Raj, Federico Scaglione, Paola Rizzi, "Review on Applications of Nanoporous Gold – Current Progress". (In writing)

Talks:

Presenting author is underlined.

- "Nanoporous Gold from $AuFe_2$ Precursor: Synthesis and Application" - D. Raj, Annual Metallurgy Lab Meeting, Italy (Vaie), 9th July, 2019.

- Second year PhD presentation, D. Raj, Department of Chemistry, University of Turin, Turin, Italy, 25th September, 2019.

- "Dealloying for the synthesis of Nanoporous Molybdenum and Gold" - D. Raj, Seminar, Department of Chemistry, Metallurgy group, University of Turin, Turin, Italy, 14th February, 2020.

- "Nanoporous Gold obtained by dealloying $AuFe_2$ precursor – a promising low-cost electrocatalyst for Hydrogen Evolution reaction" - D. Raj, M. Palumbo, G. Fiore, F. Celegato, F. Scaglione, P. Rizzi, 5th International Conference on Materials Engineering and Nano Sciences (ICMENS), 23rd - 25th March, 2021 **(Best Oral Presentation Award)**

- "Nanoporous Gold obtained by dealloying $AuFe_2$ precursor – a promising low-cost electrocatalyst for Hydrogen Evolution reaction" - D. Raj, M. Palumbo, G. Fiore, F. Celegato, F. Scaglione, P. Rizzi, New Trends in Materials Science and Engineering (NewTimes), 14th - 18th June, 2021.

- "Nanoporous Gold obtained by dealloying $AuFe_2$ precursor – a promising low-cost electrocatalyst for Hydrogen Evolution reaction" - D. Raj, M. Palumbo, G. Fiore, F. Celegato, F. Scaglione, P. Rizzi, European Congress and Exhibition on Advanced Materials and Processes – Euromat, 13th - 17th September, 2021.

- "FePd dense and mesoporous nanowires: Synthesis and Characterization" - D. Raj, Annual Metallurgy Lab Meeting, Italy (Vaie), 21st September, 2021.

- "Nanoporous Gold obtained by dealloying $AuFe_2$ precursor – a promising low-cost electrocatalyst for Hydrogen Evolution reaction" - D. Raj, M. Palumbo, G. Fiore, F. Celegato, F. Scaglione, P. Rizzi, MRS Fall Meeting and Exhibit, Virtual, 6th - 8th December, 2021.

Conferences attended:

- Nanobiology Conference - 17th October, 2019.

- 2020 Virtual MRS Spring/Fall Meeting and Exhibit, Virtual, 27th November -4th December, 2020.

- 5th International Conference on Materials Engineering and Nano Sciences (ICMENS 2021), Japan, 23rd - 25th March, 2021,

- NewTimes – New Trends in Materials Science and Engineering (NEWTIMES), 2021, Virtual, 14th - 18th June, 2021.

- European Congress and Exhibition on Advanced Materials and Processes - Euromat 2021, Virtual, 13th - 17th September, 2021,

- 2021 MRS Fall Meeting and Exhibit, Virtual, 6th -8th December, 2021.

Period Abroad:

- April to June 2021, Universitat Autonoma de Barcelona, Spain

  Supervisor: Prof. Eva Pellicer Prof. Radovan Černý.

PhD Courses and Schools Attended:

- "Aldo Armigliato" SEM School in Materials Science 2019, Italy (Trieste), 9th - 12th April, 2019.

- International Spring School of Electrochemistry – ISSE, Italy (Castellammare del Golfo), 19th - 23rd May, 2019.

- Crystallography School 2019 – CRISDI, Italy (Turin), 27th May - 14th June, 2019.

- Aerospace metallic materials and technologies, Prof. Maciej Motyka, University of Turin.

- BC1 - Introduction to Crystallography, Prof. P. Benna, Dr. S. Capella, University of Torino (CRISDI 2019).

- BC4 - X-Ray Diffraction, Prof. A. Pavese, University of Torino (CRISDI 2019).

- BC5 - X-Ray Diffraction Methods: Polycrystalline, Prof. M. Milanesio, University of Piemonte Orientale (CRISDI 2019).

- SC6. Inorganic Crystallochemistry, Prof. Rossella Arletti (CRISDI 2019).

- SC7 - The Debye Scattering Equation: A Total Scattering approach for characterizing Nanomaterials, Dr. F. Bertolotti, University of Insubria (Como) (CRISDI 2019).

- SC8 - The Rietveld Method, Dr. A. Agostino, University of Turin (CRISDI 2019).

- SC9 - Introduction to Crystal Growth, Dr. E. Costa, University of Turin (CRISDI 2019).

- SC10 - Crystal Growth for Beginners, University of Turin (CRISDI 2019).

- SC14 - X-Ray Diffraction Applications on Materials Study, Prof. Ronchetti et al, University of Torino (CRISDI 2019).

- Raman Days 2021, Department of Earth Sciences, University of Turin.

Seminars/Workshops attended

- Thermodynamics of Boron-based Complex Hydrides for Energy Storage - Italy (Turin), PhD defense by E. M. Dematteis, 19th October, 2018.

- Spin Dependent Electrochemistry - Italy (Turin), Seminar by Claudio Fontanesi, 6th November, 2018.

- Aluminum Alloys for Additive Manufacturing and their Thermal Treatments - Italy (Turin), Seminar by Dario Gianoglio, 19th January, 2019.

- Synthesis and Characterization of Ullmannite Compounds - Italy (Turin), Seminar by Francesco Aversano, 8th February, 2019.

- Materials and microstructures in Additive Manufacturing (Workshop) - Italy, 14th February, 2019.

- Low-Dimensional Dense and Nanostructured Fe-based Alloys for Smart Materials - Italy (Turin), PhD defense by Matteo Cialone, 2nd April, 2019.

- Annual lab meeting - Metallurgy group, Italy, 9th July, 2019.

- PhD DAY (Workshop) - 26th - 27th September, 2019.

- Complex hydrides as solid-state electrolyte for Li-ion batteries (Seminar) - 17th October, 2019.

- Optimization and development of thermoelectric intermetallic compounds for waste heat harvesting (Seminar) - 28th January, 2020.

- NIS colloquium (Workshop) - 29th January, 2020.

- Aluminum alloys for Additive Manufacturing: alloys microstructure, rapid solidification processes, testing of products (Seminar) - 7th February, 2020.

- Lab meeting (Seminar) - 15th April, 2020.

- Lab meeting (Seminar) - 16th June, 2020.

- Author's Workshop (Workshop) - 8th - 15th July, 2020.
- Metallurgy seminar, Alessandro Difalco, Virtual, 20th October, 2020.
- PhD defense seminar, Valerio Gulino, Virtual, 2nd November, 2020.
- PhD defense seminar, Dario Gianoglio, Virtual, 22nd January, 2021.
- PhD defense seminar, Mattia Costamagna, Virtual, 25th March, 2021.
- The Life Cycle Assessment Methodology to support the Study of Materials, Dr. Mattia Costamagna, Virtual, 21st April, 2021.
- Aging phenomena in Lithium-Ion batteries – an automotive perspective, Matteo Dotoli, Virtual, 7th July, 2021.

Teaching Activities

- Lab of "Selection and use of Materials", Laurea Magistrale in Scienza dei Materiali, Prof. Paola Rizzi, Prof. Mauro Palumbo, 30th Nov - 1st Dec, 14th -16th Dec, 2020.

ACKNOWLEDGEMENTS

I would like to extend my thanks to the perfect mentor and supervisor, Prof. Paola Rizzi who has been imperative in guiding and motivating me throughout my PhD journey. A constant source of knowledge and optimism, she has been vital for always pushing me in the positive direction.

I would also like to thank Prof. Eva Pellicer for hosting me at the Universitat Autonoma di Barcelon, Spain, where I had the amazing opportunity of pursuing research for a period of three months. It was an extremely amicable and supportive association that made a significant contribution in my research work. The same goes for my collaborators from INRIM, Turin, Italy who were involved invaluably with my PhD work every now and then.

A very special acknowledgement for the whole Metallurgy group who provided me an immensely collaborative and friendly ambience to work in. My colleagues were always happy to help and inspire me. The time spent in the group is a memorable one filled with only joyful moments of learning and having fun together.

Words are not enough to express my gratitude towards my parents for their, sacrifices, love and incessant encouragement who even though were distant from me, made sure to make me feel blessed and cared for. This journey would not have been possible without them beside me. Forever grateful to my fiancé, who has stood beside me in every step of this journey, provided rock solid support, instilled confidence in me and dealt with me during my low times with only love and patience. A big thank you to my brother and sister-in-law for always being there for me and helping me along in all ways possible. Thanks to my sister and friends as well for cheering me on the way, listening to my thoughts and feelings and providing me a push whenever I needed. My second family (my fiancé's family) deserves a mention too, for always being proud of me and fortifying me with positivity. Last but not the least, I want to thank Nonna (my landlady who I dearly call so), a figure of kindness and affection for me during these three years, who treated me like her own granddaughter and made me feel at home in a foreign country.

To sum up, this PhD journey of three years has been extremely fulfilling and fruitful to me in all respects thanks to the amazing support system consisting of kind, loving, helpful and positive people I had the fortune of surrounding myself with.